UNIVERSITÀ
degli STUDI
di CATANIA

Dipartimento
di Fisica
e Astronomia
"Ettore Majorana"

PhD programme in physics

Roberto Corso

New developments in silicon and multi-junction photovoltaics

PhD thesis

Supervisors:
Dr. S. A. Lombardo
Prof. R. Reitano

---

academic year 2022/2023

Contents

Introduction

The efficient generation of energy is the task that is becoming more and more important on a global scale in the third millennium. With the population growing at an increasing rate and with a number of emerging countries in Africa and Asia eager to establish robust industrial and residential networks of infrastructures in order to match the welfare of developed countries, the need for energy has been rising dramatically in the last decades. Moreover, answering this energy demand through the use of fossil fuels is what has exacerbated the climatic changes that had been worrying the scientific community since the last century, and which are now a reality that is becoming more apparent every day. In addition to that, the recent political crisis between Ukraine and Russia that started in 2022 has affected the economical stability of the whole Europe, as many European countries heavily relied on Russian gas for their energy production. Therefore, the developments of the last decades have made it clear that we need to rethink not only our energy production paradigm, but also how it is managed in terms of storage and use, both at utility and residential scale.

Given the aforementioned context, researchers and industries have turned their attention to renewable energy sources. Of these sources, hydropower is one of the most ancient, as watermills have been used even by Romans and Greek, and for what regards the generation of electricity, it is one of the most flexible, as the generation of power can be quickly adapted to the energy demand from the grid; it has a very high energy storage capacity and hydroelectric plants have very long lifetimes, even up to

several decades. However, it requires large masses of water stored in dams, which restricts the number of suitable sites for the installation of plants, and the water reservoirs can significantly alter the surrounding ecosystems both downstream and upstream of the plant; it also requires large extensions of land, causing the relocation of many people, and it can even contribute to the emission of greenhouse gases, in particular methane which comes from the mass of plants rotting in anaerobic conditions underwater.

In contrast, geothermal power is one of the most recent, as the first geothermal power generator was tested in 1904 in Larderello (Italy), by Piero Gino Conti, and Italy has been the only producer of geothermal electricity in the world for the fist half of 20th century. In this case, the energy is provided by the heat flow from the inner layers of Earth, and it is replenished by radioactive decay processes: theoretically, the power rate of these processes is more than enough to satisfy the current global energy demand, but this power is on average too diffuse across the surface of the Earth, except in specific localized sites (tectonic plate boundaries, magma conduits or hot springs). For this reason, it has generally seen little use in terms of relative energy production in most nations, with some exceptional cases, such as Iceland and Kenya.

Another possible option is the bioenergy obtained from biomass such as wood, residues from wood processing and agriculture and organic waste from industries and residential areas. However, employing most of these sources poses several challenges: harvesting and burning wood from forests requires careful and sustainable management of forestry and CO_2 balance and its low surface power density implies that it requires extensive land, for which it competes against food crops.

Similarly to hydropower, wind power has been harnessed for millennia for sailing rivers and seas first and then in the Middle Age to power grain processing in windmills. The first wind turbines were developed in Scotland, Ohio and Denmark towards the end of 19th century. In the last decades, wind power has rose in popularity thanks to its simplicity, cheap costs, very low greenhouse gas emissions and the possibility of offshore installations. However, wind is one of the most volatile sources, with fluctuations on hourly, daily and seasonal scales, making utility scale energy storage and integration with other sources mandatory in order to guaran-

tee the stability of the electrical grid. Moreover, the size of wind turbines and their spacing in wind farms increases the land needed for this plants, which has raised concern about their visual impact, especially in scenic, protected and archaeological areas, and about potential danger for flying wildlife. Lastly, a new issue is rising as many turbines have been reaching their lifetime end (of about 20 years), resulting in a large quantity of scrap. In this regard, turbine blades are especially hard to recycle in order to recover the fiber glass-reinforced polymers they are made of, and this is becoming an important aspect in countries that have been relying on wind power for years, such as Denmark.
Finally, the photovoltaic effect was first discovered by Edmond Becquerel in 1839, and the first solar cell prototypes were realized at the end of 19th century. First installed on satellites in the late '50s, extensive research in new technologies, processes and cell designs has allowed the sector to compete in terrestrial applications in terms of energy production and cost of energy, with installed capacity rapidly increasing since the 2000s. Compared to the other energy sources presented above, photovoltaics is suited both to large utility scale installations and small systems for residential energy production. Although the power production is ultimately influenced by weather, solar energy is always available every day, making the technology particularly appealing for locations with high irradiance throughout the year. However, the fact that the power production is directly related with the day/night cycle means that in general peak production does not correspond to peak consumption, and therefore smart grids or energy storage systems are often required, especially in residential applications. In terms of CO_2 production, photovoltaics ranks as one of the most sustainable among the other energy sources, as the amount of CO_2 produced by the module manufacturing process is offset by the long lifetime of the modules of about 30 years. However, as is the case for wind turbines, recyclability is becoming a more pressing aspect of new module installation. This is especially relevant for the case of solar modules, as the manufacturing of solar modules must take into account another variable: critical materials. Critical materials are elements that are either in relatively short supply or difficult to extract, critical for several industries, or whose supply is vulnerable due to political instabilities. Currently, solar modules require some of these element, namely indium

and silver, whereas other components, such as glass, may require a larger supply as the installed capacity grows, so the possibility to recover these materials from old modules is getting more and more attention. In addition to that, more than 90% of the crystalline silicon, which is the most diffuse semiconductor for terrestrial applications, is currently produced by China, which also manufactures more than 90% of solar modules. In response to this, Europe and the US have enacted a series of policies to establish a robust value chain for photovoltaics, with particular emphasis on the research on new materials, technologies and module designs.
In this thesis, I will present the results of my activity for the PhD programme in Physics, which focused on the characterization of new materials for silicon modules and on the development of new modules with higher efficiency compared to traditional silicon modules. In the first chapter of this work, I will present a brief history of the state of the art and of the technological breakthroughs that have lead the industry to the current state, and I will describe the different cell designs that are currently employed with their differences and advantages, along with the limiting factors for the current silicon technology. In the second chapter I will describe a theoretical activity focused on the development of a Monte Carlo simulation tool that I have employed to simulate the performance of an optimized voltage-matched two-terminal module. In the third chapter I will present a MATLAB model that has been developed to predict the performance of bifacial installations, along with the insight that has been obtained from the model and the outdoor experimental activity that has been carried out to validate the theoretical results. The fourth chapter features the culmination of the concepts presented in the previous chapter, as I will present an experimental demonstration of a multi-junction bifacial gallium arsenide/silicon module that has been tested in outdoor, achieving high and stable efficiency throughout the day. In the last chapter, I will present some results on the characterization of new materials that can be considered for the substitution of critical materials currently employed in anti-reflective layers in silicon solar cells.

Chapter 1

History and present of silicon PV

1.1 Theoretical understanding

1.1.1 Detailed balance

Even though some effort had already been dedicated towards the calculation of the efficiency of solar cells, the greatest contribution to this topic came from the work of Shockley and Queisser in 1961 [1]: whereas previous works focused on predicting cell efficiency from empirical values [2], they preferred the fully theoretical approach of the detailed balance principle, which states that in a system at equilibrium each process must be in equilibrium with its reverse process, providing much more solid information on the potential that solar cell could reach.
In their discussion, Shockley and Queisser indicate three main factors that would influence the efficiency of a solar cell: the probability t_s that a photon with greater energy than the bandgap E_g of the semiconductor will produce a hole-electron pair, the weight of radiative recombination f_c (which is the reverse process of the photon absorption described by t_s) with respect to all the other recombinations processes and the geometrical configuration of the system (regarding aspects such as the angle of incidence of light or the solid angle subtended by the light source) which are summarized in a factor f_ω; the detailed balance limit is achieved when all these factors are equal to 1.
In this ideal condition, five processes must be at equilibrium: the gener-

ation of hole-electron pairs by the incident radiation with a rate F_s, the radiative recombination of hole-electron pairs with resultant emission of photons at a rate F_c, other nonradiative processes in which hole-electron pairs may be generated or recombined and the removal of carriers in the form of a current I which translates into a rate $\frac{I}{q}$, where q is the electron charge.
For the first of these processes, they assume that the incident radiation comes from a blackbody at temperature T_s. Therefore, $Q_s(\nu_g, T_s)$ is the flux of photons with frequency $\nu_g > \frac{E_g}{h}$, where h is Planck's constant:

$$Q_s(\nu_g, T_s) = \frac{2\pi}{c^2} \int_{\nu_g}^{\infty} \frac{\nu^2}{e^{\frac{h\nu}{kT_s}} - 1} \, \mathrm{d}\nu = \frac{2\pi \left(kT_s\right)^3}{h^3 c^2} \int_{x_g}^{\infty} \frac{x^2}{e^x - 1} \, \mathrm{d}x \tag{1.1}$$

with k being Bolztmann's constant, c the speed of light in vacuum and $x = \frac{h\nu}{kT_s}$. Then, for a solar cell of surface area A, the photogeneration rate of hole-electron pairs is given by:

$$F_s = A t_s f_\omega Q_s. \tag{1.2}$$

Analogously, the rate of radiative recombination from a cell at temperature T_c is

$$F_{c0} = 2A t_c f_\omega Q_c. \tag{1.3}$$

where the factor 2 comes from the fact that both sides of the cell can contribute to the blackbody radiation of the cell Q_c; t_c may in general be different from t_s because of the difference in the spectral distribution of the blackbody radiation at T_c and at T_s and how this difference relates to the reflectivity and transmittivity of the surface of the cell. Shockley and Queisser only consider recombination between free carriers, therefore the recombination rate must be proportional to the product of their densities np. At equilibrium this value must be equal to n_i^2, whereas out of equilibrium the general rate is defined as :

$$F_c(V) = F_{c0} \frac{np}{n_i^2} = F_{c0} e^{\frac{V}{V_{th}}} \tag{1.4}$$

where $V_{th} = \frac{kT_c}{q}$ is often called thermal voltage [3]. Lastly, the nonradiative recombination rate is $R_r(V)$ and the nonradiative generation rate is

$R_g(0)$, and these will be equal for $V = 0$. The steady state condition can then be expressed by:

$$F_s - F_c(V) + R_g(0) - R_r(V) - \frac{I}{q} = 0 \tag{1.5}$$

It is useful to consider the case in which the cell is surrounded by a blackbody at temperature T_c ($F_s = F_{c0}$). At this point, the factor f_c can be introduced as the fraction of radiative processes compared to nonradiative processes:

$$F_{c0} - F_c(V) = f_c \left[F_{c0} - F_c(V) + R_g(0) - R_r(V)\right] \tag{1.6}$$

assuming that the nonradiative recombination follows the ideal rectifier equation $R_r(V) = R_g(0)e^{\frac{V}{V_c}}$, substituting Equation (1.4) and rearranging the terms returns

$$F_{c0}\left(1 - e^{\frac{V}{V_{th}}}\right) = f_c \left[F_{c0} + R_g(0)\right]\left(1 - e^{\frac{V}{V_{th}}}\right) \tag{1.7}$$

from which an expression for f_c independent from the voltage applied to the cell can be obtained:

$$f_c = \frac{F_{c0}}{F_{c0} + R_g(0)}; \tag{1.8}$$

conversely, applying these steps to Equation (1.5) yields

$$\left[F_{c0} + R_g(0)\right]\left(1 - e^{\frac{V}{V_{th}}}\right) - \frac{I}{q} = 0 \tag{1.9}$$

which can be rearranged into

$$I = I_0\left(1 - e^{\frac{V}{V_{th}}}\right) \tag{1.10}$$

where

$$I_0 = q\left[F_{c0} + R_g(0)\right] \tag{1.11}$$

is the dark saturation current.
For the case of a general irradiance, by adding and subtracting F_{c0} from

Equation (1.5) and rearranging the terms one obtains the current-voltage (I-V) characteristics of a solar cell

$$\begin{aligned} I &= q\left(F_s - F_{c0}\right) + q\left[F_{c0} - F_c(V) + R_g(0) - R_r(V)\right] = \\ &= q\left(F_s - F_{c0}\right) + q\left[F_{c0} + R_g(0)\right]\left(1 - e^{\frac{V}{V_{th}}}\right) \end{aligned} \tag{1.12}$$

which is usually reported in the following form:

$$I(V) = I_{sc} - I_0\left(e^{\frac{V}{V_{th}}} - 1\right). \tag{1.13}$$

I_{sc}, corresponding to $q\left(F_s - F_{c0}\right)$, represents the short-circuit current measured at $V = 0$. Generally, F_{c0} is several orders of magnitude smaller than F_s and is often neglected, and the I_sc is defined by a simpler general expression

$$I_{sc} = qA\int_{E_g}^{\infty} EQE(E)\phi(E)\,\mathrm{d}E \tag{1.14}$$

where $\phi(E)$ is the incident photon flux and the External Quantum Efficiency $EQE(E)$, defined as the ratio of collected carriers over incident photons, includes the photon absorption probability and losses due to reflection. Moreover, solving Equation (1.13) for $I = 0$ returns the open-circuit voltage

$$V_{oc} = V_{th}\ln\left(\frac{I_{sc}}{I_0} - 1\right). \tag{1.15}$$

Once the I-V characteristics of the solar cell has been obtained in the detailed balance limit, its efficiency can be determined by finding its maximum power point, either by solving $\frac{\mathrm{d}(IV)}{\mathrm{d}V} = 0$ or numerically, and dividing for the incident optical power.
Shockley and Queisser considered the 6000 K blackbody radiation, obtaining a maximum efficiency of 31% for a 1.35 eV semiconductor and of about 30% for silicon (1.12 eV bandgap) [4], while for the modern standard solar spectrum the highest efficiency lies at 33% for a 1.34 eV bandgap semiconductor and 32% for silicon [5].

1.1.2 Additional effects

As mentioned in the previous Section 1.1.1, one of the conditions required for the detailed balance limit is that the factor f_c, which indicates the weight of radiative processes compared to the nonradiative processes, is equal to 1. By looking at the expression for f_c given by Equation (1.8), it can be seen that this condition can only be fulfilled when the nonradiative generation rate $R_g(0)$ (and, consequently, the nonradiative recombination rate) is set to 0: that is, when all nonradiative processes are turned off. Among the three main recombination mechanisms in solar cells, radiative recombination has already been accounted for in the detailed balance limit, and one can in theory imagine a defectless material and therefore eliminate Shockley-Read-Hall (SRH, or trap-assisted) recombination (Figure 1.1). However, Auger recombination is still a fundamental physical process, and for this reason it has been the focus of several works aiming to refine the initial calculation of Shockley and Queisser.

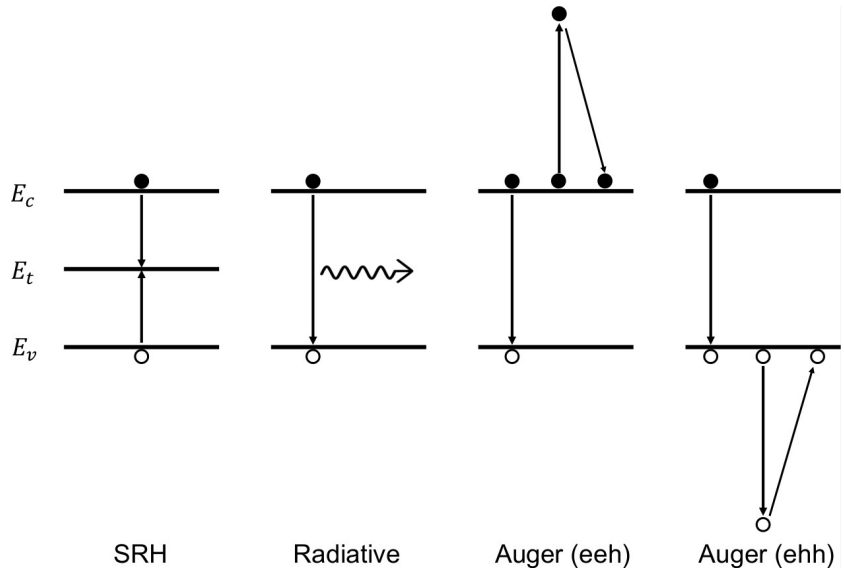

Figure 1.1: Main recombination processes in a solar cell.

In Auger recombination, the energy from the recombination of a hole-electron pair is transferred to another carrier as kinetic energy and then dissipated by thermalization in interactions with the phonons [6, 7] (Fig-

ure 1.1). The other carrier can either be a hole (the process is usually referred to as ehh process) or an electron (eeh process): for low-injection conditions, in the former case the recombination rate is given by [7]

$$R = C_p \left(n p^2 - n_0 p_0^2 \right) \tag{1.16a}$$

with a lifetime

$$\tau = \frac{1}{C_p p^2} \tag{1.16b}$$

in p-type materials; in the latter case, the recombination rate is given by

$$R = C_n \left(n^2 p - n_0^2 p_0 \right) \tag{1.17a}$$

with a lifetime

$$\tau = \frac{1}{C_n n^2} \tag{1.17b}$$

in n-type materials, where C_p and C_n are two coefficients (measured in cm^2/s), n and p are the electron and hole non-equilibrium densities and the subscript 0 indicates their equilibrium counterparts. In general, this processes depend on the two coefficients C_p and C_n, but in the high-injection case an approximate rate is given by [6]

$$R \simeq \left(C_a n^3 \right) \simeq \left(C_a p^3 \right) \tag{1.18}$$

where $C_a = C_n + C_p$. In [8], C_n and C_p have been measured by fitting carrier lifetime measurements at doping concentrations ranging from $10^{18}\ \mathrm{cm}^{-3}$ to $10^{20}\ \mathrm{cm}^{-3}$, obtaining $C_n = 2.8 \cdot 10^{-31}\ \mathrm{cm}^2/\mathrm{s}$ and $C_p = 9.9 \cdot 10^{-32}\ \mathrm{cm}^2/\mathrm{s}$ at 300 K, with a slight decrease at 77 K. In [9], the total coefficient C_a was measured in the high injection regime by performing open-circuit voltage decay measurements on a custom test structure designed to maximize sensitivity to Auger recombination, obtaining $C_a = 1.6 \cdot 10^{-30}\ \mathrm{cm}^2/\mathrm{s}$.

As mentioned previously, several works incorporated Auger recombination to improve theoretical efficiency calculations. In one of the earliest works [10], Auger recombination was used with the coefficients reported in [8] to estimate the maximum open-circuit voltage of a silicon solar cell

both in low and high injection regime, assuming perfect photon absorption (hence the maximum current possible); for a 300 µm thick cell, a maximum voltage of about 770 mV under the standard extraterrestrial solar spectrum was calculated (down from the value of 837 mV in the detailed balance limit), with a corresponding efficiency of about 28% for the extraterrestrial spectrum and 30% for the terrestrial spectrum.
However, the values reported in [8] and [9] showed a discrepancy between the low injection and the high injection cases, as the sum of C_n and C_p does not equal C_a: in [11], this deviation has been attributed to Coulomb interactions between free carriers, which enhance Auger recombination in the low injection regime, and two enhancement factors g_{eeh} and g_{ehh} for the two processes have been defined from quantum-mechanical calculations in p-type silicon. Furthermore, the dopant concentration range of applicability of the Coulomb-assisted Auger recombination was expanded towards low concentrations in [12] by introducing an empirical expression for g_{eeh} and g_{ehh} as well as a parameterization of C_p of second order in temperature. A further refinement has been proposed in [13] considering also the interaction with fixed charges, therefore expanding the validity of the parametric expression to a larger range of dopant concentrations both in high and low injection regimes. Lastly, an improvement was presented in [14] which takes into account Coulomb-enhanced radiative recombination to fit experimental lifetime data measured on n-type and p-type samples realized with improved passivation techniques (compared to those available at the time of the previous works).
Another fundamental effect that has been considered in refinements of the theoretical efficiency is free carrier absorption (FCA). In FCA, photons are absorbed by either free electrons or holes, leading to a transition in the same band (intraband absorption) or between two conduction bands (interband absorption), then the photon energy is lost due to thermalization. FCA becomes significant and competes with intrinsic absorption at energies close to the bandgap and in the sub-bandgap region, especially at high carrier concentrations [15]. One of the first parameterization was elaborated against experimental absorption data for wavelengths in the order of several µm [16]; however, this commonly used model was based on a number of assumptions which limited its validity. For this reason, in [17] a new formulation was introduced, applicable for both p- and n-type

silicon and for doping densities as high as 10^{21} cm^{-3}. Then, in [15], it was shown that the previous models performed poorly in the wavelength range between 1 µm and 2 µm, and a new parameterization was proposed to fit experimental data in this range.
For what concerns radiative recombination, its rate is usually expressed as $R = B\left(pn - n_i^2\right)$, where n_i is the intrinsic carrier concentration; however, each photon generated by a recombination event has a chance of being reabsorbed in another band-to-band transition, especially in devices specifically designed for light trapping. This phenomenon, referred to as photon recycling (PR), is usually included by multiplying B by $1 - P_{PR}$, where P_{PR} is a probability [13] that depends on the light trapping scheme employed and therefore on the geometric path length of light.
All the effects discussed above have been included in a new calculation of the theoretical efficiency of silicon by Richter *et al.* [18], namely the update standard solar spectrum, the optical constants for silicon in [19], the free carrier absorption presented in [15], the Coulomb-assisted Auger recombination from [14], the photon recycling with the radiative recombination coefficient B derived in [20] and the bandgap narrowing described in [21, 22]. The authors find a maximum efficiency of 29.43% for a 110 µm thick silicon cell, which is nowadays the most commonly reported value in the literature.

1.2 Fabrication of a solar cell

Silicon is by far the most important and popular semiconductor material since the emergence of solid-state electronics in the late '50s. Different forms of silicon are classified based on the purity of the material and of the grain size [23], and the photovoltaic industry has progressively shifted towards purer and purer forms, increasing efficiency and module lifetime, though the purity needed is still inferior compared to the electronics industry. For the photovoltaic industry, metallurgical grade silicon (or silicon metal), characterized by a minimum purity of 96% (98% on average), is the starting point in the production process of a solar cell [24]. Silica (SiO_2) is the most common mineral in the crust of Earth, but rather than common beach sand, high purity quartz is reduced by removing the

oxygen for the production of metallurgical silicon through the following reaction (which is actually the sum of several steps) [25]:

$$SiO_2\,(s) + 2\,C\,(s) = Si\,(l) + 2\,CO\,(g) \qquad \{1\}$$

This reaction takes place in electric arc furnaces, where the reagents are heated by an intense electric arc sustained between the tip of three submerged carbon electrodes and the electrical ground of the furnace. Liquid silicon metal is tapped from the bottom of the furnace, while the resulting CO is further oxidized to carbon dioxide in open furnaces and released into the atmosphere. Crude liquid silicon contains impurities between 1% and 4%, mainly iron, aluminum, calcium, titanium and carbon, and is further refined with oxidative gas and slag-forming additives, with the resulting slag being separated mechanically from the liquid silicon which is poured into a casting mold [24].
However, the semiconductor industry requires a purer form of silicon, with impurities in the range of part per billion (ppb) or even part per trillion (ppt), usually referred to as polysilicon. The general roadmap of the processes to obtain polysilicon consists in perparing a volatile silicon hydride and purifying it, generally by fractional distillation, followed by the decomposition of this hydride to pure elemental silicon by reductive pyrolysis or chemical vapour deposition. Lastly, the by-products generated by the preparation and treatment of the volatile compound, which may be different for each process, need to be recycled.

1.2.1 The Siemens process

The Siemens process (from the name of the company that developed it) was introduced in the late '50s, but it is still vastly employed. The first step is the formation of the volatile trichlorosilane:

$$Si\,(s) + 3\,HCl \longrightarrow SiHCl_3 + H_2 \qquad \{2a\}$$

This reaction occurs between 300 °C and 350°C, with a competing reaction forming tetrachlorosilane

$$Si\,(s) + 4\,HCl \longrightarrow SiCl_4 + 2\,H_2 \qquad \{2b\}$$

During this reaction impurities such as Fe, Al, and B react to form their halides (e.g. $FeCl_3$, $AlCl_3$, and BCl_3). Trichlorosilane is chosen because of its lower boiling point (31.8 °C) and high volatility compared to other silanes, making it easier to purify from the other halides by fractional distillation [26]. Then, trichlorosilane is vaporized, diluted with hydrogen and introduced in the deposition reactors, where the gas is decomposed on the surface of silicon seed rods, electrically heated to about 1100 °C, growing large rods of pure silicon. The main reactions occurring in the chamber are:

$$2\,SiHCl_3 \longrightarrow SiH_2Cl_2 + SiCl_4 \quad \{3a\}$$

$$SiH_2Cl_2 \longrightarrow Si + 2\,HCl \quad \{3b\}$$

$$H_2 + SiHCl_3 \longrightarrow Si + 3\,HCl \quad \{3c\}$$

$$HCl + SiHCl_3 \longrightarrow SiCl_4 + H_2 \quad \{3d\}$$

As shown in the equilibrium above, several by-products are generated in the chamber, the most relevant being $SiCl_4$ (about 3 to 4 moles per mole of polysilicon [27]). While tetrachlorosilane has other industrial applications, the demand is much lower than the production form the Siemens process; for this reason, it is usually preferred to recycle it on-site back to trichlorosilane. Two approaches are employed to perform this step: one is the reduction with hydrogen at about 1000 °C

$$SiCl_4 + H_2 = SiHCl_3 + HCl \quad \{4a\}$$

This process has the advantage that the trichlorosilane produced is of very high quality because both reactants are already of high quality as they are produced by Reaction {3a} and Reaction {3d}. The other way is the hydrogenation of tetrachlorosilane in a mass bed of metallurgical silicon at 500 °C and 35 atm.

$$3\,SiCl_4 + 2\,H_2 + Si = 4\,SiHCl_3 \quad \{4b\}$$

As mentioned, despite its widespread employment in the industry, the Siemens process requires a large amount of energy because of the high temperatures and produce several by-products that must be handled or recycled. For this reason, alternative processes have been introduced to

overcome these disadvantages.
One of such processes, introduced in the '70s, is the Komatsu/Union Carbide (UCC) process [28], where the trichlorosilane obtained and treated as in the Siemens process is inserted into fixed-bed columns filled with quaternary ammonium ion exchange resins acting as catalysts for the following reactions:

$$2\,SiHCl_3 = SiH_2Cl_2 + SiCl_4 \quad \{5a\}$$

$$3\,SiH_2Cl_2 = SiH_4 + 2\,SiHCl_3 \quad \{5b\}$$

The main product of this reactions, silane (SiH_4), is further purified by distillation and then pyrolysed at 800 °C to produce polysilicon onto heated silicon seed rods:

$$SiH_4 = 2\,H_2 + Si \quad \{6\}$$

The main advantages of this process are the lower temperature of pyrolysis and that most of the by-products are recycled and purified several times. However, the recycling of trichlorosilane into monosilane requires a number of additional steps, which are needed in order to increase the yield of suitable silane.
Another process, named Ethyl Corporation process after the company that developed it, ditches the idea of refining metallurgic silicon altogether in favor of alkaline fluorosilicate (M_2SiF_6, M being an alkaline element), which is in large supply as a by-product of the fertilizer industry. Silicon tetrafluoride (SiF_4) is sublimated by heating the fluorosilicates, then it is hydrogenated to silane by metal hydrides such as lithium aluminium hydride or sodium aluminium hydride:

$$2\,H_2 + M + Al = AlMH_4 \quad \{7a\}$$

$$SiF_4 + AlMH_4 = SiH_4 + AlMF_4 \quad \{7b\}$$

with M being either Na or Li. After distillation, SiH_4 is thermally decomposed to polysilicon as described by Reaction {6}, although in a different type of reactor. The main advantages of this process are the lower operating temperature, the higher efficiency of the different reactor and the fact that no additional treatments such as crushing are required; however, it also presents a higher risk of hydrogen absorption and contamination from the reactor walls.

1.2.2 The Czochralski process

In addition to the classification by purity, silicon has also been classified by its grain size: following the nomenclature introduced in [23], microcrystalline silicon (µc-Si) features grains smaller than 1 µm, polycrystalline silicon (pc-Si) features grains between 1 µm and 1 mm, multicrystalline silicon (mc-Si) features grains between 1 mm and 10 cm and single-crystalline silicon (sc-Si or simply c-Si) exhibits grains larger than 20 cm. Nowadays, the majority of silicon solar cells are fabricated from single crystalline silicon wafers, as these can reach higher efficiencies than cells in multicrystalline silicon [29]. In fact, even though multicrystalline silicon wafers can have rectangular or square shape for a better utilization of the module area (usually referred to as cell-to-module ratio) in comparison to the pseudo-square single crystalline cells, their efficiency is affected by extended defects such as grain boundaries and dislocations [30, 31].
The main process to grow single silicon crystals is the Czochralski (Cz) process, first discovered serendipitously by Jan Czochralski in 1918: the polish chemist dipped his pen in molten tin, drawing a filament which resulted being a single crystal [32]. The Cz equipment consists of a vacuum or inert chamber in which feedstock material, such as polycrystalline silicon pieces or residues from single crystals, is melted at about 1425 °C in a quartz crucible. Dopant atoms such as boron or phosphorus can be added to the molten silicon to obtain p-type or n-type silicon. The process consists in dipping a <100>-oriented monocrystalline seed into the melt and slowly withdrawing it vertically to the melt surface, where the liquid crystallizes at the seed [30]. After the silicon is completely molten, the temperature of the melt is stabilized at the required value to lower the seed into the melt: the temperature must be chosen so that the seed is not growing in diameter (if the melt is too cold) or decreasing in diameter (if the melt is too hot). The seed is pulled upwards, growing a so-called "crystal neck". Since dislocations propagate on (111) planes that are oblique in an <100>-oriented crystal, the dislocations grow out of the crystal neck after a couple of centimeters, so that the rest of the crystal grows dislocation-free. The transition region from the seed node to the cylindrical part of the crystal has the shape of a cone and is there-

fore called "seed cone". The diameter of the crystal can then be tuned by adapting the pulling speed, and at the end of the process, in order to complete the crystal growth free of dislocations, the pulling speed is increased, gradually reducing the crystal diameter and developing an end cone.
The Cz process presents several advantages that contributed to its success and diffusion: Cz crystals can be grown from a wide variety of differently shaped and doped feedstock materials, reducing raw material costs and increasing suitable sources; in fact, the feedstock is molten in a crucible and therefore the shape, grain size and resistivity of the different feedstock materials can be mixed for the required specifications, as long as macroscopic particles in pot scrap materials are avoided. Moreover, The Cz process acts as a purification step, allowing to obtain highly efficient solar cells even out of ingots grown from low-grade pot scrap material. Additionally, the homogeneity of a Cz ingot is reflected on the electrical and physical characteristics of the solar cells, whereas multicrystalline Si block casting produces samples with higher variances in most parameters. Lastly, silicon wafers obtained from Cz crystals are naturally <100>-oriented, allowing homogeneous texturing with a cost-effective wet chemical etching step [33]. By anisotropic etching, a surface texture characterized by regular pyramids is obtained, achieving light trapping and extending the optical path length inside the cell.

1.3 The different cell designs

In general, a silicon solar cell is made up by a p-n junction, with a total thickness between 140 µm and 170 µm (thinner for n-type wafers and thicker for p-type wafers) [34], an anti-reflection (AR) coating which minimizes reflectivity through destructive interference at certain wavelengths [35] and metallic contacts to collect the current generated by the cells. Additional elements, such as passivating layers or a back surface field (BSF), may be included to enhance the performance of the cell. In fact, interfaces between two dissimilar materials, such as those that occur at the surfaces of a solar cell, have a high concentration of defects due to the abrupt termination of the crystal lattice, often called "D-centers", which

can be thought of as dangling bonds. The number of these defects can be reduced by adding a layer that stabilizes (passivates) the silicon surface or by increasing the doping towards the surface: the interface between the high- and low-doped regions behaves like a p-n junction, creating an electric field which introduces a barrier to minority carrier flow to the surface [36]. The minority carrier concentration is thus maintained at higher levels in the bulk of the device, and the BSF has a net effect of passivating the surface, increasing both the I_{sc} and V_{oc} of the cell.
Several types of solar cell have been designed throughout the years and launched into the market.

1.3.1 Al-BSF cell

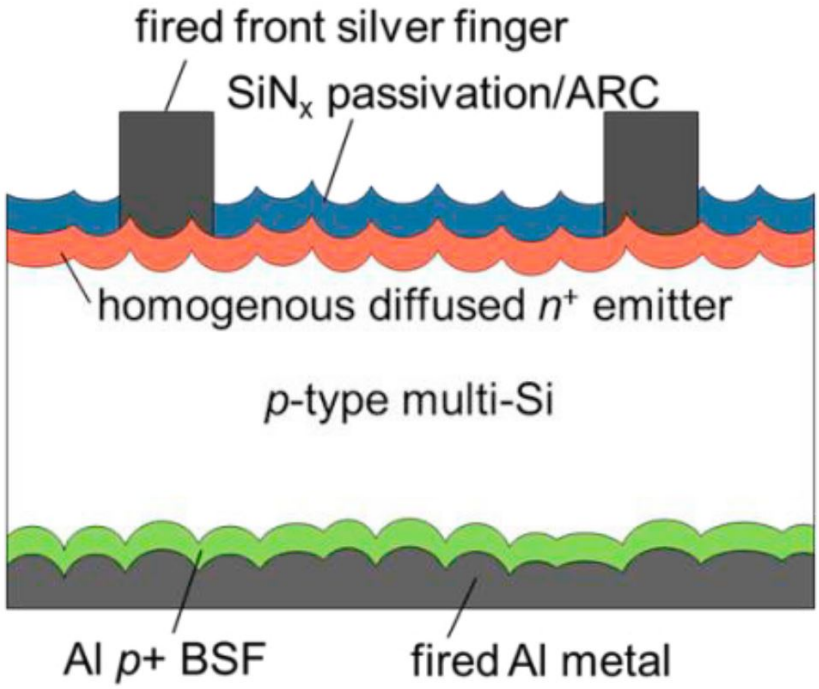

Figure 1.2: Schematic representation of an Al-BSF cell, reprinted from [37].

In the 50's and 60's, early silicon solar cells evolved in response to the interest of the space industry, although with single-digit efficien-

cies. For this reason, the cell design evolved to satisfy the corresponding requirements such as maximizing radiation resistance, therefore using high-resistivity p-type substrates to maximize radiation hardness. Then, in the early '70s It was realized that sintered aluminium on the rear surface of the cell improved its performance, by a combination of gettering and formation of a heavily doped rear interface (the BSF) which reduced rear recombination [38].
This design gained widespread popularity due to its easy manufacturing and low cost [37, 39], with efficiencies of about 17% already achieved in 1997 thanks to the SiN anti-reflection coating [40], and the technology dominated the market until the late 2010's, when it was overcome by the PERC cell [37, 41]. In fact, even though efficiency as high as 20% have been achieved [42], these cell are characterized by high rear side recombination losses due to the direct contact between silicon and the aluminum contact, which introduces a large number of surface state densities [41].

1.3.2 PERC cell

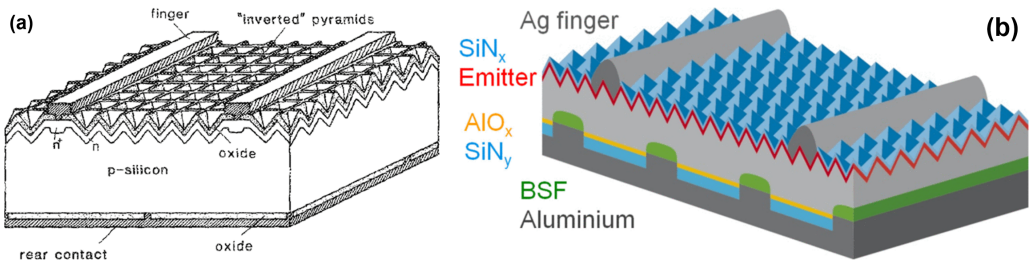

Figure 1.3: Schematic diagram of the 22.8% efficiency PERC cell, reprinted from [43] (a). Schematic diagram of an industrial PERC solar cell with AlO_x/SiN_y passivation layer, reprinted from [44] (b).

The Passivated Emitter and Rear Cell (PERC) was first proposed by Blakers *et al.* [45] in 1989. Compared to the Al-BSF cell, the PERC cell uses a thermally grown oxide to electronically passivate most of the rear cell surface. Contact is made at isolated contact holes through this passivating oxide directly to the underlying substrate [43] (Figure 1.3a). The

oxide layer also contributes as a reflective planar surface. The first prototype, with an inverted pyramid texturing on the front surface, achieved an efficiency of 22.8%. The initial high-performance PERC cells had no p+ layer at the rear contact points. Therefore, variations with boron diffusion covering a small fraction (Passivated Emitter Rear Locally diffused, "PERL") or the entire rear surface (Passivated Emitter Rear Totally diffused, "PERT") were also proposed in the following years [46]. However, it took 25 years until this technology reached economic and industrial competitiveness against the conventional Al-BSF cell [44], but it has now become the most prominent in the market [34]. The SiO_2 layer used in the first version of the cell (with a p-type silicon wafer) presents positive charges that can cause a depletion region or an n-type inversion layer to appear at the rear surface, increasing rear-surface recombination [46]. Commercial cells now employ an AlO_x/SiN_y layer, where the former assists with rear-surface passivation and the latter is used to withstand the following steps to deposit the aluminum paste (Figure 1.3b). Another improvement consisted in the laser ablation of the rear passivation layer to define the rear contact geometry, instead of the previously used photolithography [47].

1.3.3 SHJ cell

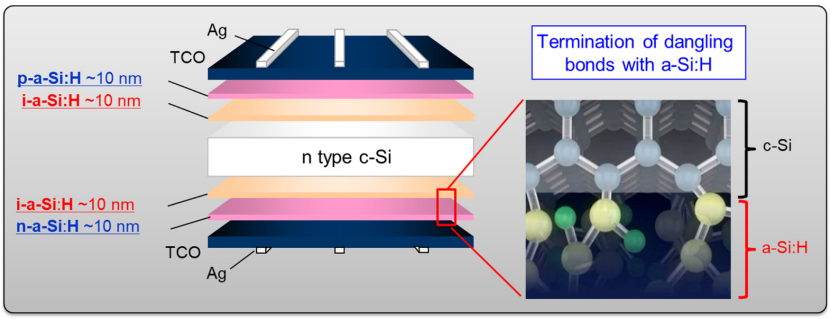

Figure 1.4: Schematic representation of an SHJ cell, with the surface passivation provided by the a−Si:H layer, reprinted from [48].

The main characteristic of the silicon heterojunction technology (SHJ) is that the p-n junction is not entirely realized by bulk Cz-Si, but rather

by crystalline silicon and amorphous silicon. The passivating ability of the hydrogenated amorphous silicon (a−Si:H) and the possibility to realize amorphous/crystalline heterostructures had been know since the '70s [49, 50]; in the following decades several prototypes had been realized, especially in Japan, achieving an efficiency of 12.3% [51, 52], and the japanese company Sanyo Electric Co. patented an improved structure where, in addition to the doped a−Si layers, another intrinsic layer was added as a buffer layer, suppressing the surface recombination and improving the V_{oc} and fill factor of the cell [48, 53, 54] (Figure 1.4). Compared to the PERC cell, the SHJ presents some important advantages: the metal contacts do not reach the bulk silicon directly, as this is protected by the amorphous layer and by a transparent conductive oxide (TCO), thus reducing the recombination rate and increasing the voltage output. Moreover, the fabrication process is much simpler, comprising a lower number of steps and lower temperatures [52, 55, 56]. Additionally, the SHJ cell results more resistant to high operating temperatures and is more suited to bifacial applications, as will be discussed in Sections 1.4 and 1.5. However, despite surpassing the PERC cell in terms of efficiency (with record efficiencies above 26%), its market share has remained limited, due to its high Ag requirements for the metal contact grids and In-rich TCO, such as indium tin oxide (ITO), increasing the price of this technology [34, 57].

1.3.4 TOPCon cell

The Tunnel Oxide Passivated Contact (TOPCon) structure is one of the most recent cell designs, first introduced in 2013 [59] by a group from the Fraunhofer Institute for Solar Energy Systems (Fraunhofer ISE). This design was introduced to circumvent the restriction of the amorphous silicon on the temperature during the fabrication process of SHJ cells, while still avoiding the requirement of laser assisted contact openings like in PERC cells [60]. For this reason, the passivating layer is structured as such: an ultra-thin wet chemical oxide layer was grown with a thickness of 14 Å (where 20 Å is considered to be the maximum thickness for an efficient tunneling [61]), followed by a a 20 nm thick phosphorus-doped Si layer was deposited on both sides [58]. To reduce the front surface recombination, the boron-doped p+ emitter was passivated by a stack of atomic

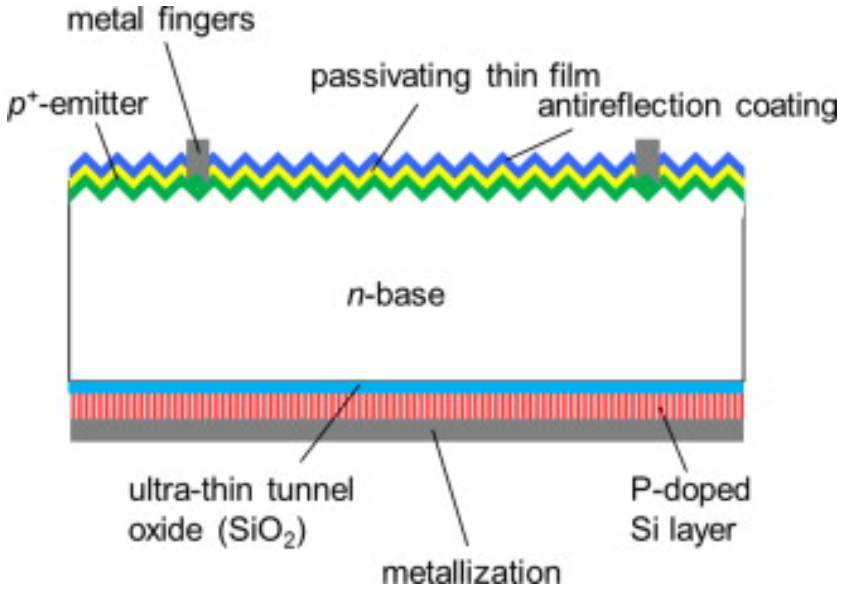

Figure 1.5: Schematic diagram of the TOPCon solar cell. The boron-doped emitter at the front is passivated by ALD Al_2O_3 and a PECVD SiN_x. Reprinted from [58].

layer deposited (ALD) aluminum oxide (Al_2O_3) and plasma-enhanced chemical vapor deposited (PECVD) silicon nitride (SiN_x) , with the latter also serving the purpose of anti-reflection coating (Figure 1.5). With this design, the interface passivation can withstand up to 400 °C, while still achieving high efficiency (23%) and fill factor (81%) [59]. In a following work, the same group developed an evolution of the original design by replicating their innovative passivating layer on the front surface on a p-type wafer [62], while other groups investigated the double-sided TOPCon architecture on n-type wafers [63]. In 2016 the first large area cell was reported [64] (239 cm^2 with an efficiency of 21.4%). Since then, the technology has continued to improve, with cell efficiencies around 24% and module efficiencies around 21% (higher than PERC but lower than SHJ and IBC) [34].

1.3.5 IBC cell

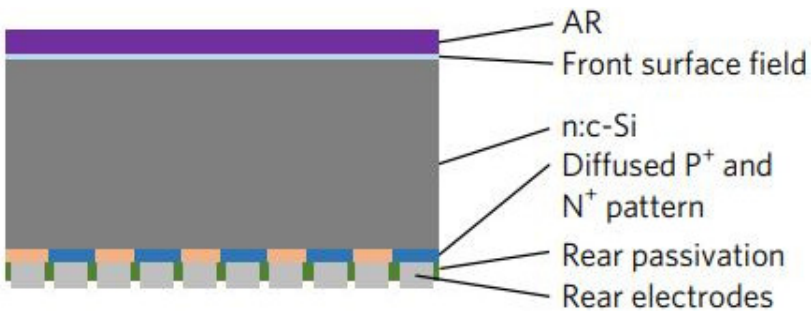

Figure 1.6: IBC solar cell schematic diagram. Reprinted from [65].

One of the most immediate sources of performance loss in solar cell is the front contact grid, not only for the recombination issues described the previous sections, but also because it reduces the active area of the cell (and the consequent current output). To answer this issue, the Interdigitated Back Contact (IBC) cell was introduced in 1975 by Schwartz and Lammert [66]. The main characteristic of this cell is that the front surface is completely free from the contact grid, whereas both the positive and negative contacts are implemented on the back surface (Figure 1.6). Along with the direct consequence of nullifying the grid shadowing, moving all the contacts to the unilluminated side of the device allows to optimize the contacts in order to reduce series resistance without impacting on the active area and also eliminates the need to allow lateral current flows through thin layers [67]. However, the diffusion length in the material needs to exceed the length of the device, as the carriers have to travel trough the whole device to the rear surface. For this reason, n-type wafers are usually employed for IBC cells, as they exhibit a longer minority carrier lifetime [68]. The main challenge in the fabrication of IBC cells is how to realize the interdigitated n-regions and p-regions on the rear surface. One of the possible solution is to print a boron-doped diffusion mask layer with the interdigitated structure on the rear surface: the boron in the mask layer diffuses into the n-type substrate to form the p+ region, while the unprinted regions form the n+ region by phosphorus diffusion. However, this approach may suffer from the poor accuracy and repeatability of the alignment [69]. In alternative to this process, ion

implantation has also been proposed for the emitter [70, 71]. In terms of efficiency, the IBC technology is the one with the highest results, with several record-breaking results of over 26% efficiency [65, 72] (although it has to be noted that these devices also integrated the heterojunction structure for its efficient passivation). However, despite its high performance, the market share of the IBC technology remains quite limited, due to its high cost and complexity of the manufacturing process [73].

1.4 The effect of temperature on solar cells

Since the early years of PV research, it has been cleared that temperature effected the performance of solar cells [74]. As evidenced in Sections 1.1.1 and 1.1.2, the efficiency of a solar cell is influenced by its match with the solar spectrum (determining the energy lost by high energy photons due to thermalization and the threshold below which photons are not absorbed by the semiconductor) and the balance between generation and recombination processes; hence, the temperature dependence of the overall efficiency stems from the dependence of the semiconductor bandgap and the dependence of the aforementioned processes.
The bandgap of semiconductors changes with temperature, because of modifications to the band energies caused by electron–phonon interactions and by thermal expansion of the lattice. While most semiconductor bandgaps decrease almost linearly in the typical temperature range of operation of solar cells, there is no general relation between the bandgap and its temperature dependence [75]. In one of the earliest works on the topic, Varshni proposed an empirical formula for the bandgap [76]:

$$E_g(T) = E_g(0) - \frac{\alpha T^2}{T + \beta} \tag{1.19}$$

where α and β are coefficients dependent on the specific semiconductors. As this fit resulted poorly accurate for low temperatures, an improvent was proposed in the following form [77]:

$$E_g(T) = E_g(0) - S\langle\hbar\omega\rangle \left[\coth\left(\frac{\langle\hbar\omega\rangle}{2kT}\right) - 1\right] \tag{1.20}$$

where S is a coupling constant and $\langle \hbar\omega \rangle$ is the average phonon energy. In this model the bandgap shift is mostly attributed to phonon excitations, and these are in turn related to the dependence of the bandgap on the lattice expansion.
Another aspect to be considered is the concentration of intrinsic carriers n_i. This is given by [78]

$$n_i = \sqrt{N_V N_C} e^{\frac{-E_g}{2kT}} \tag{1.21}$$

where N_V and N_C are the valence band and conduction band effective densities of states

$$N_{V,C} = 2 \left(\frac{2\pi m_{p,n} kT}{h^2} \right)^{\frac{3}{2}} \tag{1.22}$$

where $m_{p,n}$ are the effective masses of holes and electrons. By substituting into the square of Equation (1.21) one obtains

$$n_i^2 = 4 \left(\frac{2\pi kT}{h^2} \right)^3 \left(m_p m_n \right)^{\frac{3}{2}} e^{\frac{-E_g}{kT}}. \tag{1.23}$$

These effects are reflected on the I-V characteristics of the solar cell. For the I_{sc}, the bandgap narrowing at increasing temperatures decreases the lower bound of the integral in Equation (1.14): in general, this corresponds to more photons available for the cell, but in practice this difference depends drastically on the initial value of the bandgap, as the standard solar spectrum is not a smooth curve but presents several absorption valleys from the gases in the atmosphere. Moreover, the weight of the now-available photons must also take into account reflection losses, light trapping textures and the absorption spectrum of the semiconductor. This usually results in a linear trend with a very little slope [79], which is often negligible compared to the effect on the V_{oc}.
The V_{oc} is related to I_{sc} and I_0 according to Equation (1.15) and therefore both to E_g and n_i. The temperature dependence can be evidenced by differentiating Equation (1.15) with respect to T:

$$\begin{aligned} \frac{\mathrm{d}V_{oc}}{\mathrm{d}T} &= \frac{k}{q} \ln\left(\frac{I_{sc}}{I_0} - 1 \right) + V_{th} \left(\frac{1}{I_{sc}} \frac{\mathrm{d}I_{sc}}{\mathrm{d}T} - \frac{1}{I_0} \frac{\mathrm{d}I_0}{\mathrm{d}T} \right) = \\ &= \frac{V_{oc}}{T} + V_{th} \left(\frac{1}{I_{sc}} \frac{\mathrm{d}I_{sc}}{\mathrm{d}T} - \frac{1}{I_0} \frac{\mathrm{d}I_0}{\mathrm{d}T} \right) \end{aligned} \tag{1.24}$$

As discussed in Section 1.1.1, I_0 is a measure of recombination, and is therefore sensitive to temperature changes through n_i [80]:

$$I_0 = Aq\left(\frac{D_n}{L_n N_A} + \frac{D_p}{L_p N_D}\right) n_i^2 \tag{1.25}$$

where N_A and N_D are densities of acceptor and donor atoms, $D_{n,p}$ are the diffusion constants and $L_{n,p}$ the diffusion lengths of minority carriers in the n- and p-regions, respectively. Substituting Equation (1.23):

$$I_0 = CT^3 e^{\frac{-E_g}{kT}} \tag{1.26}$$

where the constant C encloses all the constants from the previous equations as well the doping and material parameters of the p-n junction [79]. Moreover, it can be evidenced that semiconductors with a higher bandgap have a lower dark saturation current. With this expression for I_0 the relative term in Equation (1.24) becomes:

$$\frac{1}{I_0}\frac{\mathrm{d}I_0}{\mathrm{d}T} = \frac{3}{T} - \left(-\frac{E_g}{kT^2} + \frac{1}{kT}\frac{\mathrm{d}E_g}{\mathrm{d}T}\right) = \frac{3}{T} - \frac{1}{qV_{th}}\left(-\frac{E_g}{T} + \frac{\mathrm{d}E_g}{\mathrm{d}T}\right) \tag{1.27}$$

which, substituted into Equation (1.24), yields

$$\begin{aligned}\frac{\mathrm{d}V_{oc}}{\mathrm{d}T} &= \frac{V_{oc}}{T} + V_{th}\frac{1}{I_{sc}}\frac{\mathrm{d}I_{sc}}{\mathrm{d}T} - \frac{3}{T}V_{th} - \frac{E_g}{qT} + \frac{1}{q}\frac{\mathrm{d}E_g}{\mathrm{d}T} = \\ &= -\frac{\frac{E_g}{q} - V_{oc} + 3V_{th}}{T} + V_{th}\frac{1}{I_{sc}}\frac{\mathrm{d}I_{sc}}{\mathrm{d}T} + \frac{1}{q}\frac{\mathrm{d}E_g}{\mathrm{d}T}\end{aligned} \tag{1.28a}$$

The expression for $\frac{\mathrm{d}V_{oc}}{\mathrm{d}T}$ can then be obtained by substituting a model for the bandgap dependence on temperature such as those of Equations (1.19) and (1.20). Another popular model for $\frac{\mathrm{d}V_{oc}}{\mathrm{d}T}$ was introduced by Green [81, 82, 75]:

$$\frac{\mathrm{d}V_{oc}}{\mathrm{d}T} = -\frac{\frac{E_g(0)}{q} - V_{oc} + \gamma V_{th}}{T} \tag{1.28b}$$

where γ is a parameter that includes the temperature dependence of all parameters that determine the diode saturation current density, and hence contains information about the recombination mechanisms in the

cell [75, 83]. These models can be approximated to a linear dependence for the operating temperatures of PV modules [79, 81], which is usually expressed through a set of temperature coefficients α_T (%/°C) for I_{sc}, V_{oc}, Fill Factor (FF) and efficiency (η, although the term Power Conversion Efficiency, PCE, is also often used).
Temperature coefficient values for the cell architectures presented in Section 1.3 are reported in Table 1.1, with the following literature data: [84, 85, 86, 87, 88, 89, 90, 91] for SHJ, [92, 93, 86, 87, 88, 89, 90, 91] for PERC and PERT, [94, 86, 87, 89, 90] for TOPCon and [95, 91] for IBC. The SHJ cell is the one that registers the most advantageous (least negative) temperature coefficient values, especially for V_{oc} and efficiency. This derives from the fact that the recombination mechanisms generally increase with temperature. Thus, a cell with a low recombination rate and consequently high V_{oc} such as the SHJ cell, where the efficient passivation reduces the surface recombination rate, is less affected by the recombination increase at higher temperatures. Interestingly, studying the I-V characteristics of SHJ cells in a wide range of temperatures (down to -100 °C) and irradiance (down to 10 W/m^2) has shown significant deviations from the linear trend [96]: in particular, it has been evidenced that the open-circuit voltage saturates and then starts decreasing with decreasing temperature (below -50 °C). This behavior has been correlated with the apparition of an S-shape in the I–V characteristic that can be attributed to a valence band discontinuity between the c−Si absorber and the a−Si:H layer at the p-side of the device which impedes the collection of holes [97]. The effect disappears at higher temperature due to thermionic emission of holes

	$\alpha_{T,I_{sc}}$ (%/°C)	$\alpha_{T,V_{oc}}$ (%/°C)	$\alpha_{T,FF}$ (%/°C)	$\alpha_{T,\eta}$ (%/°C)
SHJ	+0.03 ÷ +0.04	-0.22 ÷ -0.25	-0.04 ÷ -0.08	-0.21 ÷ -0.30
PERC/PERT	+0.03 ÷ +0.04	-0.26 ÷ -0.37	-0.10 ÷ -0.16	-0.32 ÷ -0.41
TOPCon	+0.03 ÷ +0.05	-0.26 ÷ -0.27	-0.07 ÷ -0.12	-0.28 ÷ -0.35
IBC	+0.06	-0.25 ÷ -0.27	-0.12	-0.30 ÷ -0.38

Table 1.1: Comparison between the temperature coefficients for I_{sc}, V_{oc}, FF and efficiency of SHJ, PERC/PERT, TOPCon and IBC cells with literature data.

across the transport barrier. This transport barrier also has a similar effect on the fill factor, which reaches a maximum at temperatures between -50 °C and +10 °C, depending on the irradiance level. This results from two competing effect: a reduction associated with the decreased open-circuit voltage due to increasing recombination and an increment resulting from the increase of thermionic emission of holes across the barrier [96].

1.5 Bifacial PV

So far, it has been implicitly assumed that the solar cell is simply illuminated by the Sun on the front surface. For example, the IBC cell has been designed with the aim to maximize the active area of the front surface. However, already in 1975 the operation of a photoconverter under separate illumination levels on each side had been discussed [98], and a few years later, the first patents on bifacial cells were deposited by Luque and his group, along with research articles [99, 100, 101, 102, 103, 104]. Luque also founded the first PV manufacturer focused on bifacial cells, ISOFOTON, a start-up from the Solar Energy Institute of the Polytechnic University of Madrid [105]. Although the company switched its production to conventional monofacial cells in 1987 [106] (the company went bankrupt in 2014 "as a consequence of the Chinese price competition and a new property change"), research continued on this topic from other institutions such as Fraunhofer ISE [107] and SunPower [108]. It wasn't until the new millenium that the industry focused its attention on bifacial modules, in particular Hitachi [109], Sanyo [84] and the chinese manufacturer Yingli [110, 111]. Nowadays bifacial cells account for more than 50% of the global market share, which is expected to increase even more in the near future [34].

As bifacial PV is a relatively recent branch, cell structures and modules had previously been optimized for monofacial applications, such as the examples of Figures 1.3 and 1.5 where the rear contact is made up by a continuous metallization, or monofacial modules being characterized by a backsheet (or back surface reflector) which reflects light trying to escape the cell from the rear surface [112]. The most popular figure when comparing bifacial cells is the Bifaciality Factor BF (%), defined as the ratio

of the rear and front efficiencies when illuminated and measured independently. This in general depends on the cell structure but also on the thickness of TCO layers as well as the width and spacing of the metallic grid lines on each surface. Typical Bifaciality Factor values range between 90% and 98% for SHJ modules [113, 114, 115], between 65% and 85% for PERC/PERT modules [116, 117, 114], between 75% and 80% for TOPCon modules [118, 119] and between 70% and 75% for IBC modules [120, 114]. The SHJ cell has a higher bifaciality factor compared to the other architectures: this is due to its symmetry, as the same a−Si:H/TCO stack is deposited on both sides of the cell [121], whereas in the other cells the front and rear contacts are usually structured differently. SHJ modules, due to their high Bifaciality Factor and low temperature coefficients, are particularly suited for bifacial applications, as will be discussed in Chapter 3.

1.6 The silicon shortage crisis and the rise of other technologies

At the beginning of the millennium, the still-small scale PV industry mostly employed electronic grade silicon scraps from the semiconductor industry as feedstock material. But the heavy investments of those years drastically increased the polysilicon demand beyond the production capability of the time, inflating the price of polysilicon [122], and already in 2002 studies recognized the risks associated with the lack of an independent polysilicon supply for the PV industry [123]. On one hand, the polysilicon supply was expanded with the diffusion of the processes discussed in Section 1.2.1 (as well as Metallurgical Upgraded Silicon, UMG [122, 124]), which resulted in the crisis being overcome by 2012, as can be seen in the PV experience (or learning) curve of Figure 1.7: module price, which was mostly following a linear decreasing trend, starts to increase in 2000, reaches a maximum in 2008 (from 3 US$/Wp to 4 US$/Wp), and is realigned with the previous trend only in 2012. However, in the meantime, the geo-economical balance (or, by introducing a neologism, one could say "geo-industrial" balance) had dramatically shifted: if in the early 2000s US, Japan and Germany were leading the module pro-

duction, by 2008 a third of the modules were already being produced in China [125].

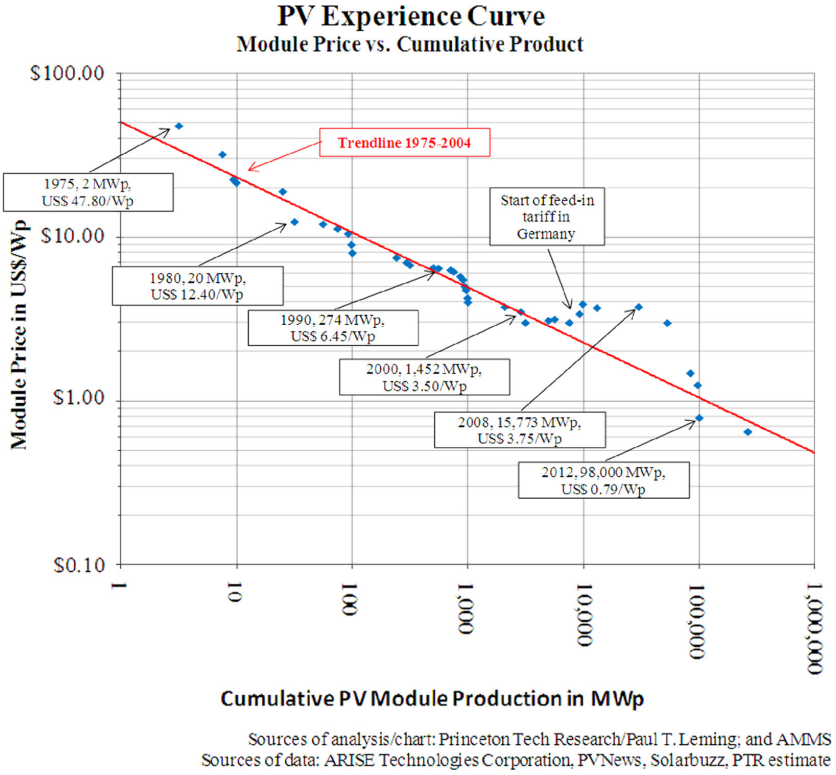

Figure 1.7: The PV experience curve, relating module price (US$/Wp) and cumulative production (MWp). Starting from 2000, module price can be seen increasing, reaching a local maximum in 2008, and the module price does not return to the linear trend until 2012. Reprinted from [122].

On the other hand, research focused its attention to alternative technologies, namely thin film solar cells: in fact, in that period the cost of the module was mostly determined by the cost of the silicon wafer, which was much thicker than in modern cells (between 250 µm and 300 µm) [126]. Thin film cells are based on highly absorbing materials, therefore can be just a few micrometers thick. This, in addition to reducing the quantity of raw material needed, also means that the electrons need to travel a much shorter distance to reach the contacts, reducing the constraints on the quality and purity of the material [125]. Moreover, another important

advantage is that thin-film solar cells are typically produced using simple and scalable low-temperature methods that are more cost-effective than the equivalent processes for silicon modules, as in thin film manufacturing many cells can be made and simultaneously assembled in a module.

1.6.1 GaAs

Gallium arsenide (GaAs) is a semiconductor of the III-IV family with a 1.42 eV direct bandgap [127]. It was one of the first thin film materials to be considered, back in 1965 on the soviet spacecrafts Venera-2 and Venera-3 directed towards Venus [128]. A first AlGaAs/GaAs prototype, with an efficiency of 9%, was presented in 1978 [129]. Since then, the technology has improved considerably, up to a record efficiency of 29.1% [130] (although the work cited by Green reports an efficiency of 27.6% [131] and is dated seven years prior the test date reported in the table by Green), close to its theoretical efficiency of 35.3% [132] and highest among all single-junction cells. However, due to its extremely high costs, it is still only employed in specific high-performance applications, such as space PV [126, 133].

1.6.2 Amorphous silicon

Many semiconductors, such as Si, Ge and the aforementioned GaAs are characterized by a crystalline lattice: *i.e.*, diamond cubic, made up by two interpenetrating face-centered cubic (FCC) lattices, in Si and Ge or zincblend in GaAs. There are also many noncrystalline semiconductors in which the chemical bonding is technically the same as in crystals but a disorderly variation in the angles between bonds eliminates the regular lattice structure. In these materials the conduction and valence band present localized tail states following an exponential distribution: this causes a characteristic exponential tail in the absorption spectrum, called "Urbach tail" [134, 135]. The mobility edge is defined as the energy separating localized and non-localized states in the respective bands, and in analogy with crystalline semiconductors, the mobility gap is defined as the differences between the two edges, which is usually measured by Tauc plot analysis.

In amorphous silicon, the characteristic energies of the band tail have been measured as 43 meV for the valence band tail and 27 meV for the conduction band tail [136] and the mobility gap resulted of about 1.75 eV [134, 126]. The earliest amorphous silicon solar cell dates back to 1976, with an efficiency of 2.4% [137]. A technology breakthrough was represented by the discovery that plasma-deposited a−Si contained a significant percentage of hydrogen atoms, which passivated the dangling bonds reducing their density by about three orders of magnitude [134, 138]. Another important contribution came from Staebler and Wronski, which discovered the effect named after them in 1977 [139]: the authors observed a decrease in conductivity of about four orders of magnitude in samples illuminated by light with an irradiance of 200 mW/cm^2 for about four hours. This light-induced degradation (LID) could be reversed by annealing at about 150 °C. The effect is often mitigated by reducing the layer thickness, but this also affect light absorption [126, 138]. Currently, single-junction a−Si:H cells achieved a record stabilized efficiency above 10%, but LID limits the competitiveness of this technology.

1.6.3 Microcrystalline and polycrystalline silicon

One attractive feature of the a-Si:H technology is that after the low-temperature deposition processes no other treatments are necessary, and the research aimed at preserving this feature while increasing efficiency and stability. In 1994, the University of Neuchatel fabricated ny very high frequency PECVD the first hydrogenated microcrystalline silicon (µc-Si:H) cell, with a stable efficiency of 4.6% [140]. Efficiency quickly improved to 8.5% [141], but the technology found its most successful application in tandem devices with amorphous silicon (which will be later named "micromorph" [142]), with efficiency of 9.1% without LID already in 1994 [143]. The Japanese company Kaneka then lead the development of this technology, achieving a stable efficiency of 11% in 2004 [142].
A few years after the development of the first µc-Si cell, Sanyo Electric co. reported on the fabrication of the first polycrystalline silicon cell by solid phase crystallization, with an efficiency of 9.2% [144]. This activity was then continued by Pacific Solar Pty Ltd, a spin-off company of the University of New South Wales (UNSW), which introduced the so-called

(poly)crystalline silicon on glass (CSG) and reached an efficiency of 10.4% in 2007 [145].
However, due to their limited efficiency and eventually competitive costs of bulk silicon, both the micromorph and polycrystalline thin film techonology remained quite limited in terms of market share [146, 147].

1.6.4 CIGS

Copper Indium Gallium Selenide (CIGS) is a solid solution of Copper Indium Selenide (CIS) and Copper Gallium Selenide (CGS), with chemical formula $CuIn_xGa_{1-x}Se_2$ and the crystal structure of chalcopyrite. Both its refractive index [148] and its bandgap depend on the indium and gallium concentrations: in fact, being x the indium concentration as reported above [149],

$$E_g = 1.04 + 0.65x - bx(1-x) \tag{1.29}$$

where b is the so-called bowing parameter, although several estimates for b and for the other constants have been presented in the literature [150, 151, 152, 153]. In general, the bandgap of CIGS ranges from about 1 eV ($x = 0$) to about 1.7 eV ($x = 1$).
Historically, the first studies were carried out on CIS in the '70s, but the first devices were actually CdS/CIS heterojunction, with an efficiency of about 5% [154, 155]. However, in 1981 Boeing presented a 9.4% efficient device [156], and in the following years Boeing and ARCO Solar contributed to the growth of the technology, developing coevaporation and precursor reactions processes to produce CIGS devices [149]. The research also focused on the surface sulfurization [157] and on the buffer layer, studying several alternative materials to CdS, and the highest efficiency achieved is of 23.35% [158]. However, the market share of CIGS remains limited even among the other thin-film technologies, and several CIGS manufacturer, such as Solyndra, went bankrupt after c-Si recovered its competitiveness after the shortage crisis [159].

1.6.5 CdTe

Due to its 1.5 eV bandgap being quite close to the optimal match for the solar spectrum, the research on cadmium telluride (CdTe) had already

started in the '50s and efficiencies between 2% and 6% were reported in that period [160, 161]. Similarly to the other materials introduced in this Section, CdTe has been mainly investigated in the context of heterojunctions, but considering that CdTe is already close to the optimal bandgap, most of the absorption should occur at the level of CdTe, thus limiting the range of partner materials to high-bandgap films with small lattice mismatch with CdTe and as little element diffusion as possible. N-type CdTe has been coupled with Cu_2Te, reaching an efficiency of 7% in 1973 [162], but stability issues and lack of further potential growth shifted the attention towards p-type CdTe with CdS, ZnO and ZnSe [163].
Two main fabrication configurations have been designed: in the first one, the superstrate configuration, the layers are deposited on a glass support, starting from the front TCO towards the bottom contact, so that light will have to go through the glass before reaching the cell. Then, the substrate cell was introduced, where the layers are deposited from bottom to top on an opaque substrate. Of the two, the superstrate configuration has seen more success both in terms of higher efficiency and industrial diffusion [160, 164].
Improved deposition processes, such as the Closed Space Sublimation (CSS), and reduced contact resistance thanks to SnO_2 lead to a record efficiency of 15.8% in 1993 [165]. However, for two decades the technology saw little improvement, up to a record of 17.3% achieved by First solar in 2012 [166]. Since then, this technology has seen a new positive phase, with efficiency reaching 22.1% [130]. Among the new solutions that have been implemented, the CdSe layer has higher solubility in CdTe than CdS, with this interdiffusion creating $CdTe_{1-x}Se_x$ alloys with graded bandgaps below the bandgap of CdTe, enhancing the absorption at larger wavelengths [166, 167]. Additionally, MgZnO (MZO) provides a better band alignment with TCOs such as FTO [166].
CdTe has also seen a considerable impact on the PV industry, due to its high stability and to the fact that there are already several processes able to produce high-quality and large-area modules, such as CSS, physical vapor deposition (PVD), electrodeposition and screen-printing [126], and is currently the second most diffused PV technology (currently representing 5% of the world market).

1.6.6 Dye-sensitized solar cells

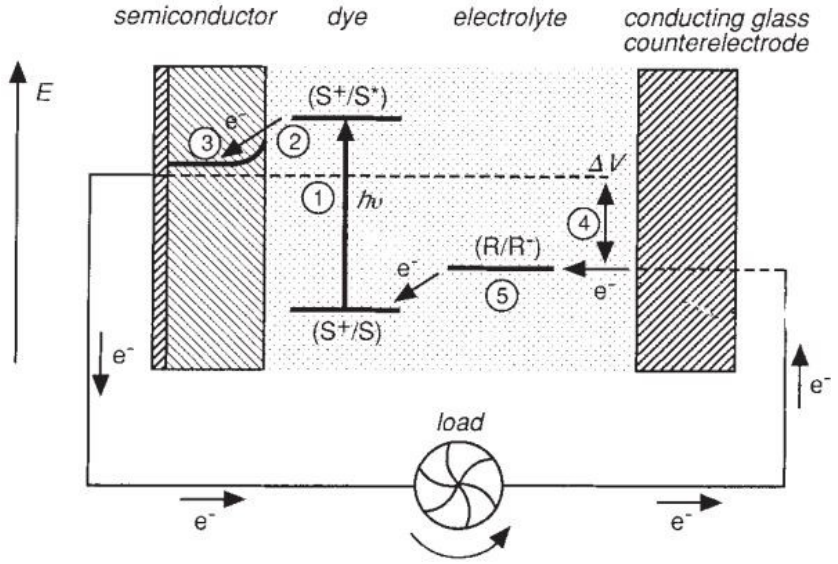

Figure 1.8: Schematic representation of the operating principle of a DSSC: the photon is absorbed by the sensitizer S, the produced electron is collected by the semiconductor and delivers power to the load. The circuit is closed by the electrolyte, obtaining a voltage ΔV. Reprinted from [168].

The main components of a Dye-Sensitized Solar Cell (DSSC) are a thin nanocrystalline semiconductor electrode formed onto a TCO-coated electrode, a sensitizer (dye) adsorbed on the surface of the nanocrystalline semiconductor, an electrolyte containing redox ions and a counter electrode. First, a sensitizer molecule absorbs the incident photons and is excited from the ground state (S) to the excited state (S*). Then, the electron diffuses through the semiconductor towards the TCO-coated electrode. The oxidized sensitizer is reduced by the ions in the electrolyte, regenerating the ground state of sensitizer, while the oxidized ions diffuse towards the counter-electrode to be reduced (Figure 1.8). The open-circuit voltage of the cell is determined by the difference between the Fermi level of the semiconductor and the redox potential of the electrolyte, while the energy gap between the Highest Occupied Molecular Orbital (HOMO) and the Lowest Unoccupied Molecular Orbital (LUMO) of the sensitizer

determines the wavelength sensitivity range (representing the bandgap of a solid-state semiconductor). But, in order to have a driving force for the electron, the LUMO must have higher energy than the conduction band of the semiconductor, thus reducing the voltage output of the cell (Figure 1.8). The small size of the semiconductor nanoparticles increase the surface area by a roughness factor (usually higher than 1000), increasing the amount of adsorbed dye for a more efficient light absorption.
Research on the topic of dye-sensitized semiconductor began in the '60s, but only two decades later it was recognized that the dye could function most efficiently if chemisorbed on the surface of semiconductor nanoparticles [169, 170]. Titanium dioxide (TiO_2) quickly became the semiconductor of choice for the photoelectrode due to its low-cost, wide availability and safety, and in 1991 a 7.1% cell was announced [168] with nanostructured TiO_2, a ruthenium complex-based dye and a iodine-based electrolyte. Recent cells have achieved efficiencies of 13.5% with Cu-based electrolytes [171] and of 14.3% with organosilicon compound dyes and cobalt electrolytes [172].
However, this technology is held back mainly by light induced degradation and sealing problems, as this must take into account the thermal expansion of the liquid electrolyte. Moreover, another drawback is represented by Volatile Organic Compounds (VOC), solvents typically contained in the electrolyte solution which must be carefully sealed as they are hazardous to human health and the environment [173].

1.6.7 Perovskite

By definition, a perovskite (PVK) is any material with the crystal structure ABX_3, where A is a large cation, B a small inorganic cation and X is an anion bonding the two. This structure is typical of the namesake mineral (calcium titanate, $CaTiO_3$), discovered in the Ural mountains in 1839 and named after the Russian mineralogist Lev Perovski, and it has been characterized by X-ray diffraction on barium titanate in 1945 [174]. The first application of perovskites for photovoltaic application was reported in 2009 [175], when $CH_3NH_3PbBr_3$ and $CH_3NH_3PbI_3$ have been studied as sensitizers for TiO_2 photoelectrochemical cells, with an efficiency of 3.8%. In that system, the efficiency was limited by the iodine electrolyte

which corroded the perovskite [176]. In 2011 efficiency was improved to 6.5% and stability to 10 min (80% degradation) [177].
The following year the paradigm was changed as Lee *et al.* reported on a solution-processable solar cell in which a mixed-halide perovskite ($CH_3NH_3PbI_2Cl$) was used as the absorber, but the liquid electrolyte had been replaced with an organic hole-transport material (spiro-OMeTAD), improving the efficiency to 10.9% [178]. Further improvements came with the replacement of mesoporous TiO_2 with an insulating Al_2O_3 scaffold within which the perovskite is infiltrated, with efficiency up to 13.5% [179]; additionally, full films with no scaffolding were obtained, with an efficiency of 11.4% [180]. In the last years, the technology has continued to improve, up to above 24% efficiency and 87% efficiency retention after 500 hours [181] for single-junction cells; in fact, PVK are often considered for multi-junction modules, for which efficiencies above 30% have been reached [182].
The employment of PVK in tandem cells derives from one of its most appealing characteristics, that is, the possibility to tune its bandgap. This is usually done by substitution: for example, $MAPbI_3$ and $MASnI_3$ exhibit a sharp absorption peak at about 1.50 eV, but this can be reduced by 0.07 eV by replacing methylammonium (MA) with formamidinium. The bandgap range can be quite wide, as the partial substitution of Pb with Sn can alter the bandgap of $CH_3NH_3PbI_3$ from 1.17 eV to 1.55 eV [183].
The biggest challenge for the industrial development of PVK is its stability, as PVK cells are still far from the 30-year lifetime of c-Si modules [184], which is especially important for the aforementioned multi-junction applications. The instability of PVK is mainly related to environmental factors such as humidity, thermal stress, intrinsic stability of the materials and LID [185]. Moreover, PVK cells show remarkable hysteresis between forward and backward I-V scans, with various causes proposed such as ion movement, polarization or ferroelectric effects [183]. Lastly, another core problem in the production and deployment of perovskite solar cells is their recyclability, which is necessary due to the presence of lead in most high efficiency perovskites. In fact, lead represents a severe risk for human health and environment pollution, and its use is strictly regulated in many countries [186]. Therefore, research is actively focusing on preventing lead leakage and developing efficient lead-free perovskites.

Chapter 2

Solar cell modeling

2.1 An analytical method for solar cell optics

When dealing with the optics of solar cells, one is usually interested in determining how much light is reflected or transmitted by the cells and how much it is absorbed and in which layer, with the intention to minimize the former and maximize the latter. From the point of view of optics, a solar cell can be considered as a multilayered dielectric system, and it can therefore be analyzed with methods initially developed for these systems, such as the transfer matrix method.
Whenever a plane wave meets a layered medium, it is partly reflected and transmitted not only at the surface of the system but also at each interface inside the medium, and the resulting electromagnetic field in the system derives from infinite contributions. The calculation of these contributions can still be brute-forced if the number of layers is sufficiently small, but alternative approaches are preferred for more complex systems. Given U^+ the sum of the forward-traveling waves and U^- the sum of the backward-traveling waves, an optical element can be described as a 2 x 2 matricial operator $M = \begin{pmatrix} A & B \\ C & D \end{pmatrix}$ acting on the column vector, that is:

$$\begin{pmatrix} U_2^+ \\ U_2^- \end{pmatrix} = \begin{pmatrix} A & B \\ C & D \end{pmatrix} \begin{pmatrix} U_1^+ \\ U_1^- \end{pmatrix} \tag{2.1}$$

where the subscripts 1 and 2 indicate the waves before and after the optical element, respectively [187]. In this approach, a layered medium can be expressed as a product of m operators $M_m \cdot M_{m-1} \cdot ... \cdot M_1 \cdot M_0$. Another useful operator to consider is the scattering matrix $S = \begin{pmatrix} t_{12} & r_{21} \\ r_{12} & t_{12} \end{pmatrix}$, where the quantities r_{ij} and t_{ij} represent the amplitude reflectance and transmittance coefficients from layer i to layer j, respectively. While the elements of the S matrix have a direct physical meaning, the matrices of single elements cannot be combined to obtain the matrix of the whole system like with the M matrices, but one can calculate the global transfer matrix from the matrices of each layer first and then convert it to a scattering matrix through the following relationships:

$$M = \begin{pmatrix} A & B \\ C & D \end{pmatrix} = \frac{1}{t_{21}} \begin{pmatrix} t_{12}t_{21} - r_{12}r_{21} & r_{21} \\ -r_{12} & 1 \end{pmatrix}, \tag{2.2a}$$

$$S = \begin{pmatrix} t_{12} & r_{21} \\ r_{12} & t_{12} \end{pmatrix} = \frac{1}{D} \begin{pmatrix} AD - BC & B \\ -C & 1 \end{pmatrix}. \tag{2.2b}$$

The M matrix for light propagation in the bulk of a layer is given by:

$$M = \begin{pmatrix} e^{-i\frac{2\pi\tilde{n}d}{\lambda}} & 0 \\ 0 & e^{i\frac{2\pi\tilde{n}d}{\lambda}} \end{pmatrix} \tag{2.3}$$

where $\tilde{n} = n + ik$ is the complex refractive index of the material, and this operator incorporates both the phase shift and the wave attenuation in the material. For a wave incident on a surface, given θ_1 the incidence angle and θ_2 the transmitted wave angle determined by Snell's law, the operator M assumes the following form:

$$M = \frac{1}{a_{21}n_2^*} \begin{pmatrix} n_1^* + n_2^* & n_2^* - n_1^* \\ n_1^* - n_2^* & n_1^* + n_2^* \end{pmatrix} \tag{2.4}$$

where for the S or transverse electric polarization $a_{ij} = 1$ and $n_i^* = n_i cos\theta_i$ while for the P or transverse magnetic polarization $a_{ij} = \frac{cos\theta_i}{cos\theta_j}$ and $n_i^* = n_i sec\theta_i$.

Once the global S matrix has been determined, the intensity reflectance $R_{+,-}$ is given by $|r_{0m,m0}|^2$ for forward and backward waves and the intensity transmittance $T_{+,-}$ is given by $\frac{n_j cos\theta_j}{n_i cos\theta_i}|t_{0m,m0}|^2$ [188].

2.2 Computational methods

As discussed in the previous Section 1.1.2, single-junction Si PV has a theoretical limit of about 29.4% [189], and multi-junction modules represent a promising alternative to overcome this limit. However, even when restricting the bottom semiconductor to Silicon, there is a variety of possible candidates for the top semiconductor that can be considered, such as GaAs, CdTe, CIGS and perovskites [190]. Moreover, for each configuration several additional levels of variability should be adapted for optimal performance, such as the choice of TCOs, buffer layers and tunnel junctions for the case of tandem devices. Lastly, the thickness of each layer should be varied in order to achieve the current matching needed in order to maximize the performance gain in series-connected devices. Therefore, designing a multi-junction module is a task which can be greatly accelerated by computational physics.

In the general context of solar cell simulation, several tools have been developed over the years: one of the first to be introduced is PC1D, with the earliest versions dating before 1990 [191, 192]. However, in 2011 an upgraded version was published as a new program called PC2D [193], which implemented the numerical solution of the two-dimensional drift diffusion equations in order to account for effects in PERC and IBC cells that were not accurately modeled by its one-dimensional predecessor. Then, in 2019 PC3D was published, with an improved optical model suited for the randomized pyramidal texture commonly found in silicon cells [194].

Among the earliest simulation tools, SCAPS is a one-dimensional program, introduced in 1998, designed for thin-film CdTe and CIGS cells [195], with a focus on electrical properties of the system such as tunneling [196], graded bandgaps [197] (which consists in varying the concentration of gallium and selenium along the layer to obtain spatially tuned electronic properties) and defects [198, 199].

Other simulation tools include CoBoGUI, a MATLAB-based graphical user interface to manage two-dimensional simulations performed in COMSOL Multiphysics [200], wxAMPS, an improved version of an older semiconductor devices simulator called AMPS [201] and Quokka, introduced in 2012 as an alternative with wider availability than CoBoGUI and better

performance than PC2D [202].
Another software to be mentioned is the set of TCAD tools designed by Silvaco, which are mostly used for the development of semiconductor devices: regarding solar cells, the ATLAS tool has been used to design and optimize traditional silicon solar cells as well as thin-film and multi-junction cells [203, 204, 205].
Within my research activity, I have developed a Monte Carlo simulation code that has been applied to optimize a voltage-matched 2T module in different configurations [206]. This has been preferred to software already available as writing your own simulation tool gives you complete control on the physics of the process, whereas the description of tools in the literature such as those presented above is not always complete.

2.2.1 Solar cell modelling in Python

In general, Monte Carlo simulation is an effective approach to obtain information from a system when the underlying fundamental physical laws governing the system are known but the overall dynamics is much more complex due to the size of the system or the number of agents in it. In solar cells, a complete simulation of the system must include two different sections: the optical simulation to determine the absorption of photons and the electrical simulation to determine the collection of carriers.
For the optical part, the interaction between photons and bulk materials is expressed by the Beer-Lambert law:

$$I_T(\lambda) = I_0(\lambda) \cdot e^{(-\alpha(\lambda)d)} \tag{2.5}$$

where λ is the wavelength of the radiation, d is the length of material considered, $\alpha(\lambda)$ is the absorption coefficient of the material and I_0 and I_T are the intensities of the incident and transmitted radiation, respectively. In turn, $\alpha(\lambda)$ is defined as $\alpha(\lambda) = \frac{4\pi k}{\lambda}$, where $k(\lambda)$ is the imaginary part of the complex refractive index of the material.
As for the interfaces between different materials, a photon can either be reflected away or transmitted through, according to the Fresnel equations:

$$r_s = \frac{n_1 cos\theta_i - n_2 cos\theta_t}{n_1 cos\theta_i + n_2 cos\theta_t} \tag{2.6a}$$

$$t_s = \frac{2n_1 cos\theta_i}{n_1 cos\theta_i + n_2 cos\theta_t} \tag{2.6b}$$

$$r_p = \frac{n_2 cos\theta_i - n_1 cos\theta_t}{n_2 cos\theta_i + n_1 cos\theta_t} \tag{2.6c}$$

$$t_p = \frac{2n_1 cos\theta_i}{n_2 cos\theta_i + n_1 cos\theta_t} \tag{2.6d}$$

where Equations (2.6a) and (2.6b) give the coefficient for the S polarization and Equations (2.6c) and (2.6d) give the coefficients for the P polarization. However, employing these equations in the case of lossy media with complex refractive indices can lead to a great confusion, as most textbooks claim that these equations can be generalized simply by converting the real quantity n into a complex number, while recent literature challenged these claims [207, 208, 209]. For this reasons, even within a Monte Carlo simulation, I opted for using the transfer matrix method described in Section 2.1 to determine the reflectance and transmittance at each interface.
The last physical law concerning the optics simulation is Snell's law, which determines the traveling angle of transmitted light with respect to the normal of the interface:

$$n_1 sin\theta_i = n_2 sin\theta_t \tag{2.7}$$

As for the electric simulation, this depends on the drift-diffusion process and on recombination processes such as Shockley-Read-Hall, Auger, radiative recombination and surface recombination due to dangling bonds, some of which have already been discussed in Chapter 1. The SQ limit is an ideal condition, in which recombination is assumed to be minimal; on the contrary, these loss mechanisms tend to increase the dark saturation current and limit the voltage output of the solar cell. In general, the weights of these phenomena depend on a number of material-dependent parameters as well as on the cell design: for this reason, as the case study of [206] consists in a comparison of several materials including perovskites, which collectively form a large family of semiconductors with different electrical properties, a "condensed" approach has been preferred to keep the Monte Carlo simulation as widely applicable as possible, even to new materials and cell designs whose electric properties

or loss mechanisms might not be well-documented in the literature. The condensed approach consists in comparing the open-circuit voltage obtained from the J-V (current density - voltage) characteristics in the ideal case of the detailed balance limit of Shockley and Queisser ($V_{oc,SQ}$) discussed in Section 1.1.1 with the value achieved with the top cell reported in [130] ($V_{oc,SA}$, where the subscript SA stands for state-of-the-art) for the same semiconductor, from which a Technology Development Coefficient (TDC) can be defined as:

$$TDC = \frac{V_{oc,SA}}{V_{oc,SQ}} \tag{2.8}$$

This coefficient expresses all the processes that reduce the V_{oc} of the cell but only depends on the bandgap of the semiconductor. Once the J-V characteristics of the system has been determined from the absorbances resulting from the optical simulation, the TDC can be used to modify the dark saturation current J_0. Starting from the J-V characteristics at open-circuit condition:

$$0 = J_{sc} - J_0 \left(e^{\frac{qV_{oc}}{k_B T}} - 1 \right) \tag{2.9}$$

one can obtain the dark saturation current density in the Shockley-Queisser limit:

$$J_{0,SQ} = \frac{J_{sc,SQ}}{e^{\frac{qV_{oc,SQ}}{k_B T}} - 1} \tag{2.10}$$

where the subscript SQ has been added to differentiate from the following expression for the state-of-the-art cell, for which the relation $V_{oc,SA} = V_{oc,SQ} \cdot TDC$ is valid by definition, obtaining:

$$J_{0,SA} = \frac{J_{sc,SQ}}{e^{\frac{qV_{oc,SQ}TDC}{k_B T}} - 1} \tag{2.11}$$

It has to be noted that in this last expression the short-circuity current density is still the SQ limit value: this is because the purpose of the TDC is to summarize all the phenomena affecting the carrier collection, therefore the assumption that the cell can absorb all the incident light in the

SQ limit should not influence the application of the TDC. Therefore, the ratio between the dark saturation current densities in the two case is:

$$\frac{J_{0,SA}}{J_{0,SQ}} = \frac{J_{sc,SQ}}{e^{\frac{qV_{oc,SQ}TDC}{k_BT}} - 1} \cdot \frac{e^{\frac{qV_{oc,SQ}}{k_BT}} - 1}{J_{sc,SQ}} \tag{2.12}$$

and it follows that:

$$J_{0,SA} = J_{0,SQ} \frac{e^{\frac{qV_{oc,SQ}}{k_BT}} - 1}{e^{\frac{qV_{oc,SQ}TDC}{k_BT}} - 1} \tag{2.13}$$

therefore the J-V characteristic of a state-of-the-art cell can be derived from the J-V characteristics of the same cell in the SQ limit by adjusting the dark saturation current density by the factor in Equation (2.13).
In the simulation, once the J-V characteristics of each cell has been determined, a suitable number of cells n_c must be connected in series for both semiconductors in order to match the voltage outputs, with $n_{c,top}$ being generally different from $n_{c,bottom}$. Assuming that all cells are identical to each other and illuminated evenly, the current output of each module will be equal to the current of a single cell and its voltage output equal to the output of a single cell multiplied by the same factor. Then, the J-V characteristics of the whole multi-junction system can be obtained by adding the currents produced by the two modules at each voltage point. In summary, the only inputs of the model are the refractive indices of each layer and the specifics of any textured surface.
The model has been used to evaluate the power conversion efficiency (PCE) of four voltage-matched two-terminal (VM2T) modules: GaAs/Si, CdTe/Si, $CuIn_{1-x}Ga_xSe_2$/Si (and in particular the case for $x = 1$, which will be referred to as CGS in the rest of this work) and PVK/Si. The system is made up by 11 layers, as shown in Figure 2.1: the outermost layers are semi-infinite air layers ($j = 1$) and the multi-junction system is encapsulated in a 4 mm thick glass layer ($n = 1.5$) on both sides. The top cell has two Al-doped ZnO (AZO) anti-reflection layers at the top and at the bottom: this material has been chosen for its relatively cheap cost that does not include indium [210]. The two modules are separated by a dielectric interlayer with $n = 1.5$, like glass [211] or polymeric films such as PMMA [212]. For the bottom cell, an SHJ cell has been considered, but

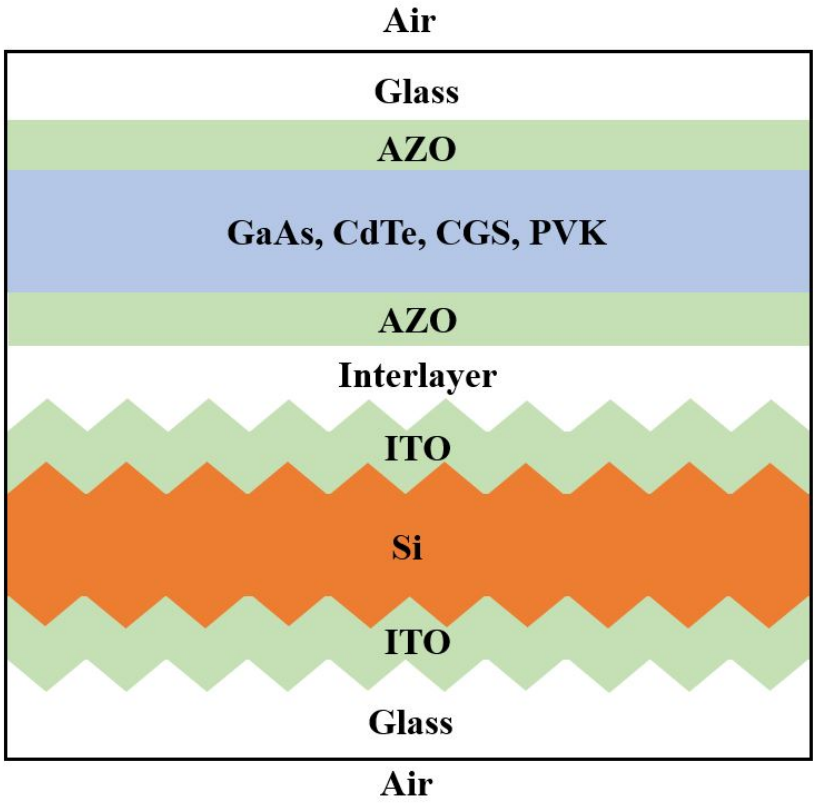

Figure 2.1: Diagram of the multi-junction system modeled in [206], indicating the flat module at the top in contrast with the textured module at the bottom.

the amorphous silicon layers have been neglected. The SHJ cell presents a texturization made up by regular pyramids, although random pyramids can also be simulated by the model. The TCO layers in the SHJ cells are made of In_2O_3:Sn (ITO), as this is the most diffused TCO in industrial production [210]. The literature data on the refractive indices of these material are reported in [213, 19, 214, 215, 216, 148].

Some of the thicknesses of specific layers in the system are fixed: in particular, the Si layer is 160 µm thick and the second ITO layer underneath is 80 nm thick. The height of the Si pyramids on both sides is 1 µm, and both glass layers are 4 mm thick. These values are typical in current state-of-the-art SHJ cells [34, 217, 218]. All the other thicknesses

were allowed to vary, with the thicknesses of the AZO layers in the top module and of the top ITO layer in the Si module ranging from 40 to 200 nm, while the semiconductor layer thickness ranged from 0.1 µm to 4 µm. Moreover, the interlayer thickness was allowed to vary from 50 µm to 300 µm. As the distance between lines in the metal grid contact are usually in the order of millimeters [219], the model needs to be able to simulate large surfaces, and in order to do that a unit cell is defined by considering the (110) planes that include the base of the pyramids in the textured Si surface, while the faces of the pyramids lie on the (111) planes. The origin of the coordinate system lies at the center of the base of the Si upward pyramid. This cell can be repeated infinitely along the x and y direction by applying periodic boundary conditions, and this approach allows the simulation of a large number of pyramids, as demonstrated in [220].
For each wavelength in the 300 nm – 1200 nm range (with a 10 nm step), 1000 photons have been simulated. At each iteration, the photon is initialized with a random position $\vec{p} = (p_x, p_y, p_z)$ and an initial velocity $\vec{v} = (0, 0, -1)$ in the first air layer. Each photon travels linearly and is tracked until it is either completely reflected away from the system, transmitted through the last air layer beyond the system or absorbed in one of its layers. At each iteration the software checks the current layer in which the photon is traveling, then, based on the position of the photon with respect to the nearest surfaces, the following steps are carried out:

- if the photon is traveling through an absorbing medium, an absorption probability $a(\lambda) = 1 - e^{-\alpha_j \frac{l_j}{cos\theta}}$ is calculated, with α_j being the absorption coefficient defined by Lambert–Beer's Law for the j-th layer, l_j its thickness and θ the angle between $\vec{v}$ and the (0,0,1) direction. A random number is generated to determine whether the photon is actually absorbed into the current layer or not. In the former case, a new iteration is initialized, whereas in the latter case, the position of the photon is updated by moving for a distance $\frac{l_j}{cos\theta}$ along $\vec{v}$ and the iteration continues;

- whenever the photon reaches an interface, reflection and transmission probabilities are calculated with the transfer matrix method as previously stated and a random number is generated to determine if

the photon is reflected or transmitted. In the former case, the photon remains in the current layer and its direction is updated according to [221]: being $\hat{n}$ the normal to the surface, the normal component of $\vec{v}$ with respect to the surface can be found by projecting on $\hat{n}$:

$$\vec{v}_\perp = (\vec{v} \cdot \hat{n})\,\hat{n} \tag{2.14}$$

while the parallel component can be obtained by difference:

$$\vec{v}_\parallel = \vec{v} - \vec{v}_\perp. \tag{2.15}$$

From the properties of the reflected direction $\vec{r}$ it is clear that $\vec{r}_\parallel = \vec{v}_\parallel$, while $\vec{r}_\perp = -\vec{v}_\perp$, therefore:

$$\vec{r} = \vec{v}_\parallel - \vec{v}_\perp = \vec{v} - (\vec{v} \cdot \hat{n})\,\hat{n} - (\vec{v} \cdot \hat{n})\,\hat{n} = \vec{v} - 2\,(\vec{v} \cdot \hat{n})\,\hat{n}. \tag{2.16}$$

For the transmitted direction, considering

$$\sin(\theta_i) = \frac{\left\|\vec{v}_\parallel\right\|}{\|\vec{v}\|} = \left\|\vec{v}_\parallel\right\| \tag{2.17}$$

where the last equality holds as $\|\vec{v}\| = 1$ at all times (this is valid for all the other vectors in the simulation), and that from Snell's law

$$\sin(\theta_t) = \frac{n_1}{n_2}\sin(\theta_i), \tag{2.18}$$

it follows that

$$\left\|\vec{t}_\parallel\right\| = \frac{n_1}{n_2}\left\|\vec{v}_\parallel\right\| \tag{2.19}$$

for the norm of the vectors, whereas for the vector themselves, given that $\|\vec{v}_\perp\| = \cos(\theta_i)$ but that $\vec{v}_\perp$ and $\hat{n}$ are antiparallel, it follows from Equation (2.15) that

$$\vec{t}_\parallel = \frac{n_1}{n_2}\left[\vec{v} + \cos(\theta_i)\hat{n}\right]. \tag{2.20}$$

For the perpendicular component, by Pythagora's theorem

$$\vec{t}_\perp = -\sqrt{\|\vec{t}\| - \left\|\vec{t}_\parallel\right\|^2}\,\hat{n} = -\sqrt{1 - \left\|\vec{t}_\parallel\right\|^2}\,\hat{n} \tag{2.21}$$

as all vectors are normalized; adding the two components together, regrouping the terms by their direction and using Equation (2.17),

$$\vec{t} = \frac{n_1}{n_2}\vec{v} + \left(\frac{n_1}{n_2}\cos(\theta_i) - \sqrt{1 - \sin^2(\theta_t)}\right)\hat{n} \tag{2.22}$$

where $\sin^2(\theta_t)$ can be obtained from Snell's law

$$\sin^2(\theta_t) = \left(\frac{n_2}{n_1}\right)^2 \sin^2(\theta_i) = \left(\frac{n_2}{n_1}\right)^2 \left(1 - \cos^2(\theta_i)\right); \tag{2.23}$$

- when the photon approaches a pyramid, that is, when p_z is in the range of z values of the points of the pyramid, the intersections between the $\vec{v}$ and the faces of both the pyramid and the unit cell are calculated, if present. In general, a plane can be represented by a set of points $\vec{u}$ for which

$$(\vec{u} - \vec{u_0}) \cdot \hat{n} = 0 \tag{2.24}$$

where $\hat{n}$ is again a normal vector to the plane and $\vec{u_0}$ a point in the plane, while the trajectory followed by the photon can be expressed as

$$\vec{p} = \vec{p_0} + d\vec{v} \tag{2.25}$$

where $\vec{p_0}$ is the starting point of the photon and $d \in \Re$. Looking for the intersections between these objects corresponds to looking for the points satisfying both equations, therefore by substitution:

$$(\vec{p_0} + d\vec{v} - \vec{u_0}) \cdot \hat{n} = 0. \tag{2.26}$$

Rearranging the terms gives

$$(\vec{v} \cdot \hat{n})\, d + (\vec{p_0} - \vec{u_0}) \cdot \hat{n} = 0 \tag{2.27}$$

and solving for d

$$d = \frac{(\vec{u_0} - \vec{p_0}) \cdot \hat{n}}{\vec{v} \cdot \hat{n}}. \tag{2.28}$$

After all the intersections have been found, only those for which $d > 0$ are valid, as the photon is traveling forward; moreover, since

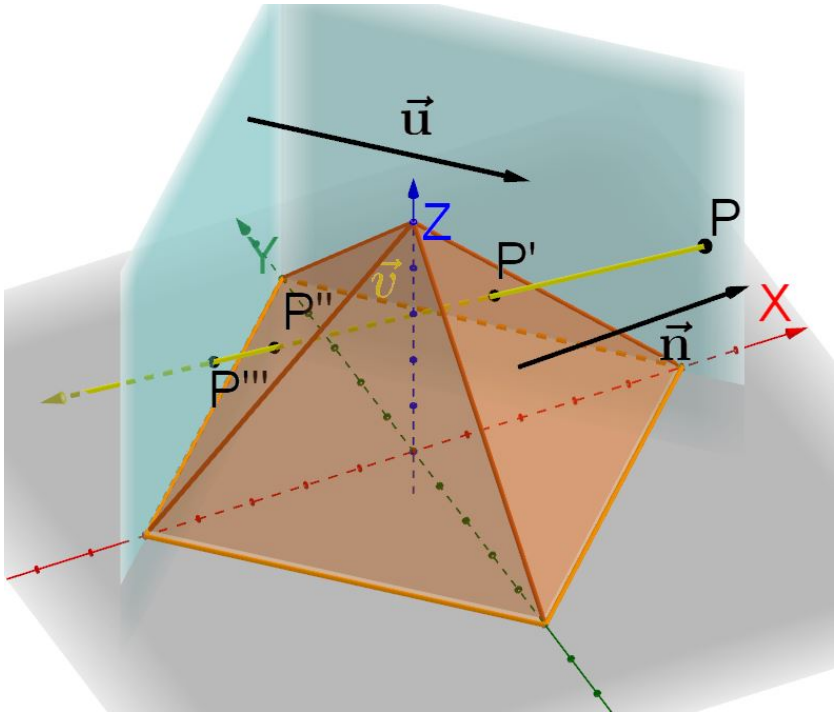

Figure 2.2: Representation of the unit cell. For simplicity, only two of the vertical planes of the boundary of the cell are shown, represented by the vector $\vec{u}$. From the starting position $\vec{p}$, the photon direction $\vec{v}$ intersects two faces of the pyramid (vector $\vec{n}$) and a boundary plane in $\vec{p'}$, $\vec{p''}$ and $\vec{p'''}$, respectively.

planes are by definition infinite whereas the faces of the pyramids are finite, it must be checked that the intersections with the faces of the pyramid lie on the corresponding quadrants. Then, the closest point is selected as shown in Figure 2.2 and, if the photon is traveling through an absorbing medium, a new absorption event is carried out as described above, with d calculated as from Equation (2.28). If the ray has not been absorbed and the new position $\vec{p}$ lies on a face of the pyramid, a new reflection/transmission event is carried out, whereas if it lies on the face of the unit cell, periodic boundary conditions are applied and the position is updated as

$$\vec{p'} = \vec{p} + s\hat{n} \tag{2.29}$$

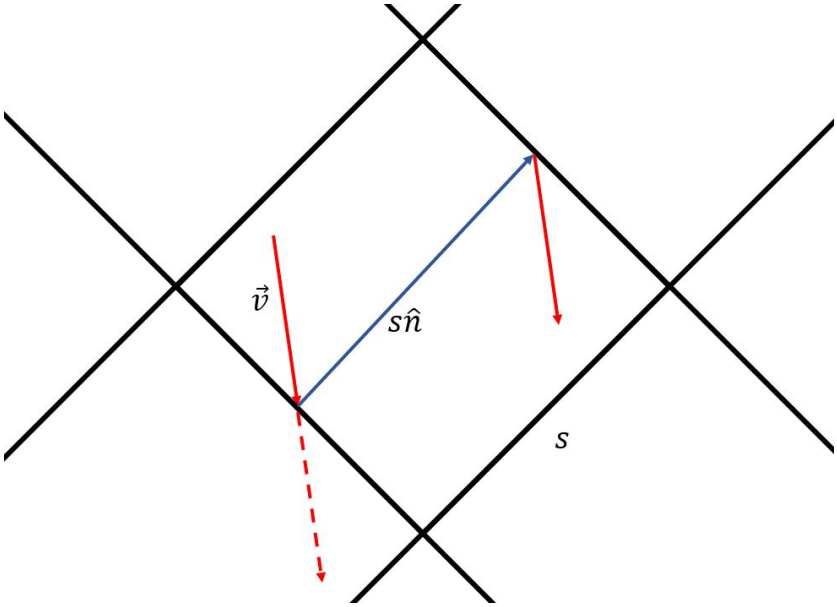

Figure 2.3: Schematic representation of how boundary conditions are applied. The direction of the photon is preserved, while the position is updated to where it would be in the next unit cell.

where $\hat{n}$ is the unit vector perpendicular to the plane pointing inwards and s is the length of the edge of the base of the pyramid, as illustrated in Figure 2.3;

- if the photon travels from one surface of the Si layer to the other without being absorbed or back and forth through the dieletric slab, its p_x and p_y will be randomized with respect to the new pyramid that the photon approaches. This step reflects the fact that the chemical etching of the silicon wafer in industrial processes generates randomly distributed pyramids [222] whose position are not correlated between the two surfaces of the layer. As for the dielectric layer, the randomization of the position of the photon is a computationally cheap way to simulate traveling for a distance that is orders of magnitude larger than the size of the unit cell;

- if the photon is in one of the two semi-infinite air layers and is traveling away from the system, it is considered either reflected (if

it is in the first air layer, that is $j = 1$) or transmitted (if it is in the last air layer, that is $j = 11$), and a new iteration is initialized.

The flow chart of the simulation algorithm is reported in Figure 2.4.

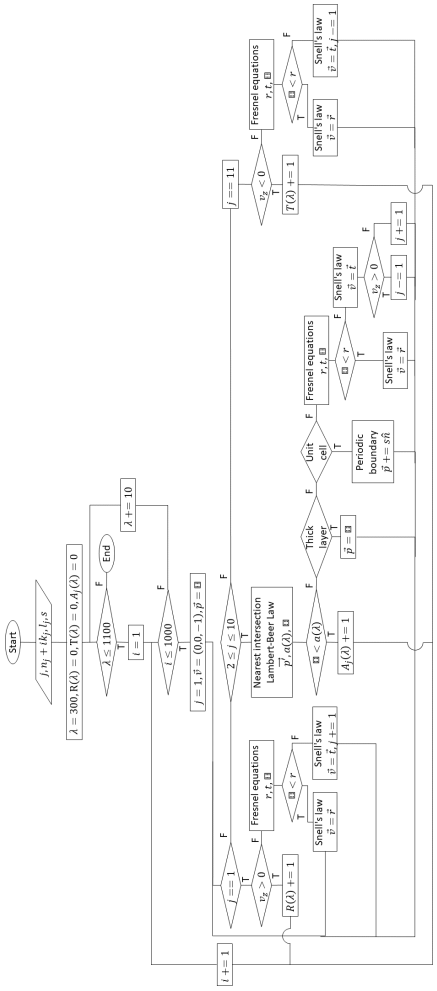

Figure 2.4: Schematic flow chart of the optics simulation algorithm. The counters $R(\lambda)$, $T(\lambda)$ and $A_j(\lambda)$ are increased when a photon is reflected, transmitted or absorbed, respectively.

The optics simulation has been validated by comparison with optical data from a textured 160 µm thick SHJ cell covered with ITO on the front and on the back (80 nm and 100 nm, respectively), manufactured by Enel Green Power. These data of have been measured with a Bentham PVE300 photovoltaic QE system and compared to the reflectivity and transmissivity calculated by the model. The results, reported in Figure 2.5, show a general agreement between the model and experimental data (Figure 2.5a), as well as the contribution of each layer in the modeled system to the total absorbance (Figure 2.5b). A deviation between the model and the experimental data was found in the near-infrared region for wavelengths longer than 1000 nm, where an underestimate of absorbance occurred. Such deviation is most likely due to scattering effects occurring when the wavelength is close to the pyramid feature size, which cannot be accurately modeled using ray tracing [223].

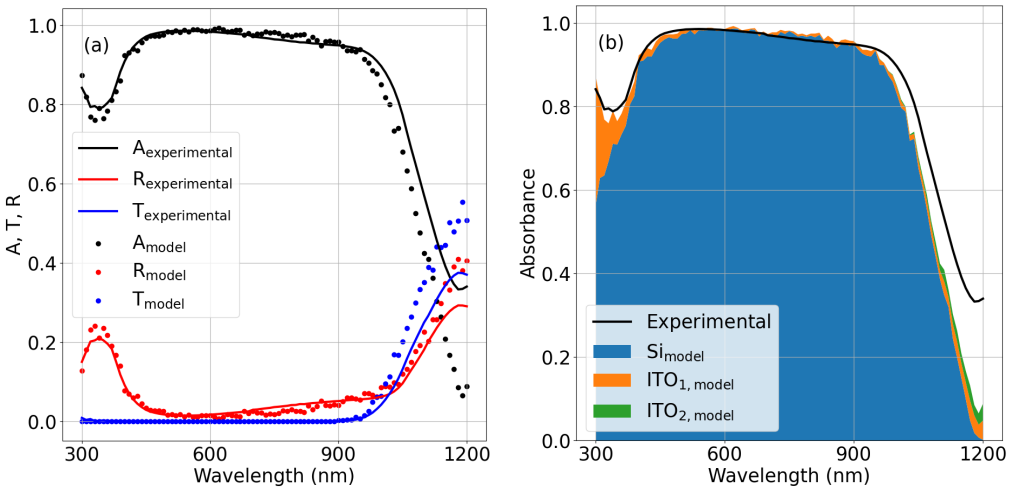

Figure 2.5: Comparison between experimental and simulated optical properties of an SHJ cell (a). Stacked area chart of the simulated absorbances of each layer in the simulated test sample (b).

To optimize the thicknesses of anti-reflection layers and of the interlayer of the multi-junction system, the case of the CdTe/Si system has

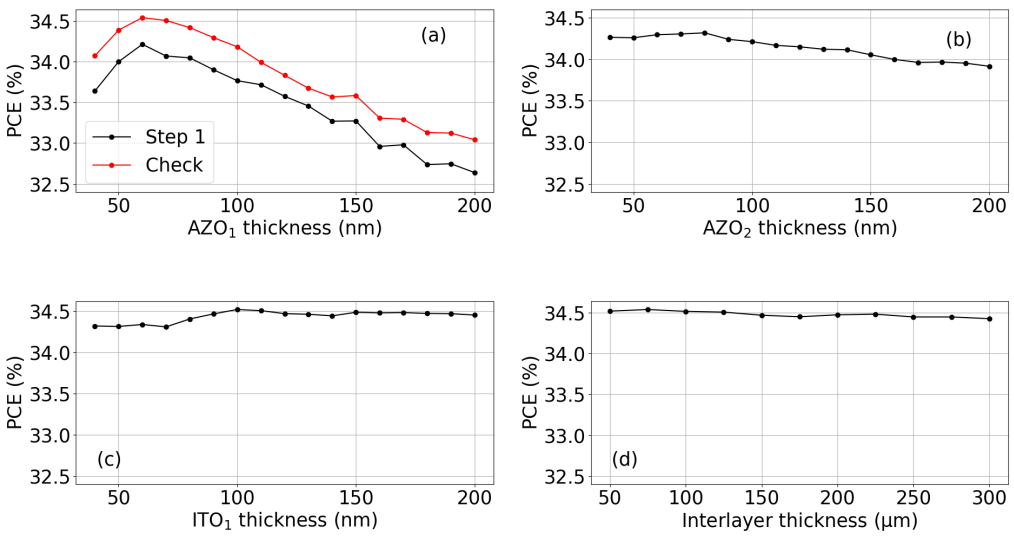

Figure 2.6: SQ PCEs obtained in the CdTe/Si system by varying the thickness of the first AZO layer (a) before and after the optimization process, of the second AZO layer (b), of the first ITO layer (c) and of the interlayer (d).

been considered, since the refractive index of CdTe is close to the average of all the considered semiconductors for the top module. Rather than simulating all the possible combinations of the four parameters, it has been preferred to optimize one layer at a time (a similar approach was employed in [224, 225]), starting from the first AZO layer and with the initial configuration $l_{AZO_2} = 100$ nm, $l_{ITO_1} = 80$ nm, $l_{interlayer} = 100$ µm and $l_{CdTe} = 2$ µm. The system is optimized by determining the PCE in SQ limit in standard test conditions (STC, corresponding to a 1000 W/m^2 irradiance and 25 °C ambient temperature). In the first step of the optimization process, the thickness of the first AZO layer was varied while the other thicknesses were fixed to the values reported above; the results shown in Figure 2.6a indicate that the optimal thickness of this layer is 60 nm, and this value was fixed for the following steps. In the next step, the thickness of the second AZO layer was varied to obtain an optimal value of 80 nm (Figure 2.6b). In the same fashion, the optimal thickness of the

top ITO layer (Figure 2.6c) was determined to be 100 nm (similar results for the ITO layer have already been reported in [226]), and the optimal interlayer thickness was 75 µm (Figure 2.6d). At the end of the process, a new optimization iteration was performed on the first AZO layer to check that the optimal value had not changed due to the optimization of the following layers (Figure 2.6a).
With the AZO_1, AZO_2, ITO_1 and interlayer thicknesses optimized as shown in Figure 2.6, the thicknesses of GaAs, CdTe and CGS have been investigated. This variable was allowed to span from 0.1 µm to 4 µm, and the results reported in Figure 2.7 show that the *PCE* obtained in the SQ limit under STC increases with the top semiconductor thickness, although the efficiency gain decreases significantly for thicknesses greater than 1 µm.

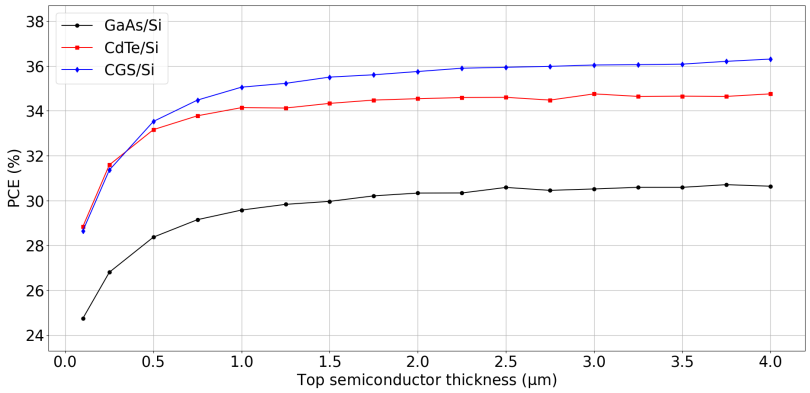

Figure 2.7: SQ-limit PCEs of the GaAs/Si, CdTe/Si and CGS/Si systems for top semiconductor thicknesses ranging from 0.1 µm to 4 µm.

As for the PVK/Si system, one important advantage of PVK is the possibility of tuning its bandgap in a wide range of energies as mentioned in Section 1.6.7 [183, 227]. It is therefore useful to evaluate the optimal PVK bandgap for the coupling with Si in a multi-junction system while also taking into account how the optical properties of PVK are related to its bandgap. In order to estimate the performance of PVK/Si modules with different PVK bandgaps, I started from considering the experimental optical constants of PVK with a bandgap of 1.94 eV reported in [213].

I then modified the imaginary part of the refractive index by stretching the function $k(\lambda)$ to obtain bandgaps ranging from 1.6 eV to 2 eV, and recalculated the real part through the Kramers–Kronig relations [228]:

$$Re(\chi(\omega)) = \frac{2}{\pi} P \int_0^\infty \frac{\omega' Im(\chi(\omega))}{\omega'^2 - \omega^2} \mathrm{d}\omega' \tag{2.30a}$$

$$Im(\chi(\omega)) = -\frac{2\omega}{\pi} P \int_0^\infty \frac{Re(\chi(\omega))}{\omega'^2 - \omega^2} \mathrm{d}\omega' \tag{2.30b}$$

where P represents the Cauchy principal part of the integral, $\omega = \frac{2\pi c}{\lambda}$ is the frequency corresponding to the wavelength of interest, c is the speed of light in vacuum and χ is the electric susceptibility of the medium, which is related to the refractive index by

$$\chi = \epsilon_r + 1 = (n + ik)^2 + 1 \tag{2.31}$$

The new refractive indices are reported in Figures 2.8a and 2.8b, along with the absorption coefficient $\alpha(\lambda)$ (Figure 2.8c).

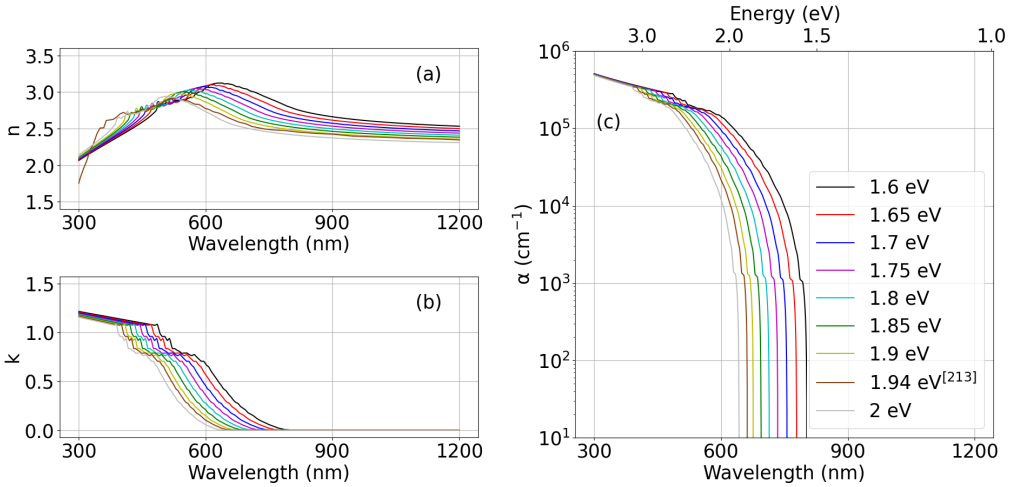

Figure 2.8: Real (a) and imaginary (b) parts of the refractive indices obtained from the Kramers–Kronig relations and absorption coefficients (c) of PVK for bandgaps ranging from 1.6 eV to 2 eV.

With the optimized thicknesses of AZO_1, AZO_2, ITO_1 and of the interlayer, I varied the PVK bandgap from 1.6 eV to 2 eV (with an initial thickness fixed to 2 µm). In Figure 2.9a, it can be observed that the optimal bandgap resulted equal to 1.85 eV, which is different from the value commonly reported in the literature of 1.7 eV [229]. However, this value is usually obtained through *ab initio* calculations, where the absorbances of the materials are assumed to be one, neglecting optical effects altogether. On the contrary, the simulations showed that an accurate evaluation of a photovoltaic system must include an optical model that considers the refractive indices of all materials involved. Moreover, it can be seen that the contribution to the system performance from the PVK module decrease as the bandgap increases, while the Si module follows the opposite trend: this is due to the fact that as the PVk bandgap increase only photons with higher and higher energies are absorbed by this module, leaving more low energy photons to be absorbed by the Si module. Figure 2.9b shows the *PCE* trend with the PVK thickness for the 1.85 eV bandgap PVK, indicating that again the *PCE* of the system increases with the PVK thickness.

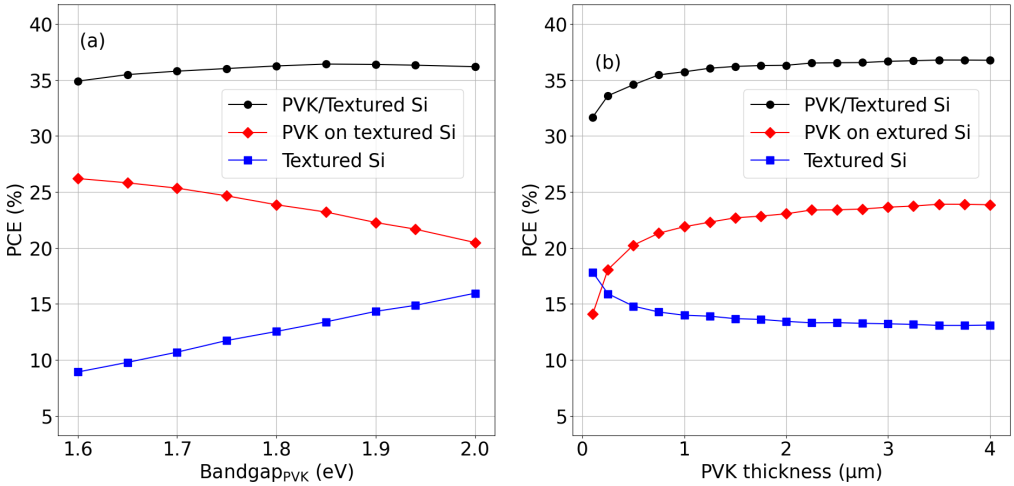

Figure 2.9: SQ *PCE* for different PVK bandgaps for the PVK/Si system at a fixed PVK thickness of 2 µm (a). SQ *PCE* of the PVK/Si system for different thicknesses of the 1.85 eV bandgap PVK (b).

Semiconductor	Bandgap[206] (eV)	Bandgap$_{\text{SA cell}}$[130] (eV)	$V_{oc,SA}$ (V)	$V_{oc,SQ}$ (V)	TDC
Si	1.12	-	0.738	0.860	0.858
GaAs	1.42	-	1.127	1.144	0.985
CdTe	1.5	-	0.875	1.215	0.720
$CuIn_{1-x}Ga_xSe_2$	1.7 ($x = 1$)	1.08	0.734	0.822	0.893
PVK	1.85	1.67	1.213	1.374	0.883

Table 2.1: Bandgap energies, open-circuit voltages and technology development coefficients (TDCs) of the semiconductors considered in [206]. For CGS and PVK, the bandgap of the record cells reported in the literature [130] are also listed. It must be noted that for these materials, TDC calculations were based on the bandgap and voltages of the literature material, while the coefficient was assumed to be the same for the bandgap considered in [206].

So far, all *PCE* values have been calculated in the ideal SQ condition. However, as mentioned previously, in order to provide a more realistic estimate of the achievable multi-junction system efficiency, I introduced a technology development coefficient, defined as the ratio between the open-circuit voltages of SA cells and the ideal SQ limit for the same semiconductor evaluated under STC. This coefficient has been introduced with the idea to take into account all the recombination processes (Auger, Shockley–Read–Hall, interfaces, photon recycling, etc.) even without an accurate electrical model. As SA values, I considered those reported in [130], while the SQ values were obtained by considering the voltage of the ideal J–V characteristics at $J = 0$ A/m^2. The TDCs for the semiconductor technologies considered in [206] are reported in Table 2.1. It must be noted that, although for CGS and perovskite the materials employed for the record cells reported in the literature have different bandgap energies compared to those considered within [206], the same TDC value has been assumed.

Once the TDC of each semiconductor has been calculated, starting from the initial SQ calculation of the J-V characteristics of each module, the dark saturation currents have been updated according to Equation (2.13) to obtain the SA adjusted curves and the J-V characteristics of the whole

system is obtained by adding the two contributions. In Table 2.2 are reported the PCEs of the four systems both in the SQ limit and in the SA case. The number of cells in the top module was modified to take into account the lower voltage output of the state-of-the-art cells compared to their theoretical limit, whereas the number of Si cells in the bottom module was fixed at 72. Considering that the two modules should have similar voltage outputs and that therefore $n_{c,top}V_{oc,top} \simeq n_{c,Si}V_{oc,Si}$, it is to be expected that the ratio between the number of cells connected in series in the two modules is roughly equal to the inverse of the ratio of the respective open-circuit voltages, as it can be observed from Table 2.2.

System	$n_{c,top,SQ}$	$n_{c,top,SA}$	PCE_{SQ} (%)	PCE_{SA} (%)
GaAs/Si	50	44	30.51	29.45
CdTe/Si	48	57	34.53	25.24
CGS/Si	42	40	36.07	31.74
PVK/Si	38	37	36.77	34.16

Table 2.2: Comparison between number of top semiconductor cells and PCEs obtained in the SQ limit and for state-of-the-art cells in the multi-junction systems.

The *PCE* drop was more noticeable in the CdTe/Si system as CdTe has the lowest TDC, whereas the drop was much lower in the GaAs/Si module as GaAs has the highest TDC. Among all the considered semiconductors for the top module, the PVK module with the 1.85 eV bandgap is the one that allows, in principle, the best multi-junction system efficiency, which would reach about 34% with current state-of-the-art cells.

Chapter 3

Module installation

Once a certain PV technology has been perfected at the cell and module level, another crucial step is the installation of the modules in outdoor applications. This represents a drastic change in operating conditions for the modules, as they are subjected to several external agents (humidity, heat, sand, hail, soiling, etc.) that may degrade their performance, not only during the module operation lifetime but also during long lasting experiments carried out in outdoor sites. For this reason, several test protocols have been defined to certificate the quality and robustness of the modules and even to study why and how modules age in outdoor conditions, and this is a very active sector of the PV research as these protocols must be updated as new technologies and module designs enter the market.

In order to extract the highest power possible from modules in the field, the configuration of the system must take into account certain key factors, namely the amount of light that will be available during the year, the temperatures that the modules may reach and how much the module could degrade in that specific locations. For small residential applications there is not much freedom in how much these parameters can be optimized, as modules are often installed on rooftops, and therefore the orientation and surroundings of the module can be considered fixed. For large utility scale applications, however, these parameters become crucial when choosing the site for the plant, and accurately modeling how the system will perform in outdoor operating conditions is necessary to optimize the

power production of the plant.

3.1 Irradiance model overview

Over the years, several different models have been designed to predict daily solar radiation [230]. One is generally interested in predicting the amount of light impinging on horizontal surfaces or surfaces tilted by an angle β.
The intensity on a horizontal surface I_H can be expressed as the sum of two terms, the direct beam component I_b and the diffuse light component I_d:

$$I_H = I_b \cos(\theta_z) + I_d \tag{3.1}$$

where θ_z is the solar zenith angle, defined as the angle between the direction of the direct beam and the normal to the ground. Sometimes the complementary angle α, called elevation or altitude angle, is used to describe the position of the Sun with respect to a horizontal surface. The other important angles needed to describe the position of the Sun are the declination angle δ, which is the angular distance of the Sun from the celestial equator, the hour angle ω, defined as the angular distance between the meridian of the observer and the meridian passing through the Sun (whereas the azimuth angle θ_{az} is defined as the horizontal position of the Sun measured clockwise from the North), and the latitude ϕ of the location of interest. It has to be noted that due to the tilt of the rotation axis of the Earth with respect to its orbit of 23.45°, the Sun oscillates yearly between $\delta = -23.45^\circ$ and $\delta = 23.45^\circ$, and the hour angle is defined so that it is 0° at noon:

$$\omega = 15^\circ \, (12 - ST) \tag{3.2}$$

where ST is the solar time defined as:

$$ST = LT + \frac{ET}{60} + \frac{4}{60} \, (L_s - L_l) \tag{3.3}$$

where LT is the local time, L_s and L_l are the latitudes of the standard meridian of the local timezone and of the location itself, respectively, and ET is the so-called equation of time [231]:

$$ET = 9.87 \sin(2B_{ET}) - 7.53 \cos(B_{ET}) + 1.5 \sin(B_{ET}) \tag{3.4}$$

	A	B	C
January	1230	0.142	0.058
February	1215	0.144	0.060
March	1186	0.156	0.071
April	1136	0.180	0.097
May	1104	0.196	0.121
June	1088	0.205	0.134
July	1085	0.207	0.136
August	1107	0.201	0.122
September	1152	0.177	0.092
October	1193	0.160	0.073
November	1221	0.149	0.063
December	1234	0.142	0.057

Table 3.1: Estimate of the parameters A, B and C from the ASHRAE model.

with $B_{ET} = \frac{360}{365}(d - 81)$ for a day d of the year; the equation of time is an empirical factor which takes into account the eccentricity of the orbit and the axial tilt of Earth. The angles that have been presented are related by the following expression:

$$\cos(\theta_z) = \sin(\alpha) = \sin(\delta)\sin(\phi) + \cos(\delta)\cos(\phi)\cos(\omega). \tag{3.5}$$

A first class of models summarize environmental factors such as humidity, air turbidity and cloud cover in a set of monthly parameters, so that the terms of Equation (3.1) can be expressed by the following expressions:

$$I_b = Ae^{\frac{-B}{\cos(\theta_z)}} \tag{3.6a}$$

$$I_d = CI_b \tag{3.6b}$$

One of the first and most popular estimate for these parameters was given by the ASHRAE model [232], reported in Table 3.1. The values of these parameters have been thoroughly investigated over the years by adapting them to real data collected in different parts of the world [233], from India [234] to China [235], Middle East [236, 237] and Africa [238], with many works focused on comparisons between many different locations [239].

Another set of models correlates the diffuse radiation I_d and the total radiation I_H on a horizontal surface based on a clearness index M_t, defined as the ratio between the global horizontal radiation and the extraterrestrial irradiation I_0:

$$M_t = \frac{I_H}{I_0}. \tag{3.7}$$

In these models, I_d is expressed as a piecewise function of I_H, where each piece is usually a polynomial of degree n of I_H and its range of applicability depends on the value of M_t. As an example, I report a model by Liu and Jordan [240], based on data collected in Canada and USA, which adopts a first degree polynomial for $0.75 < M_t \leq 1$:

$$I_d = (0.384 - 0.416 M_t)\, I_H \tag{3.8}$$

Another model by Erbs et al. [241], based on data from USA and Australia, employs a more complex function:

$$I_d = \begin{cases} (1 - 0.09 M_t)\, I_H & 0 < M_t \leq 0.22 \\ (0.9511 - 0.1604 M_t + 4.388 M_t^2 - 16.638 M_t^3 + 12.336 M_t^4) I_H & 0.22 < M_t \leq 0.8 \\ 0.165 I_H & 0.8 < M_t \leq 1 \end{cases} \tag{3.9}$$

Several other models have been published, with data collected from Canada [242], Mediterranean countries [243, 244, 245, 246], Brazil [247, 248], Australia [249, 250], Hong Kong [251] and India [252].
When the surface is tilted by an angle β, the angle of incidence (θ or AOI) can be calculated as [253]:

$$\theta = \text{acos}(\sin(\theta_z)\cos(\theta_{az})\sin(\beta) + \cos(\theta_z)\cos(\beta)) \tag{3.10}$$

In this case, the total irradiance I_β can be expressed as

$$I_\beta = I_{b\beta} + I_{d\beta} + I_r \tag{3.11}$$

where, compared to Equation (3.1), the direct and diffuse component must take into account the tilt of the surface and the new term I_r describes the contribution from the light reflected by the surrounding ground. In general, diffused radiation models can be divided in two groups: isotropic

models, where the intensity of the diffused radiation is assumed to be uniform, and anisotropic models, in which the sky is discretized in different regions.
One of the first and simplest isotropic models is the one by Liu and Jordan [254], in which the portion of sky contributing to the diffused radiation is equal to the fraction of solid angle of the spherical lune up to $\theta = \beta$:

$$I_{d\beta} = \frac{1}{4\pi} \int_0^{\beta} \int_0^{2\pi} \sin(\theta) \mathrm{d}\theta \mathrm{d}\phi \cdot I_d = \left(\frac{1 - \cos(\beta)}{2} \right) I_d \tag{3.12}$$

with other equations proposed in the following years [255, 256, 257].
As for the anisotropic models, one of the most famous and widely used is the Perez model [258], in which the sky is divided in three sections: the circumsolar section, the isotropic background and the horizon zone.

$$I_{d\beta} = I_d \left[\left(\frac{1 + \cos(\beta)}{2} \right) (1 - F_1) + \frac{a_1}{a_2} F_1 + F_2 \sin(\beta) \right] \tag{3.13}$$

where $a_1 = \max[0, \cos(\theta)]$, $a_2 = \max[\cos(85^\circ), \cos(\theta_z)]$ and F_1 and F_2 are empirical functions determining the weight of the circumsolar and horizon regions:

$$F_1 = \max \left(0, f_{11} + f_{12}\Delta + \frac{\pi}{180} \theta_z f_{13} \right) \tag{3.14a}$$

$$F_2 = f_{21} + f_{22}\Delta + \frac{\pi}{180} \theta_z f_{23} \tag{3.14b}$$

The isotropic configuration is recovered for $F_1 = F_2 = 1$. The f coefficients are parameters whose values depend on the value assumed by the function ϵ, which describes sky clearness, within one of eight bins ranging from overcast to clear sky:

$$\epsilon = \frac{\frac{I_d + I_b}{I_d} + 1.041 rad \cdot \theta_z^3}{1 + 1.041 rad \cdot \theta_z^3} \tag{3.15}$$

The bins of ϵ are reported in Table 3.2, whereas for the values of the f coefficients Perez himself a published different values fitted to various data sets [258, 259, 260]. Lastly, the coefficient Δ depends on the ratio between the diffuse radiation on a horizontal surface and the extraterrestrial irradiation:

$$\Delta = AM \frac{I_d}{I_0} \tag{3.16}$$

Bin	Lower bound	Upper bound
1 (overcast)	1	1.065
2	1.065	1.230
3	1.230	1.500
4	1.500	1.950
5	1.950	2.800
6	2.800	4.500
7	4.500	6.200
8 (clear sky)	6.200	∞

Table 3.2: Sky clearness ϵ bins.

where the Air Mass AM is another important parameter indicating the relative height of the air column traversed by light, which depends on θ_z. The minimum height, which corresponds to $\theta_z = 0$ and $AM = 1$ (usually referred to as $AM1$), is the thickness of the atmosphere; analogously, $AM0$ corresponds to the extraterrestrial spectrum whose irradiance value is I_0, while $AM1.5$ (roughly corresponding to $\theta_z = 48°$) is another notable spectrum as it is the one adopted as reference when comparing the efficiency of solar cells. Several approximation have been proposed to calculate AM: a first order approximation ignores the curvature of the Earth, and in this case

$$AM = \frac{1}{\cos(\theta_z)}; \tag{3.17}$$

however, this model will predict infinite Air Mass as θ_z approaches $\frac{\pi}{2}$. A more accurate definition can be derived by considering Earth as a perfect sphere, in which case, being r the ratio between Earth's radius and the atmosphere height [261]:

$$AM = \sqrt{(r\cos(\theta_z))^2 + 2r + 1} - r\cos(\theta_z). \tag{3.18}$$

Other models have been proposed throughout the year, taking into consideration density variability through the atmosphere, temperature differences and refraction [262]. It is intuitive that light intensity reduces with increasing Air Mass, but due to the different and variable atmospheric factors involved such as humidity, pollution, air temperature, etc., which

must be considered not only locally but even in the tens of kilometers travelled by light, the dependency of light intensity from AM can be quite complicated. For this reason, this relation is often expressed through an empirical approximation model [263]:

$$I_{AM} = 1.1 \cdot I_0 \cdot 0.7^{\left(AM^{0.678}\right)} \tag{3.19}$$

Where the factor 1.1 assumes that diffuse light amounts to 10% of direct light and the factor 0.7 assumes that 30% of incoming light is reflected by the atmosphere.

3.2 Module temperature model overview

As discussed in Section 1.4, temperature has a major effect on the operation of a solar cell, as it reduces the bandgap decreasing the voltage output of the cell; at the same time, the smaller bandgap means the cell can now absorb photons with less energy, which increases the current, although this secondary effect is marginal compared to the voltage drop. Usually, experimental studies and characterization of new cells are carried out under STC, which means at 25 °C. However, in outdoor installations, several factors, such as ambient temperature, wind speed and irradiance, can greatly affect the operating temperature of the modules. Besides, knowing the module temperature is necessary for estimating the thermal stress on the materials and thus for quantifying the degradation of the modules [264], which is essential for predicting the lifetime of the modules. Therefore, accurately predicting the operating temperature is an important step to evaluate the performance and profitability of the system. However, in general the temperature cannot be directly measured at the cell level, as the cells are inside the panels and therefore covered by an encapsulating material (commonly ethylene-vinyl-acetate, EVA [265]), with a layer of tempered glass on the front surface and another layer of glass for bifacial cells or with a plastic backsheet on the back surface [266]. In order to measure the cell temperature directly, one would have to either integrate temperature sensors inside the module during the manufacturing process [267, 268] or to install them afterwards

by manipulating the modules [269]. Hence, the quantities that are usually directly accessible are the temperatures of the outer surfaces of the module. For this reasons, module temperature is mostly estimated from a number of environmental and internal parameters, and several models have been proposed to address this task [270, 271].
One of the first models was the one published by Ross in 1980 [272], which introduces a Nominal Operating Cell Temperature (*NOCT*): this temperature is measured in different conditions than those of STC, namely 800 W/m^2 irradiance, 20 °C air temperature and 1 m/s wind speed. In this model the cell temperature T_c is defined as

$$T_c = T_a + \frac{NOCT - 20\ ^\circ C}{800\ W/m^2} I_\beta \tag{3.20}$$

with T_a being the ambient temperature. Typical *NOCT* values are about 45 °C for most commercial modules [273] and are provided by the manufacturer.
Heat transfer has been implemented in a model by Faiman [274]:

$$T_c = T_a + \frac{I_\beta}{U_0 + U_1 WS} \tag{3.21}$$

where U_0 is the constant heat transfer coefficient ($W \cdot m^{-2} \cdot K^{-1}$), U_1 the convective heat transfer coefficient ($W \cdot s \cdot m^{-3} \cdot K^{-1}$) and WS the wind speed. A more complex function is used in PVsyst, a commercial simulation tool by Sandia National Laboratories [275]:

$$T_c = T_a + I_\beta \frac{\alpha\,(1-\eta)}{U_0 + U_1 WS} \tag{3.22}$$

where α is the module absorption coefficient and η its efficiency. Though it considers additional factors such as optical and heat transfer characteristics of the module and wind speed, this model requires several additional parameters that the user must know or measure in order to utilize the model properly. A simpler approximation of this model has been implemented in another simulation tool, PVLab [276]:

$$T_c = T_a + I_\beta \frac{\alpha\,(1-\eta)}{H} \tag{3.23}$$

where H represents a global heat transfer coefficient. This model neglects wind effects, and in contrast uses a default value $H = 29\ \mathrm{W \cdot s \cdot m^{-3} \cdot K^{-1}}$. Other models, such as [277] (also by Sandia), start by estimating the temperature of the module backside T_b, introducing empirically-determined coefficient to account for the fact that anemometers are usually installed at a height of about 10 m, much higher than the modules:

$$T_b = I_\beta \left(e^{a+bWS} \right) + T_a \tag{3.24}$$

where a is related to the upper temperature reached in conditions with high irradiance and low wind and b determines how effective wind is in cooling the module down. But, given that the superficial temperature of the module and of the cell may differ as discussed previously, a second equation relates these two quantities:

$$T_c = T_b + \frac{I_\beta}{I_{AM1.5}} \Delta T \tag{3.25}$$

where $I_{AM1.5}$ is the intensity of the standard solar spectrum (1000 $\mathrm{W/m^2}$) and ΔT is the temperature difference between cell and module measured in STC, usually of about 2-3 °C [277].

3.3 2D and 3D PV system modeling

In regards with the modeling of entire PV systems in the field, any simulation tool must include an irradiance model and a temperature like those introduced in the previous Sections 3.1 and 3.2 (with many more available in the literature); however, and especially for the irradiance model, the most crucial choice is between 2D and 3D simulation. The former favors simple geometrical considerations, whereas the latter usually introduces a discretization of the system and its surroundings along with a function that determines how each element contributes to the overall irradiance.

In the case of bifacial modules, estimating the albedo irradiance $I_{r\beta}$ impinging on the module backside is critical for evaluating the performance of the system: the first configuration that can be considered assumes that

the intensity of reflected radiation is isotropic [278], and in this case it can be calculated from the remaining lune with respect to what has been discussed for Equation (3.12):

$$I_{r\beta} = I^*_{d\beta}\rho = \frac{1}{4\pi}\int_{\beta}^{\pi}\int_{0}^{2\pi}\sin(\theta)\mathrm{d}\theta\mathrm{d}\phi\cdot\rho I_H = \left(\frac{1+\cos(\beta)}{2}\right)\rho I_H \quad (3.26)$$

where $I^*_{d\beta}$ is the fraction of diffuse irradiance associated with the solid angle of the spherical lune behind the module and ρ is the ground albedo.
Other models include several view factors to account for module self-shading and for light reflect by the ground in front of the module [279, 280, 281], while others also consider how rows in the system can shade each other [282].
In three-dimensional models, the most common approach is actually borrowed from heat transfer theory [283]:

$$VF_{A1\to A2} = \frac{1}{A_1}\int_{A_1}\int_{A_2}\frac{\cos(\theta_1)\cos(\theta_2)}{\pi R^2}\,\mathrm{d}A_1\,\mathrm{d}A_2 \quad (3.27)$$

where $VF_{A1\to A2}$ is the view factor from the ground element A_1 to the module A_2, R the distance between the two and $\theta_{1,2}$ the angles between R and the normal vector to the respective surface [284, 285].

3.3.1 Description of a 3D model

All the models cited so far only consider the total irradiance, disregarding how this irradiance is distributed in terms of spectrum, which is actually important to evaluate accurately how much module can heat up; this is especially significant when comparing monofacial and bifacial modules, as the backsheet in the former is designed to reflect visible light trying to escape the module back into it while being transparent to infrared light below the bandgap of silicon ([286]), whereas the latter lack this layer but receive additional light on the back, whose spectral distribution depends on the ground beneath the module [287].
In [288] a new MATLAB-based 3D simulation code has been presented, further described and detailed in [289], which has been specifically aimed at the simulation of bifacial systems: in this model the position of the Sun

is first calculated at each moment in time from Equations (3.2) and (3.5), obtaining the angle of incidence from Equation (3.10). Then, the Air Mass at the current Sun position is calculated from Equation (3.17); whereas most models apply the AM value to determine the irradiance such as in Equation (3.19), particular emphasis is put in this model on the spectral distribution of solar light, therefore AM is used to adjust the solar spectrum as:

$$AM_x(\lambda) = AM0(\lambda) - \frac{x}{1.5}\left(AM0(\lambda) - AM1.5(\lambda)\right) \tag{3.28}$$

where $AM_x(\lambda)$ is the solar spectrum at $AM = x$. This equation performs a wavelength-per-wavelength linear interpolation between the two spectra $AM0(\lambda)$ and $AM1.5(\lambda)$. Then, the AM_x spectrum is re-scaled to the irradiances I_b and I_d defined by the ASHRAE model using Equation (3.6) with the coefficients reported in Table 3.1. Lastly, diffuse light is assumed to be isotropically diffused as in the model by Liu and Jordan of Equation (3.12). With this procedure, each component of solar light has both an irradiance value and a corresponding spectral distribution.
As for the reflected light, the ground surface is divided in finite elements $\mathrm{d}A_s$, with $P = (P_x, P_y, 0)$ the center of each element; for each element, the view factor $\Omega(x, y)$ must be calculated first to determine how much it contributes to the albedo light impinging on the back of the module. Being L_x the length of the module in the x-axis (oriented along the North-South direction), L_y its length in the y-axis (oriented along the East-West direction) and $C = (x_m, y_m, z_m)$ its center, its vertices v_m have the following coordinates:

$$v_{m1} = \left(x_m + \frac{L_x}{2}\cos\beta, y_m - \frac{L_y}{2}, z_m - \frac{L_x}{2}\sin\beta\right) \tag{3.29a}$$

$$v_{m2} = \left(x_m + \frac{L_x}{2}\cos\beta, y_m + \frac{L_y}{2}, z_m - \frac{L_x}{2}\sin\beta\right) \tag{3.29b}$$

$$v_{m3} = \left(x_m - \frac{L_x}{2}\cos\beta, y_m + \frac{L_y}{2}, z_m + \frac{L_x}{2}\sin\beta\right) \tag{3.29c}$$

$$v_{m4} = \left(x_m - \frac{L_x}{2}\cos\beta, y_m - \frac{L_y}{2}, z_m + \frac{L_x}{2}\sin\beta\right) \tag{3.29d}$$

Considering one of the diagonals of the module surface, for example $v_{m1}v_{m3}$, it is possible to define two tetrahedrons with P as their vertex

and the triangles $v_{m1}v_{m2}v_{m3}$ and $v_{m1}v_{m3}v_{m4}$ as their bases. Starting from the first tetrahedron and by introducing the vectors $\vec{R}_i$ from the vertex of the pyramid (which is the center of the ground element) to the i-th vertex of the module, one can define the vertex angles from the scalar product of each couple of vectors:

$$\theta_{12} = \operatorname{acos}\left(\frac{\vec{R}_1 \cdot \vec{R}_2}{\left\|\vec{R}_1\right\|\left\|\vec{R}_2\right\|}\right) \tag{3.30a}$$

$$\theta_{23} = \operatorname{acos}\left(\frac{\vec{R}_2 \cdot \vec{R}_3}{\left\|\vec{R}_2\right\|\left\|\vec{R}_3\right\|}\right) \tag{3.30b}$$

$$\theta_{31} = \operatorname{acos}\left(\frac{\vec{R}_3 \cdot \vec{R}_1}{\left\|\vec{R}_3\right\|\left\|\vec{R}_1\right\|}\right) \tag{3.30c}$$

Then, by making use of L'Huilier's theorem [290], the solid angle of the first tetrahedron is obtained as:

$$\Omega_1 = 4\operatorname{atan}\left(\sqrt{\tan\left(\frac{\theta_s}{2}\right)\tan\left(\frac{\theta_s-\theta_{12}}{2}\right)\tan\left(\frac{\theta_s-\theta_{23}}{2}\right)\tan\left(\frac{\theta_s-\theta_{31}}{2}\right)}\right) \tag{3.31}$$

with $\theta_s = \frac{\theta_{12}+\theta_{23}+\theta_{32}}{2}$. Repeating these steps for the second tetrahedron yields the total view factor for the ground element (Figure 3.1).

The model also takes into account module self-shading by introducing a boolean function $ssh(x, y)$ whose value is 1 for unshaded elements and 0 for shaded elements. Whether a ground element is shaded or not is determined by projecting parallel sunbeams from the vertices of the module towards the ground. The aforementioned azimuth and zenith angles identify the position of the Sun and the direction of its rays in a spherical coordinate system, therefore these can be expressed by the vector

$$\vec{s} = (\sin(\theta_z)\cos(\theta_{az}), \sin(\theta_z)\sin(\theta_{az}), \cos(\theta_z))\,. \tag{3.32}$$

Then, an increment $d_{1-2,3-4} = -\frac{v_{m1-2,3-4_z}}{s_z}$ is defined according to the height of the lower and upper vertices of the module; the shadowed area

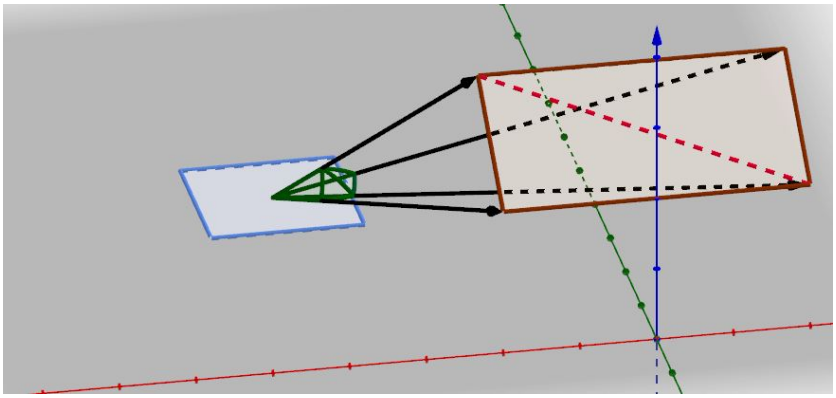

Figure 3.1: Schematic diagram of the geometry used to calculate the view factor from the angles(green) from the ground element (blue) to the module (red). The red dashed line separates the two tetrahedrons.

is obtained by moving the projection of the module on the ground by said increment along the x- and y- axis, obtaining the vertices v_s

$$v_{s1} = \left(v_{m1_x} + d_1 \cdot s_x, v_{m1_y} + d_1 \cdot s_y, 0\right) \tag{3.33a}$$

$$v_{s2} = \left(v_{m2_x} + d_2 \cdot s_x, v_{m2_y} + d_2 \cdot s_y, 0\right) \tag{3.33b}$$

$$v_{s3} = \left(v_{m3_x} + d_3 \cdot s_x, v_{m3_y} + d_3 \cdot s_y, 0\right) \tag{3.33c}$$

$$v_{s4} = \left(v_{m4_x} + d_4 \cdot s_x, v_{m4_y} + d_4 \cdot s_y, 0\right) \tag{3.33d}$$

These vertices draw a parallelogram on the ground, therefore it must be checked that the center P of the ground element $\mathrm{d}A_s$ lies inside the parallelogram through the following conditions:

$$\begin{cases} v_{s4_x} \leq P_x \leq v_{s1_x} \\ v_{s1_y} + \frac{v_{s4_y} - v_{s1_y}}{v_{s4_x} - v_{s1_x}} \left(P_x - v_{s1_x}\right) \leq P_y \leq v_{s2_y} + \frac{v_{s3_y} - v_{s2_y}}{v_{s3_x} - v_{s2_x}} \left(P_x - v_{s2_x}\right) \end{cases} \tag{3.34}$$

and $ssh(x, y)$ will be 0 if these conditions are fulfilled and 1 otherwise. Moreover, it is determined if the ground element is facing the front or the back of the module by calculating the angle of incidence of the reflected

light on the module:

$$\theta = \text{acos}\left(\frac{\vec{R_c}\cdot\hat{n}}{\left\|\vec{R_c}\right\|}\right) \tag{3.35}$$

where $\vec{R_c}$ is the vector from the center of the ground element P to the center of the module C and $\hat{n} = (\sin(\beta), 0, \cos(\beta))$ is the normal unit vector to the module; if $\theta < \frac{\pi}{2}$ light reflected by the ground element will impinge on the module back, otherwise it will be collected by the front of the module.
Lastly, the total reflected spectrum on the back is calculated as the sum of the contributions from all the non-shadowed elements:

$$I_{r\beta}(\lambda) = \sum_{x,y,ssh=1,\theta<\frac{\pi}{2}} \frac{\Omega(x,y)}{2\pi}\,\mathrm{d}A_s\,\rho(\lambda)I_H(\lambda). \tag{3.36}$$

An analogous sum on the elements for which $\theta > \frac{\pi}{2}$ yields the reflected light collected by the front of the module $I^*_{r\beta}(\lambda)$. Lastly, it must also be considered the fraction of diffused light $I^*_{d\beta}(\lambda)$ impinging on the back of the model, which is given by the same integral used to determine the irradiance impinging on the ground in Equation (3.26).
Once all the components of the overall irradiance have been calculated, the I_{sc} of each module in the array can be calculated as:

$$\begin{aligned} I_{sc} &= I_{sc,front} + I_{sc,back} = \\ &= hcqL_xL_y\left[\int_\lambda \frac{1}{\lambda}EQE_f(\lambda)\left(I_b(\lambda)\cos(\theta) + I_{d\beta}(\lambda) + I^*_{r\beta}(\lambda)\right)\mathrm{d}\lambda + \right. \\ &\quad \left. + \int_\lambda \frac{1}{\lambda}EQE_b(\lambda)\left(I_{r\beta}(\lambda) + I^*_{d\beta}(\lambda)\right)\mathrm{d}\lambda\right] \end{aligned} \tag{3.37}$$

where the factor $\frac{hcq}{\lambda}$ converts the spectra from $\mathrm{W/m^2}$ to photon flux.
The temperature model implemented in this code is the NOCT model by Ross of Equation (3.20) [272]; in[291], I have introduced a modification of the temperature module by adding the additional albedo light collected by the back of bifacial modules, whereas the original model had been

developed for monofacial modules:

$$T_{m,bifacial} = T_a + \frac{NOCT - 20\ ^\circ C}{800\ W/m^2} I_\beta. \tag{3.38}$$

where I_β is the sum of all the components illustrated above.
Finally, the I-V characteristics of each module is calculated as in Equation (1.13) and the characteristics of the entire system is obtained by adding each module in series.

3.3.2 Simulation results and outdoor experiments

In [288] the model has been validated by comparison with a laboratory scale system made up by four bifacial cells in series arranged in a 2-by-2 minimodule, tested in Catania (latitude 37°24′41″N). The model has been validated against experimental data at different ground clearances ranging from 25 cm to 55 cm and at different tilt angles from 20° to 46°: both the experimental data and the model confirmed that the optimal installation for this system at this latitude is with a ground clearance of 55 cm and a tilt angle of 35°.
In [289], the model was used to evaluate the performance of a bigger system: in this case a 2-by-15 array of full-size modules, both with bifacial and monofacial cells. The study estimated the performance gain by employing a monoaxial solar tracker at different latitudes, concluding that the monoaxial tracker is more beneficial at low latitudes, increasing the energy output of the bifacial array by 11% and that of the monofacial array by 14% at the latitude of Catania. Moreover, the module has been employed to approximate a 2D simulation by extending the system along the y-axis and focusing on the central modules: in this scenario, it resulted that 2D models tend to underestimate the energy output per module, as they neglect the additional light received by edge modules in the array, as these modules have a wider ground area available for collecting reflected light.
In [291], I have been involved in a study aimed at a direct comparison between monofacial and bifacial systems implementing the same technology: in particular, two identical minimodules of 3 bifacial n-type SHJ cells have been prepared. The minimodules had not been fabricated through

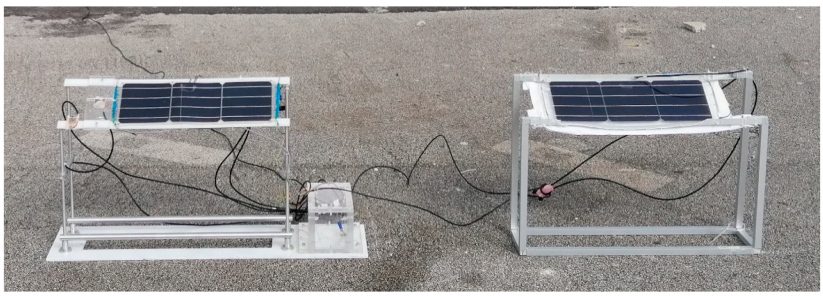

Figure 3.2: Experimental setup for the study reported in [291].

a standard industrial process, and lacked the outer glass layers on the front and back sides, therefore exposing the EVA encapsulant. Additionally, one of the modules has been covered with white cardboard on the back to completely prevent the albedo light collection in order to mimic a monofacial module with a white backsheet. The minimodules have been installed at a ground clearance of 55 cm and a tilt angle of 35°, in accordance with the results reported in [288], in the same test site of the previous study (Figure 3.2). Experimental electrical data, namely the I-V characteristics of the two minimodules, and irradiance data have been collected from 9 A.M. to 4 P.M. for 3 days in February 2021, on sunny days with no clouds. Additionally, two thermoresistances have been placed on the front and back side of each minimodule in order to evaluate temperature differences between bifacial and monofacial systems. In this work, due to the symmetric structure of the SHJ cell and therefore of the minimodules, the cell temperature has been assumed to be the average of the front and back temperature:

$$T_c = \frac{T_{m,front} + T_{m,back}}{2} \tag{3.39}$$

As one would expect, minimodule temperatures in Figure 3.3 are lower in the morning, reach their maximum at midday, and decrease in the afternoon, and they are significantly higher than the ambient temperature due to the thermalization of the absorbed photons. In particular, it can be seen that the bifacial minimodule is up to about 12 °C warmer than the monofacial minimodule. Moreover, the experimental assumption of Equation (3.39) and the modified *NOCT* model of Equation (3.38) follow

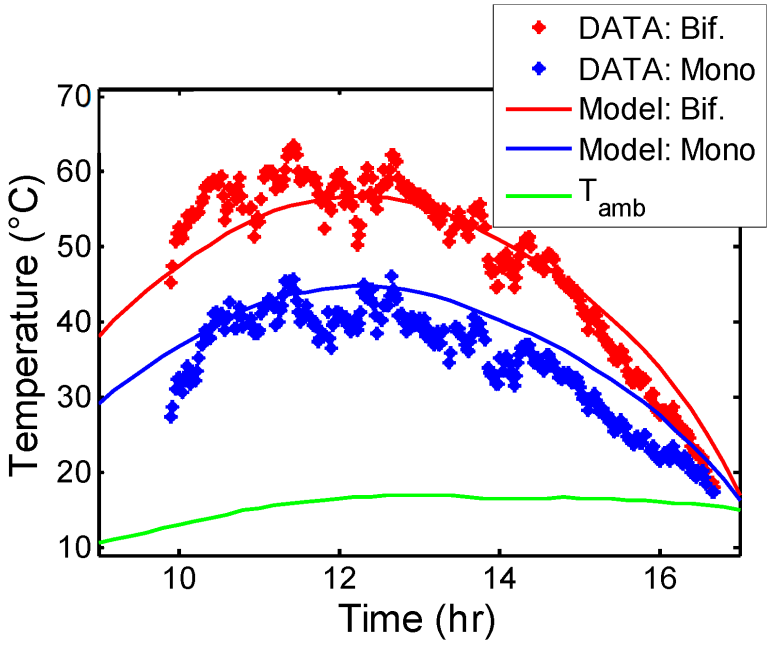

Figure 3.3: Temperature data for the monofacial and bifacial minimodules compared with the model. Ambient temperature is also reported as reference.

the same trend.
The I_{sc} data, reported in Figure 3.4a, show that the current difference between the minimodule of about 1.5 A is in accordance with the predicted contribution from the back of the bifacial minimodule, further validating the model.
As for the V_{oc} data of Figure 3.4b, the voltage outputs of the two minimodules are quite close for most of the day; in fact, the higher temperature of the bifacial minimodule should decrease its voltage output, as discussed in Section 1.4, but the additional light collected on the back compensates the negative effect of the temperature.
The fact that bifacial minimodule exhibited a similar voltage poutput but a higher current than the monofacial module imply that the daily energy yield EY is also in favor of the former, as shown in Figure 3.4c over the course of a day.

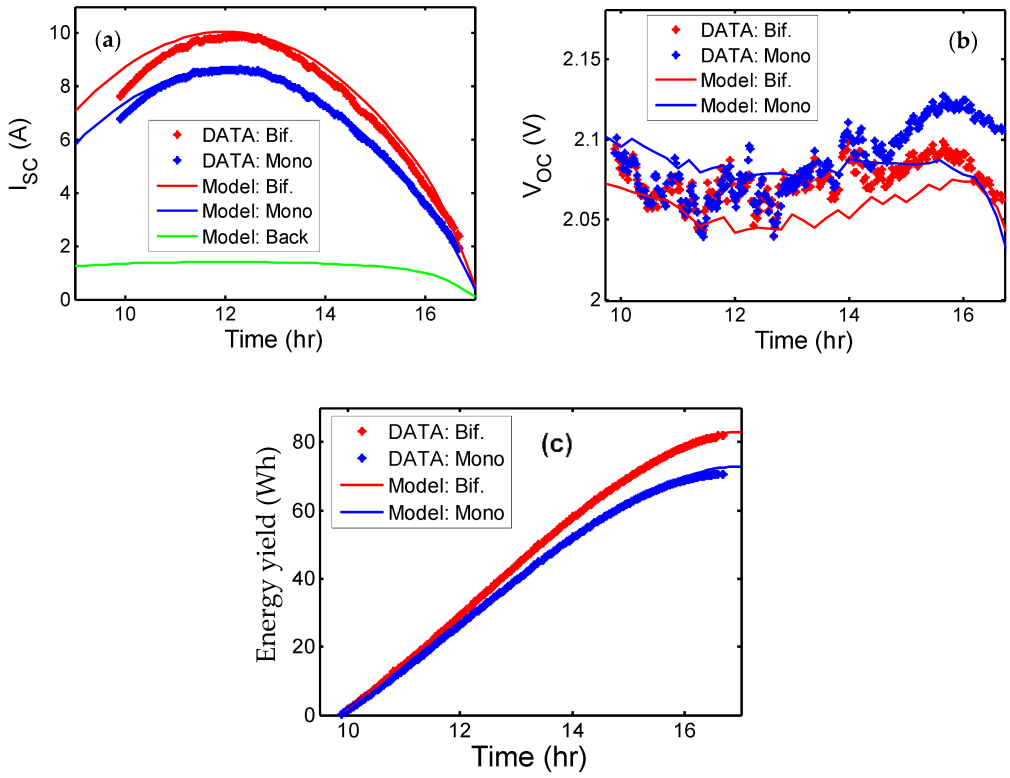

Figure 3.4: I_{sc} data for the monofacial and bifacial minimodules compared with the model, for which are reported the monofacial current and the bifacial current with the contribution collected by the back of the minimodule (a). Open-circuit voltage data for the monofacial and bifacial minimodules compared with the model (b). Data of a single day of module energy yield compared with the values predicted by the model (c).

In this work the model has also been used to investigate scenarios closer to utility scale applications: in particular, the three-cell minimodule has been compared with a 2-by-3 array of full-size modules. For both systems the energy yield EY has been calculated throughout a year at the latitude of Catania, with a tilt angle of 35° and a ground clearance of 55 cm for the minimodule and of 2 m for the array. Then, the relative Bifacial

Gain BG has been calculated as:

$$BG = \frac{EY_{bifacial} - EY_{monofacial}}{EY_{monofacial}}. \tag{3.40}$$

Figure 3.5 shows that smallest system gains the most from the bifacial cells: this is due to the fact that as the size of the system increases, the differences of illumination on the back surface among the cells increase as well. Since all cells are in series, the overall module current is determined by the lowest cell current, which are usually at the center of the array as discussed in [289]. Nevertheless, the relative bifacial gain is still between 12% and 25% throughout the year.

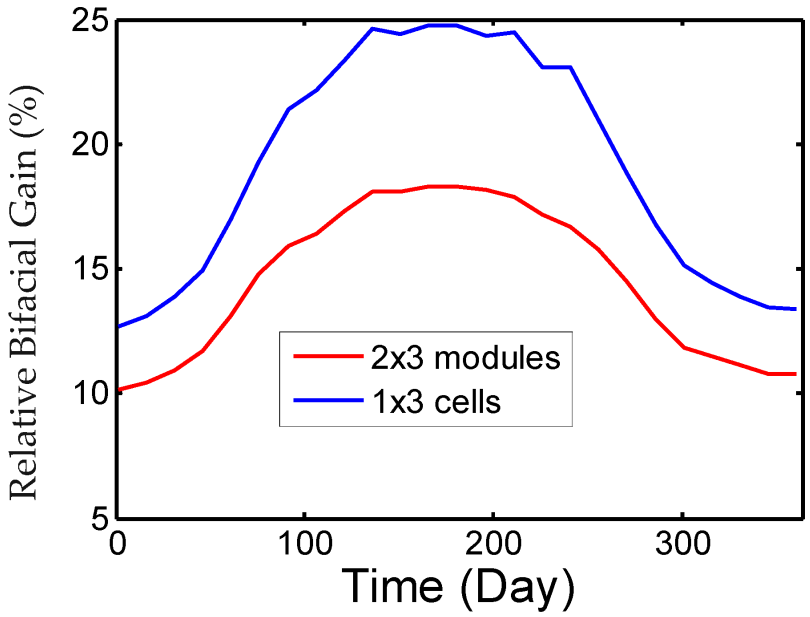

Figure 3.5: Modeled Bifacial Gain over the course of a year for a three-cell minimodule and a six-module array.

I have further investigated the subject of the uneven current production in bifacial system in [292]. I simulated the current produced by the back side of the modules in a 2-by-3 bifacial array and in a 2-by-6 array, both in landscape configurations, installed at a ground clearance of 2 m and a tilt angle of 35° at the latitude of Catania. This simulation has been carried

out for the sole spring equinox at 10 A.M., in order to obtain results that can be representative of the general trend throughout the year (whereas the solstices present more extreme situations) but also to emphasize the effects of asymmetrical illumination along the West-East direction. In these simulations, XA is the length of the ground extending beyond the array along the North-South direction and YB is the ground extension along the East-West direction. The currents produced by the back of specific modules in the array have been simulated for different YB values, with XA set to 5 m. The modules under focus were the central and the edge modules in the lower (southern) and top (northern) row of the arrays. From the values reported in Figure 3.6 it can be seen that the cur-

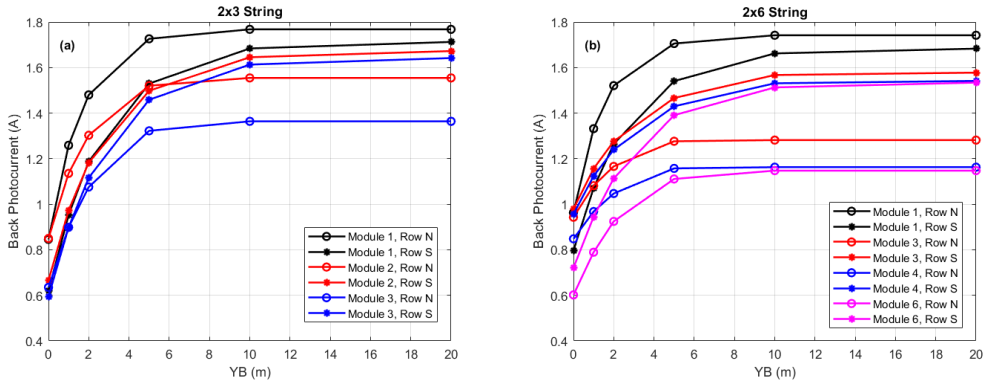

Figure 3.6: Back current of the central and edge modules for varying YB values for an array of 6 modules (a) and an array of 12 modules (b). XA is fixed to 5 m.

rent produced by the modules generally increases with YB up to 10 m, whereas further extensions of the ground surface would have a negligible effect on the current production. The current difference between the best and worst modules ranges from 0.2 A to 0.4 A for the smaller array and from 0.4 A to 0.6 A in the larger array. Besides, the first column of the array produced more current in both systems due to the asymmetrical position of the Sun with respect to the array. From these results it can be concluded that this current production unevenness evolves throughout the day and it is more pronounced in more horizontally elongated

systems.
In [293], the study of [291] has been expanded by investigating the correlation between the current output of the minimodules and the irradiance data. In this case, the bifacial minimodule has been placed on a 1 m^2 white plastic sheet (WPS), as shown in Figure 3.7. From the data of Figure 3.8, the I_{sc} is proportional to the frontal irradiance, both for the monofacial minimodule and the bifacial minimodule, with the additional albedo light contributing to a higher current in the latter; however, it can be seen that in the case of the bifacial minimodule the current output is higher in the afternoon than in the morning for the same frontal irradiance values (Figure 3.8b).

Figure 3.7: Picture of the experimental setup of [293].

This feature has been correlated with the increased infrared fraction of the solar spectrum in the afternoon and with the high responsivity of bifacial SHJ cells to infrared light. The albedo of the asphalt shown

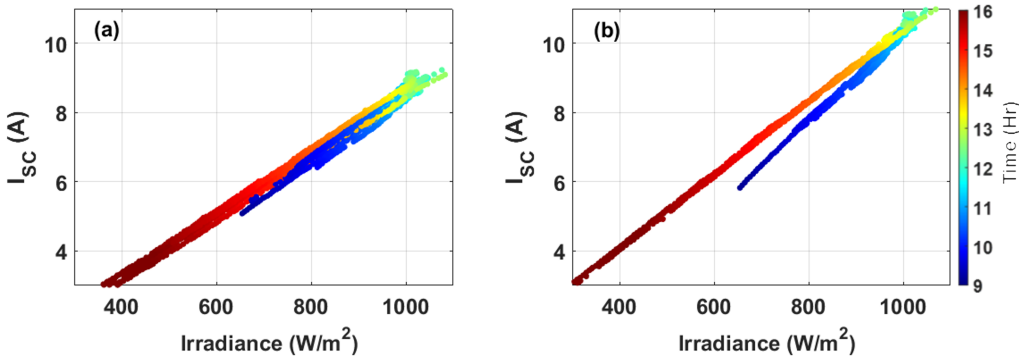

Figure 3.8: I_{sc} against frontal irradiance throughout the day for the monofacial minimodule (a) and for the bifacial minimodule (b).

in Figure 3.9a increases in the afternoon; this has been measured with two calibrated silicon photodiodes placed at the same ground clearance and tilt angles as the minimodules, and the albedo is calculated as the ratio of the current of the back photodiode over the current of the front photodiode. Additionally, the Central Spectrum Wavelength (CSW) of each spectrum is defined as [294]:

$$CSW = \frac{\int \phi(\lambda)\lambda \, \mathrm{d}\lambda}{\int \phi(\lambda) \, \mathrm{d}\lambda} \tag{3.41}$$

where $\phi(\lambda)$ is the measured photon flux of the solar spectrum. Another figure of merit usually reported to characterize spectra and directly related is the average photon energy APE:

$$APE = \frac{\int E(\lambda) \, \mathrm{d}\lambda}{q \int \phi(\lambda) \, \mathrm{d}\lambda} = \frac{hc}{CSW} \simeq \frac{1240 \; eV \cdot nm}{CSW} \tag{3.42}$$

where $E(\lambda)$ is the irradiance of the spectrum. Figure 3.9b shows an increase of CSW in the afternoon. These effects, in addition to the high reflectivity of asphalt and of the WPS reported in [287], result in a higher IR component in the reflected irradiance collected by the back of the bifacial minimodule. Moreover, these cells exhibit a high Detector Responsivity (DR) in the IR region. DR, measured in A/W, is defined as:

$$DR = \frac{q\lambda}{hc} EQE(\lambda) \tag{3.43}$$

The measured data of Figure 3.9c show that on both sides of a bifacial SHJ cell *DR* reaches its maximum after 1000 nm. Therefore, it has been concluded that the combination of high IR incident light and high responsivity resulted in a higher current output in the afternoon.

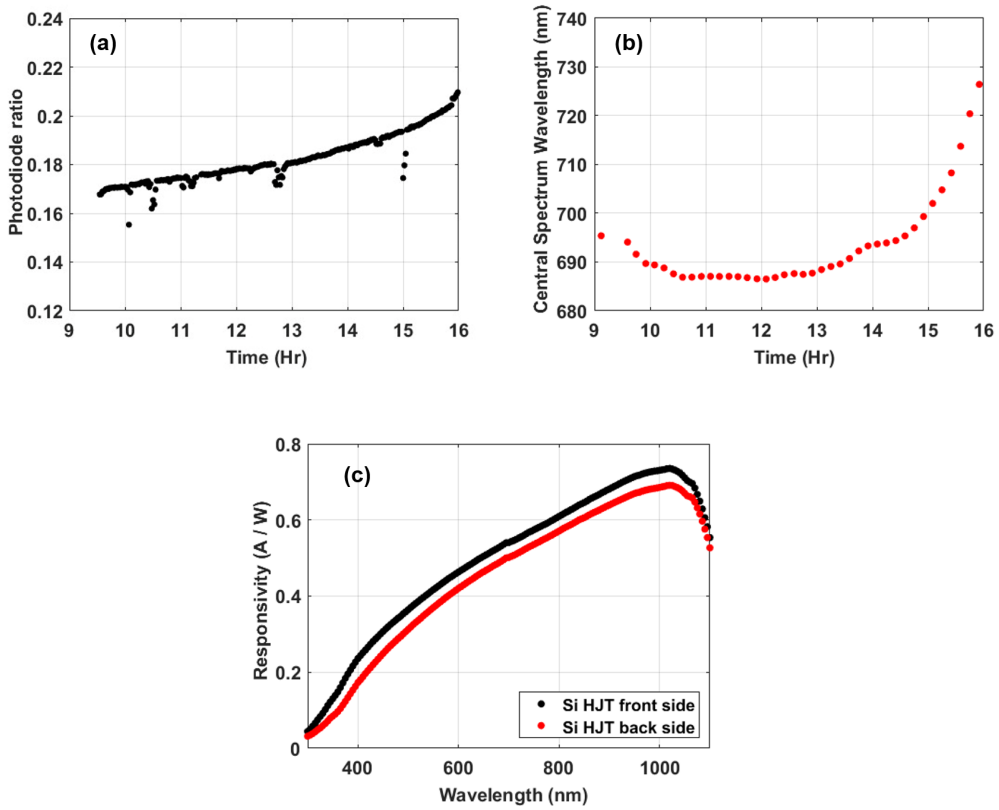

Figure 3.9: Albedo measured as the ratio of two photodiodes in the same position as the minimodules (a). Central Spectrum Wavelength calculated from the solar spectra registered during the day (b). Detector Responsivity of the front and back side of the SHJ cells in the minimodules (c).

In [295], I have used the model to investigate different configuration, focusing on the tilt angle for a full-size module facing south. A first set of simulations have been carried out for a ground surface of 20 m by 20 m, a ground clearance of 2 m and tilt angle ranging from 0° to 90°, evaluating the *BG* as defined in Equation (3.40) throughout the year.

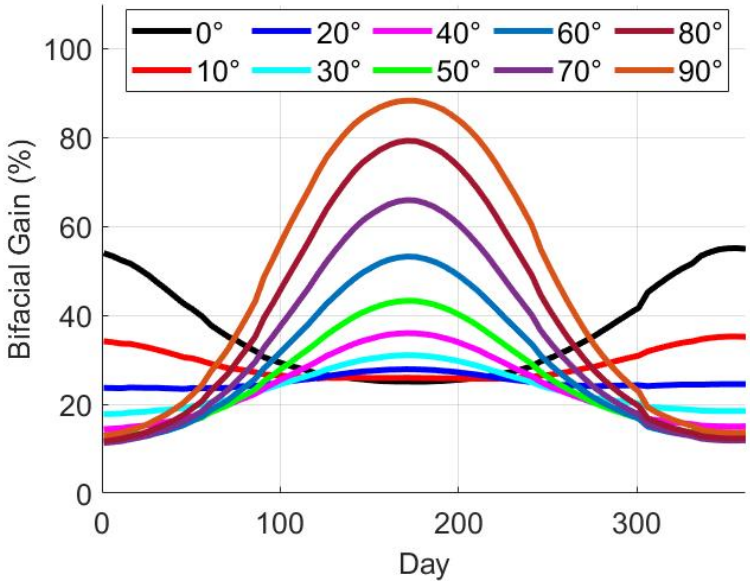

Figure 3.10: Bifacial gain throughout the year for different tilt angles for a module on a 20 m by 20 m asphalt surface.

The highest BG values are reached in summer and for high tilt angles (Figure 3.10): that is because the direct beam component weights less on the total light collected by the module due to its high incidence angle and the reflectivity of the glass of the module, whereas the front and back sides collect similar amounts of diffuse light according to Equation (3.12) and Equation (3.26), respectively, as β gets closer to $\frac{\pi}{2}$.

A second set of simulations have been performed in order to evaluate the shadow cast by the module facing south. To this end only three notable days have been considered: the spring equinox, assumed as an average configuration throughout the year, and the summer and winter solstices, representing the most extreme configurations. For each of these days I have calculated the fraction of shadowed area on a 20 m by 20 m surface, reported in Figure 3.11. The shadow occupies a small fraction of the total ground surface in spring and in summer, but becomes much larger in winter. Moreover, the largest shadow is cast at tilt angles between 40° and 50° in spring (Figure 3.11a), at tilt angles close to 0° in summer

(Figure 3.11b) and at tilt angles close to 90° in winter (Figure 3.11c).

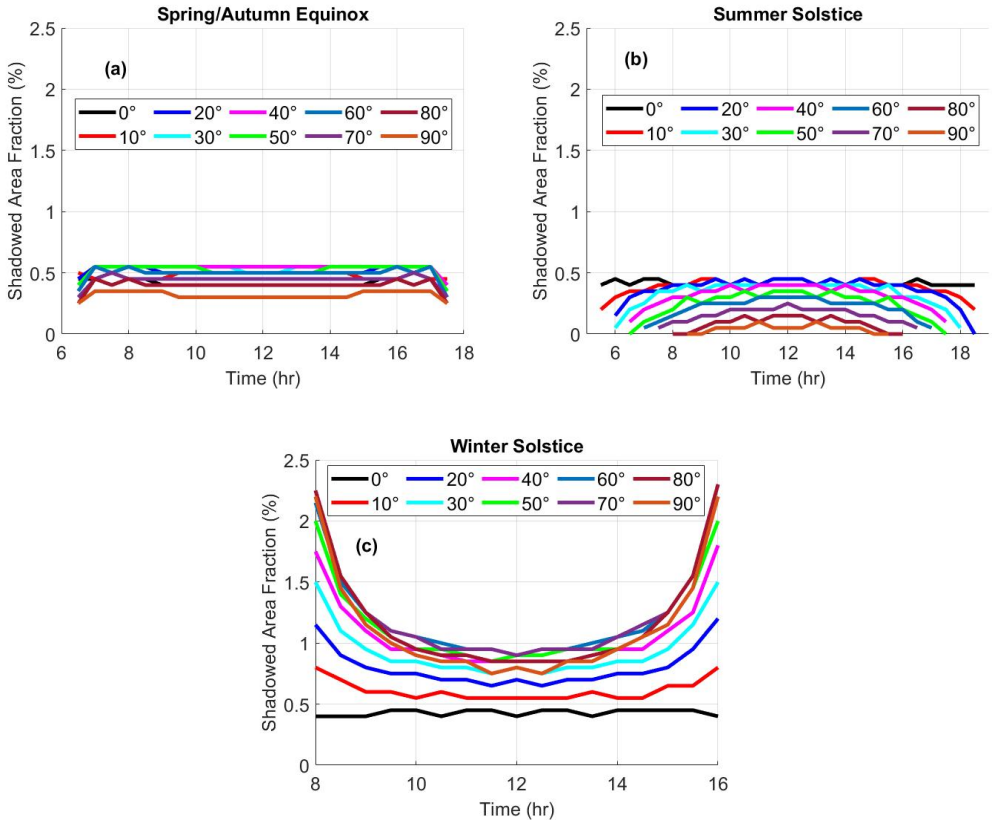

Figure 3.11: Fraction of shadowed area cast by the module on a 20 m by 20 m surface at the spring/autumn equinox (a), at the summer solstice (b) and at the winter solstice (c).

Chapter 4

Multijunction PV

The work of Shockley and Queisser [1] introduced an upper limit for any single-junction PV technology. In order to achieve higher efficiencies, the solution was to either use concentrating systems or increase the number of junctions with different bandgaps. As a side note, concentrator photovoltaics (CPV) has been quite popular in the last decades as the solar cells still represented a large fraction of the overall cost of the PV system, but has been declining in use as the cost of the module is nowadays mostly determined by the so-called balance of system (BOS), which encompasses all the other electrical and mechanical components such as wiring, mountings, inverters and storage systems [296].
As for multi-junction PV, the interest of the space research community lead to the development of the multi-junction GaAs technology [297], due to its radiation hardness, resulting in the first AlGaAs/GaAs prototype with a 9% efficiency being presented in 1978 [129] (as briefly mentioned in Section 1.6.1).

4.1 The theoretical limit

From a theoretical point of view, the first studies on the limit efficiency of multi-junction systems date back to the late 70's with the works of Parrott [298] and De Vos [299].
In his work, Parrott considered an edge-illuminated system made up by

segment of decreasing bandgaps: its derivation begins with the consideration that the generation rate $G(x)$ depends on the integral on all the available energies, which depend on the bandgap and therefore on x. This dependence translates into an integral expression for $\frac{\mathrm{d}J_{sc}}{\mathrm{d}x}$ and for $\frac{\mathrm{d}J_0}{\mathrm{d}x}$, and this allows the definition of $V_{oc}(x)$ as

$$V_{oc} = \frac{kT}{q} \ln\left(1 + \frac{\frac{\mathrm{d}J_{sc}}{\mathrm{d}x}}{\frac{\mathrm{d}J_0}{\mathrm{d}x}}\right); \tag{4.1}$$

then, the locally generated power can be expressed as

$$\frac{\mathrm{d}P}{\mathrm{d}x} = F\frac{\mathrm{d}J_{sc}}{\mathrm{d}x}V_{oc}(x) \tag{4.2}$$

which can then be integrated over x to obtain the total power of the system. Parrott derived an integral expression for the efficiency η, and obtained that for the spectrum of a 6000 K blackbody η would be 64% at 1 sun illumination, 77% at 1000 suns and 81% at 10000 suns.
The approach employed by De Vos is more reminiscent of that by Shockley and Queisser: in a system made up by n cells with decreasing bandgap in series at the same temperature T_c, the i-th I-V characteristics is given by

$$I_i(V_i) = I_{sci} - I_{0i}\left(e^{\frac{qV_i}{kT_c}}\right) \tag{4.3}$$

and, in analogy with the analysis of Shockley and Queisser, the dark saturation current is determined only by radiative recombination:

$$I_{0i} = qF_{0i} = 2qA\int_{\frac{E_{gi}}{h}}^{\infty} N(\nu, T_c)\,\mathrm{d}\nu \tag{4.4}$$

with F being the photon flux, A the area of the solar cell and

$$N(\nu, T) = \frac{2\pi}{c^2}\frac{\nu^2}{e^{\frac{h\nu}{kT}} - 1} \tag{4.5}$$

is the blackbody radiation at temperature T. The photocurrent of the cell is given by

$$I_{sci} = q\left(F_{si} - F_{0i}\right) \tag{4.6}$$

where F_s is the incident photon flux. The first cell of the stack is illuminated by the Sun and by the light emitted by the second cell:

$$F_{s1} = fA \int_{\frac{E_{g1}}{h}}^{\infty} N(\nu, T_s)\,\mathrm{d}\nu + Ae^{\frac{qV_2}{kT_c}} \int_{\frac{E_{g1}}{h}}^{\infty} N(\nu, T_c)\,\mathrm{d}\nu \tag{4.7a}$$

where f is the geometrical factor dependent of the solid angle subtended by the light source. Besides, it must be noted that the lower bound of the second integral depends on E_{g1} rather than E_{g2} as it is assumed that each cell can only absorb photons with energy equal or greater than its bandgap. The general i-th cell in the stack receives emitted light from the cell above and below, whereas sunlight has been filtered by the previous cells:

$$F_{s1} = fA \int_{\frac{E_{g1}}{h}}^{\frac{E_{g1-1}}{h}} N(\nu, T_s)\,\mathrm{d}\nu + Ae^{\frac{qV_{i-1}}{kT_c}} \int_{\frac{E_{gi-1}}{h}}^{\infty} N(\nu, T_c)\,\mathrm{d}\nu + Ae^{\frac{qV_{i+1}}{kT_c}} \int_{\frac{E_{gi}}{h}}^{\infty} N(\nu, T_c)\,\mathrm{d}\nu \tag{4.7b}$$

while the last cell in the stack does not have another cell below it:

$$F_{sn} = fA \int_{\frac{E_{gn}}{h}}^{\infty} N(\nu, T_s)\,\mathrm{d}\nu + Ae^{\frac{qV_{n-1}}{kT_c}} \int_{\frac{E_{gn-1}}{h}}^{\infty} N(\nu, T_c)\,\mathrm{d}\nu \tag{4.7c}$$

The overall power of the system is $P = \sum_{i=1}^{n} V_i I_i$, which is maximized by the system of n equations $\frac{\partial P_i}{\partial V_i} = 0$. Solving the system also yields the working points of each cell. Before generalizing to an infinite number of cells, it is useful to introduce $x_i = \frac{qV_i}{kT_c}$ and give the form of the i-th equation of the system:

$$(1 + x_i)e^{x_i} = \frac{F_{si}}{F_{0i}} + \frac{1}{2}x_{i-1}e^{x_i} \frac{\int_{\frac{E_{gi-1}}{h}}^{\infty} N(\nu, T_c)\,\mathrm{d}\nu}{\int_{\frac{E_{gi}}{h}}^{\infty} N(\nu, T_c)\,\mathrm{d}\nu} + \frac{1}{2}x_{i+1}e^{x_i} \tag{4.8}$$

When the number of cells tends to infinite and the bandgap difference between adjacent cells becomes infinitely small, the discrete quantities become continuous: $x_i \to x$, $x_{i\pm1} \to x \pm \mathrm{d}x$, $E_{gi} \to E_g$ and $E_{gi\pm1} \to E_g \pm \mathrm{d}E_g$. It must be noted that in order to make these substitutions $x(E_g)$ must be a continuous function, which means that the loads on the infinite

cells in the stack must also vary continuously. With these substitutions Equation (4.8) becomes

$$(1+x)e^x = f\frac{N(\frac{E_g}{h}, T_s)}{N(\frac{E_g}{h}, T_c)} \tag{4.9}$$

and the overall maximum power is given by

$$P_{max} = A\frac{kT_c}{h}\int_{\frac{E_{gn}}{h}}^{\infty} x^2 e^x N(\frac{E_g}{h}, T_c)\,\mathrm{d}E_g \tag{4.10}$$

which depends on the last and smallest bandgap of the stack. It must be noted that E_{gn} must be chosen so that $x(E_{gn}) = 0$, as otherwise cells with a lower bandgap would operate at negative voltages. With these constraints, De Vos reports a maximum theoretical efficiency of 68.2% at 1 sun.

Other works include that of Henry [300], in which the author determined the maximum work per absorbed photon and then calculated the limiting efficiency for a finite number of cells where the bandgap differences had been tuned in order to eliminate current mismatch in the stack. Herny reports efficiency of 37%, 50%, 56% and 72% for stacks with 1, 2, 3 and 36 cells, respectively, at a 1000 suns concentration (which is the only case considered in his work because, as the author states, "[...] multiple energy gap cells are expected to be used only in concentrators having relatively high concentrations. Only then can a complex and costly cell be afforded").

In [301], Martí and Araújo use a similar method to that of De Vos but also considering the case in which each cell of the stack has a reflector behind it suited to its bandgap, finding efficiencies of 69.9% and 86.8% at no concentration and maximum concentration, respectively, for the 6000 K blackbody spectrum, while these figures decrease to 65.4% and 85.0% for the $AM1.5$ direct spectrum. Maximum concentration corresponds to the ideal case in which the light source covers the entire solid angle, that is $f = 1$ or $\frac{\pi}{\Omega_s} \simeq 46000$ suns [300] as the solid angle subtended by the sun is $\Omega_s \simeq 6.8 \cdot 10^{-5}$ steradians. In [302], Brown and Green expanded the work of Martí and Araújo for different numbers of cells, concluding that the efficiency gains tend to decrease after more than 10 cells are

added to the stack, at which point the efficiency of the system would reach 80% at maximum concentration, with a slight efficiency loss for the series-constrained case.

4.2 Two-, three- and four-terminal systems

The essence of multi-junction modules is the combination of semiconductors with different bandgaps in order to reduce thermalization losses and collect solar light more efficiently over a broad range of wavelengths. However, said combination encompasses two different aspects: the optical coupling and the electrical coupling. Each of these two can be implemented in different ways, giving rise to several diverse solutions and module designs.

The two most diffused ways to achieve optical coupling are the cell stacking and the optical splitting: in the former design, the cells are stacked on top of each other in a single monolithic system and the light splitting is obtained by filtering high photons from the upper cells to lower cells, which are ordered by decreasing bandgaps. This is the most common approach, largely used in space applications [303], and with many prototypes exceeding 30% efficiency [304].

In the latter design, the cells are physically separated and optic elements like gratings [305, 306], prisms [307, 308], dichroic mirrors [309, 310, 311] and holographic elements [312, 313] redirect each selection of the solar spectrum to the cell most suited to absorbing it.

Other designs that have been tested include an integrating sphere-like system whose internal walls are characterized by solar cells with different bandgaps and covered by band-pass filters [314, 315]: light is continuously reflected and scattered inside the system until it is allowed to pass through the suitable filter and absorbed by the corresponding cell.

Another designs consists in arranging a series of cells and selective filters in a path so that light is redirected from one cell to the other, with each cell absorbing its fraction of the spectrum as the rest is reflected to the next element [314, 316].

As for the electric coupling, the simplest approach consists in not actually coupling the cells: in fact, once each cell receives the appropriate

range of photons, separate circuits can be connected to extract power independently from the others. The main advantage of this implementation, which is usually called four-terminal (4T) for two-cell systems, is that it allows to extract the maximum power possible from each cell; the downside is that large utility scale or even residential systems would require double the electric components, increasing BOS [317] costs and chance of system failures, therefore this design is more suited to small laboratory scale prototypes.

The most common approach, however, is the two-terminal (2T) connection, in which all cells are inserted in the same electrical circuit. In this case, the choice between connecting the cells in series or in parallel becomes crucial: the series connection requires that the currents of all cells are matched to the same value in order to maximize the power increase, as the current of the whole system is limited to the lowest of all cells [318], while the parallel connection requires voltage matching in a similar way [319]. The series connection is especially convenient in monolithic devices, while the parallel connection requires different numbers of cells for each semiconductor to be connected in series first in order to achieve the same voltage output, as the V_{oc} mostly depend of the bandgap of the semiconductor: in fact, only modules can effectively be connected in parallel, making the manufacturing of these system much more complex. However, the current produced by a solar cell is proportional to the photon flux, whereas its voltage output varies logarithmically, as shown in Equations (1.14) and (1.15): for this reason, once installed in the field, the parallel connection is in principle more robust to spectral variation, which are to be expected throughout the day and because of the weather, than the series connection.

Another recent approach is the three-terminal (3T) design, which combines the ease of manufacturing of series-connected monolithic devices with the lack of current matching and robustness to spectral variations of parallel-connected devices [320]: in fact, this approach was introduced to overcome the current mismatch in triple-junction GaInP/GaAs/Ge solar cells, where Ge was current-limited by the other two junctions due to the broad range of photon energies it can absorb [321]. The first design consisted of an AlGaAs cell over an IBC cell (the original work featured a Si IBC cell since this cell design had already been developed for silicon),

so that the electrons generated by the top cell would be collected by the contact on the emitter of the top cell, while the IBC cell would collect the electrons generated by the cell itself at the contact on the emitter and the holes generated by both cells at the contact on the base. This allows power to be extracted separately from each cell. The two cells are usually grown epitaxially on top of each other or connected by wafer bonding [322, 323], although devices with a middle contact between the two absorbers have also been proposed in order to bypass the need of a tunnel junction [324]. 3T devices can match the power output of 4T devices [325], but they are much more complex to model [326] and operate, as two voltage biases need to be tuned in order to extract the maximum power [320], and this complexity also carries over to the different schemes in which 3T cells can be connected in a string [327].

4.3 Implementation of a parallel-2T bifacial device

In [311], I have realized a parallel-connected 2T (P2T) GaAs/bifacial SHJ device. The GaAs module was made up by two commercial reference GaAs cells [328] connected in series: each cell had an active area of 20 mm $\times$ 20 mm, was protected by a 104 mm $\times$ 74 mm $\times$ 16 mm housing (Figure 4.1a) and under STC the PCE was about 20%, its V_{oc} was 1.0 V and its J_{sc} was 25 mA/cm^2.
The bifacial SHJ cell had been manufactured by Enel Green Power (EGP) [329, 330, 331]. Under STC, these cells, realized in M2 pseudo-square format, show a V_{oc} of about 730 mV, a J_{sc} of 38 mA/cm^2, a bifaciality factor of about 90% and a PCE of 23%. In order to match the size and voltage output of the GaAs module, three cells of appropriate size had to be joines in series, so that each module would have a V_{oc} of about 2 V. For this purpose, a single EGP M2 SHJ cell has been cut by mechanical scribing along the easy-cleavage (110) directions [332], and the resulting 13 mm $\times$ 20 mm fragments cell have been connected in series by soldering silver-coated copper ribbons. Considering that the unconvential manufacturing process might introduce defects in the cells, several samples have been realized and compared, with the best performing sample

chosen for the implementation in the final device [333]. Each module had the same active area of 8 cm^2, which has been considered as the active area of the whole device. As shown in Figure 4.1b, the SHJ module has been placed on a glass slide having dimensions 75 mm $\times$ 16 mm $\times$ 1 mm as a transparent support, allowing the module to collect albedo irradiance on its back.

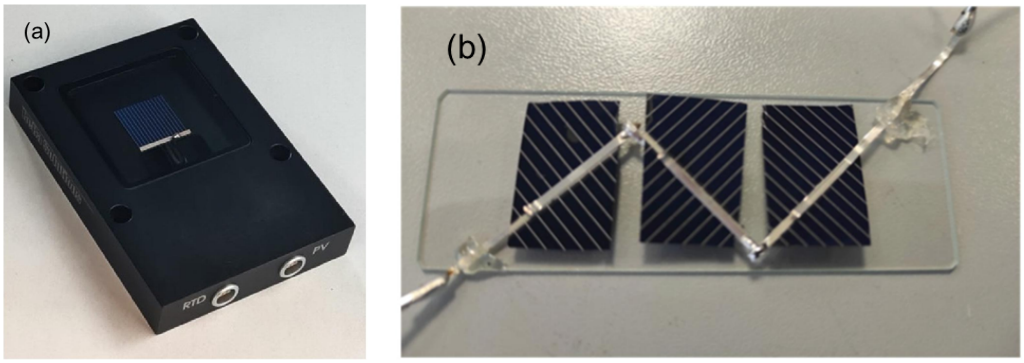

Figure 4.1: Picture of the GaAs cell (a) and of the bifacial SHJ minimodule placed on the glass slide (b). The GaAs cell is 20 mm $\times$ 20 mm wide and the SHJ mini-module is made up by three 13 mm $\times$ 20 mm cells connected in series through silver-coated copper ribbons.

Two long-pass dichroic mirrors manufactured by Thorlabs [334], both having dimensions 25 mm $\times$ 36 mm $\times$ 1 mm and a cut-on wavelength of 805 nm, have been used to split the incident light. As depicted in Figure 4.2, the mirrors were positioned perpendicular to each other, so that the angle of incidence of direct solar light would be 45°.
To evaluate the optical coupling of the modules and dichroic mirrors, I measured the transmittance and reflectance of the mirrors at an AOI of 45° and the EQE of the GaAs cell and of the front and back sides of the SHJ cells with a Bentham PVE300 Photovoltaic Characterization system. The data reported in Figure 4.3 show that the mirror cut-on wavelength of about 805 nm differs by about 50 nm from the upper bound of wavelengths suitable for GaAs.
The modules have also been characterized by measuring the J-V characteristics under STC before assembling the P2T device (Figure 4.4a) and

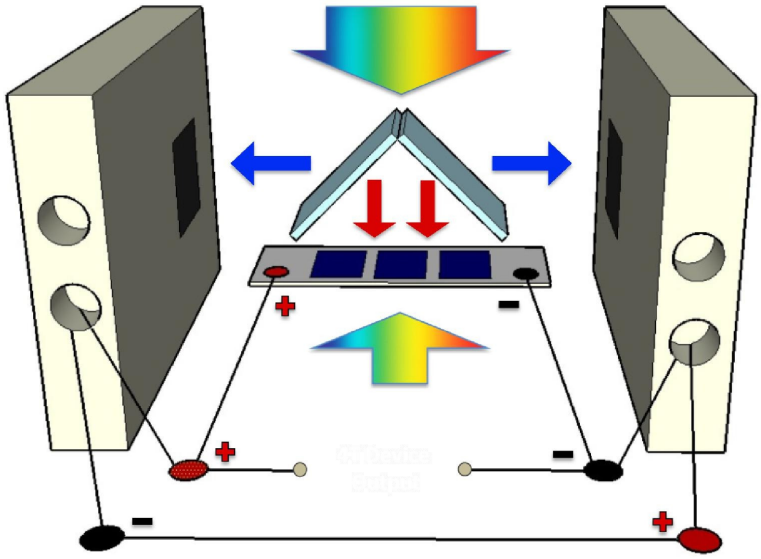

Figure 4.2: Graphic representation of the optical and electrical coupling of the P2T device. Incoming light (multicolor) impinges on the dichroic mirrors: visible light (blue) is reflected to the GaAs cells, while infrared light (red) is transmitted to the SHJ cells. The SHJ cells also collect all light impinging on the rear of the module.

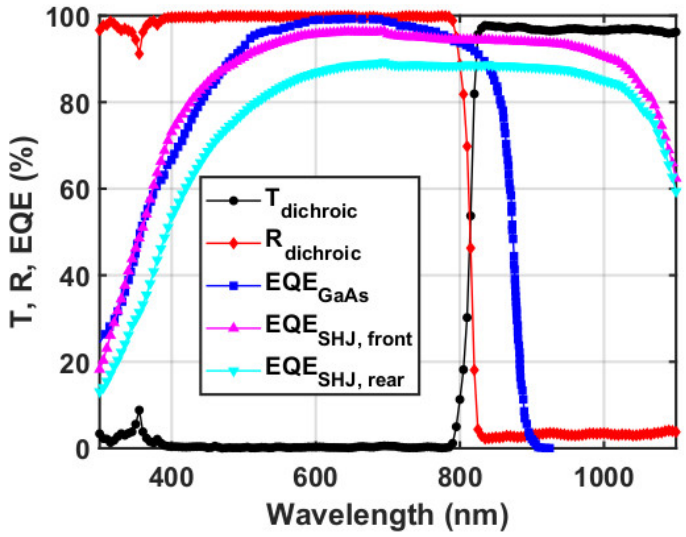

Figure 4.3: Transmittance and reflectance data of the dichroic mirrors ($AOI = 45°$) compared with the EQEs of the GaAs and SHJ cells. The cut-on wavelength of the mirror resulted 805 nm, confirming the value reported by the manufacturer.

by measuring the I-V characteristic of each module and of the whole device after it had been assembled (Figure 4.4b). For the SHJ module, a PCE of 18.2% has been measured before assembling the device, much lower than the original value for the M2 cells. This large decrease has been mainly ascribed to three effects: the V_{oc} decrease due to the mechanical cut from 730 mV down to 680 mV, the series resistance increase due to the unconventional series connection by soldered ribbons and the glass slide isolating the module from the temperature controlled chuck during the measurement, which lead to an increase in cell temperature affecting the resulting efficiency. For the GaAs mini-module, the measured PCE was equal to 20.1%, similar to the value reported by the manufacturer.
Once the GaAs and SHJ modules had been assembled in the P2T device, the current measured in each module decreased with respect to the previous values: this is due to the optical splitting of the dichroic mirrors, which also affects the GaAs module because of the slight mismatch between the cut-on wavelength of the mirror and the EQE spectrum of GaAs shown in Figure 4.3. The overall PCE of the P2T device was of 24.83%, larger than the values of each module, with a voltage mismatch smaller than 0.2 V.

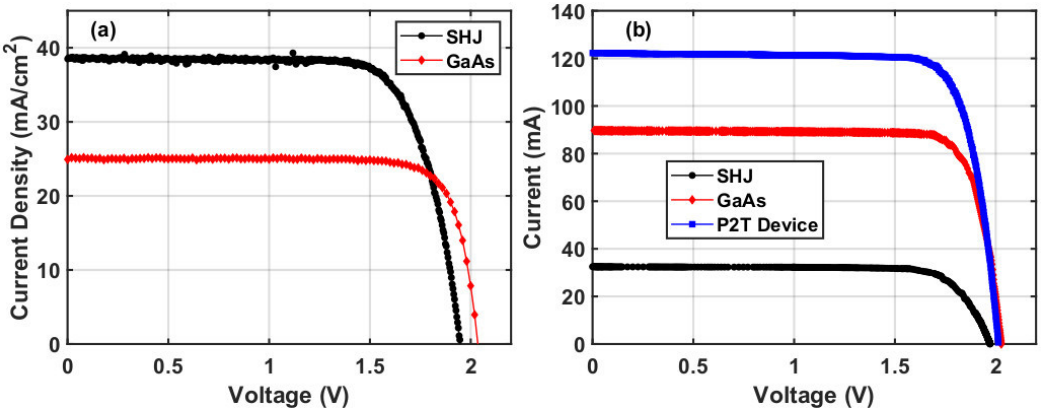

Figure 4.4: J-V characteristics of the modules under STC (a) measured without interposing the dichroic mirrors between the modules and the light source. I-V characteristics (b) of the individual modules and of the whole P2T device at STC.

The P2T device has been tested in outdoor in Catania (37°26′30″N) in January 2022. The whole system was anchored to an EGIS EPR-203 bi-axial solar tracker in order to receive solar radiation at the desired AOI. In fact, the supporting structure and GaAs cell housings limit the diffuse light that can reach the mirrors, and the tracker is therefore necessary for the device operation. A picture of the setup is reported in Figure 4.5a. The spectral distribution of solar light from 300 nm to 1100 nm has been monitored using an optical fiber mounted on the tracker connected to a monochromator (Newport, model: CS130-RG-1-MC). The I-V characteristics of the P2T device have been measured with the same setup employed in the previous work on bifaciality [291] and whose electric scheme is reported in Figure 4.5b: the voltage across the device was swept by a variable load, applied by driving an STP60NF06 power MOS from OFF to ON condition with a linear staircase signal applied to the transistor gate, while the current was evaluated by the voltage drop across a 10 mΩresistor connected in series to the device. The electrical data, collected from 9 A.M. to 5 P.M., have been acquired through an USB-6343 National Instrument data logger. The setup registered a single point of the I-V curve every 0.05 s, a complete I-V curve every 26 s and a complete solar spectrum every 220 s [333]. Periodically, groups of five I-V curves have been acquired while covering the back of the SHJ module with a black plastic sheet to block the albedo light, in order to evaluate the contribution of the bifaciality to the overall performance of the P2T device.

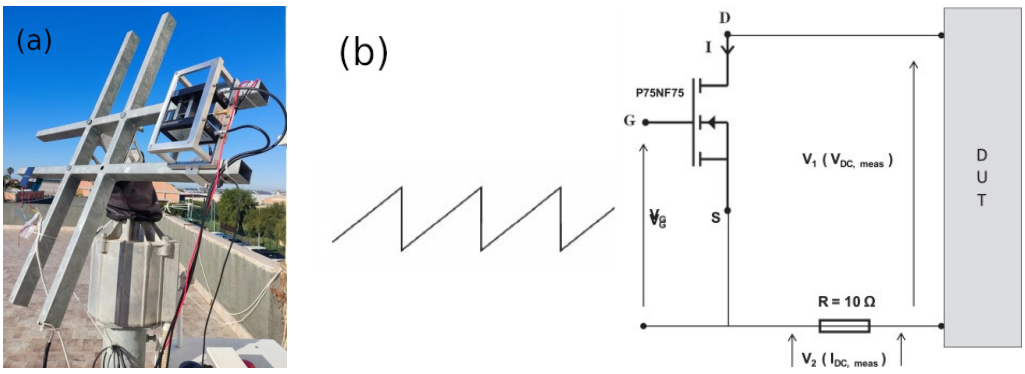

Figure 4.5: Picture of the outdoor setup (a). Electrical scheme of the I-V measurement setup (b).

Figure 4.6 reports the V_{oc}, I_{sc} and PCE data registered during the experiment: the voltage match between the two mini-modules resulted quite stable during all day, as the V_{oc} of the device remained above 2 V until 4 P.M. (Figure 4.6a); conversely, I_{sc} shows a definite trend during the day, registering its maximum values between 11 A.M. and 1 P.M. (Figure 4.6b). As for the impact of the bifaciality of the SHJ module, it can be seen that it contributes positively to the device in terms of both voltage and current gains, as these quantities registered higher values in the bifacial configuration: this implies that the additional current produced by the bifacial SHJ module does not impair the voltage match between the two modules, whereas the current match would require tuning the design of both modules in advance while taking into account whether the bottom module will be bifacial or not, making the design and the manufacturing process less flexible.
The PCE for each I-V curve is reported in Figure 4.6c. The highest value registered during the measurement period is 25.4%, slightly higher than the value obtained during the indoor characterization phase. This difference has been attributed to the effect of the higher albedo irradiance available in the outdoor test site compared to the indoor measurement setup. Moreover, factors such as the spectral distribution of incoming light, ambient temperature and wind speed are also expected to differ between indoor and outdoor conditions. Similarly to the case of V_{oc}, PCE data show a considerable stability over time compared to I_{sc}, from a maximum of 25.4% to a minimum of 21.3%, corresponding to a variation of 16% of the maximum value. Moreover, the values registered in the monofacial configuration range from 18.4% to 21.4%, with a variation of 16% of the maximum value. Therefore, it had been concluded that the bifaciality of the SHJ module brought an average PCE increase of 17% during the day, confirming the stability of the parallel connection throughout the day.

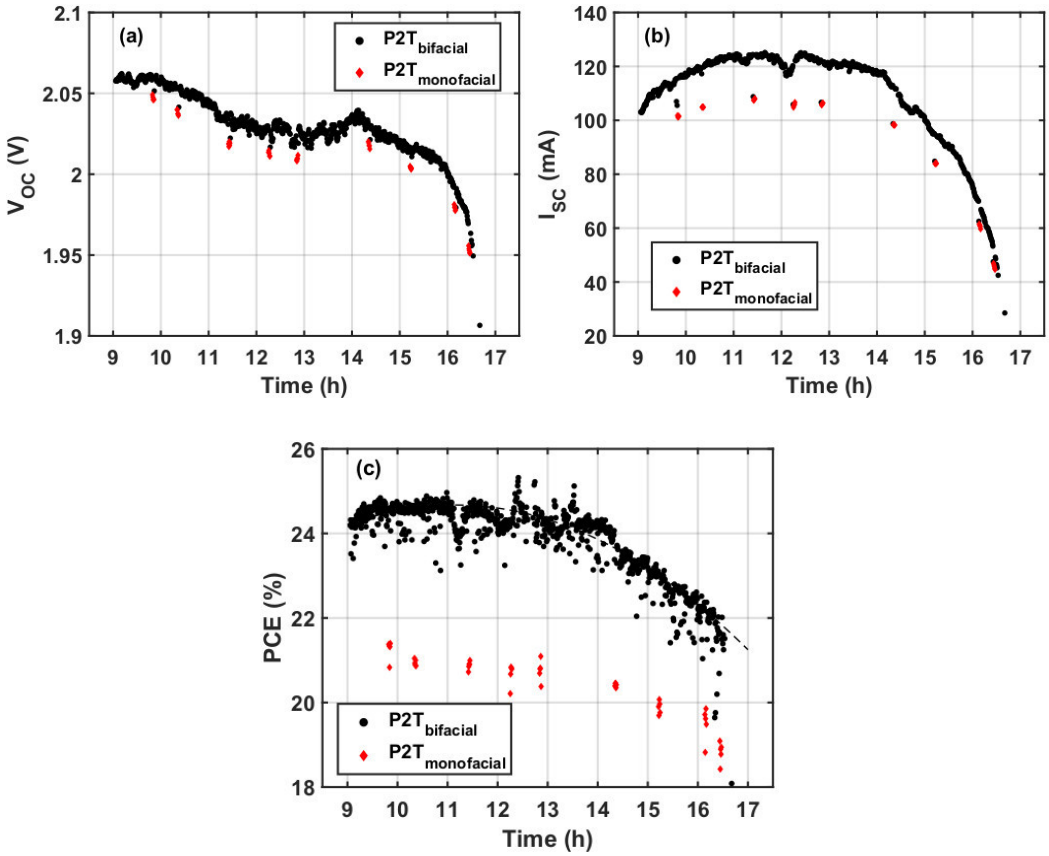

Figure 4.6: V_{oc} (a), I_{sc} (b) and PCE data of the P2T device during the day. Black dots indicate the data obtained with the bifacial configuration ("$P2T_{bifacial}$"), whereas red diamonds indicate the data obtained with the monofacial configuration ("$P2T_{monofacial}$").

Spectral distribution data of solar light had been registered during the outdoor measurement by sending light to a monochromator with an optic fiber and reading the current generated by a calibrated Si cell at the exit of the monochromator. From each spectrum the CSW has been calculated from Equation (3.41), and the data reported in Figure 4.7a show a minimum around midday and an increase of up to 80 nm in the afternoon. In [333] this quantity has been correlated with the fraction of photons that the dichroic mirrors send to each module: from Figure 4.7b it can be seen that there is a linear correlation between these quantities. This

also implies that the weights of the current contributions from the two modules to the overall current of the device change during the day, with the SHJ module overcoming the GaAs module for CSWs larger than 760 nm (corresponding to 4 P.M. in January), showing again that the parallel connection is impervious to spectral variations during the day, whereas a series connected device would always be limited to the lowest of the individual currents.

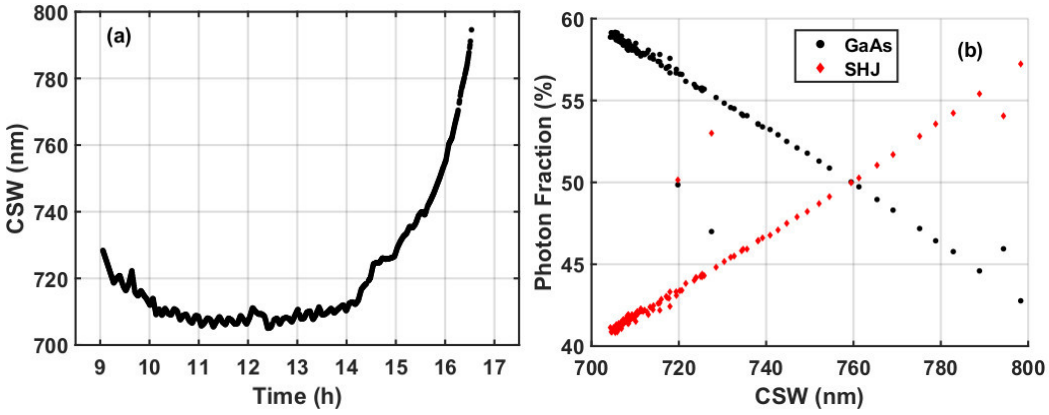

Figure 4.7: *CSW* data of all spectra (a). Fractions of photons reflected to the GaAs (black) and SHJ (red) modules (b).

Lastly, in [335], I have tested the same P2T device with specific albedo conditions (as opposed to the residential background of the previous work). Four paper sheets have been placed behind the SHJ module, at a distance of about 20 cm, each of a different color: white, gray, orange and green (Figure 4.8), in order to mimic common albedo conditions such as snow, asphalt, rooftop shingles and grass, respectively. The reflectivity of each sheet had been characterized with an integrating sphere, obtaining that the data are more varied in the visible part of the spectrum, whereas each paper sheet had higher reflectivity in the IR region (Figure 4.9a). Moreover, while it is to be expected that the white paper sheet would be the most reflective, the reflectivity of the green sheet is comparable to that of the black sheet in the visible region and even inferior in the IR region. For each paper sheet, a set of I-V characteristics has been registered in the bifacial and monofacial configurations. Figure 4.9b reports the rela-

tive PCE increase between the two configurations for each paper sheet: by comparing the increase ranking with the reflectivity ranking, it can be concluded that that the more reflective sheets contribute more to the bifaciality of the SHJ module. This would not be surprising in a single-junction system, but in this setup it confirms that the same parallel-connected 2T device can be employed in different albedo conditions.

Figure 4.8: Pictures of the P2T device mounted on the bi-axial solar tracker with a gray, white, orange and green paper sheet.

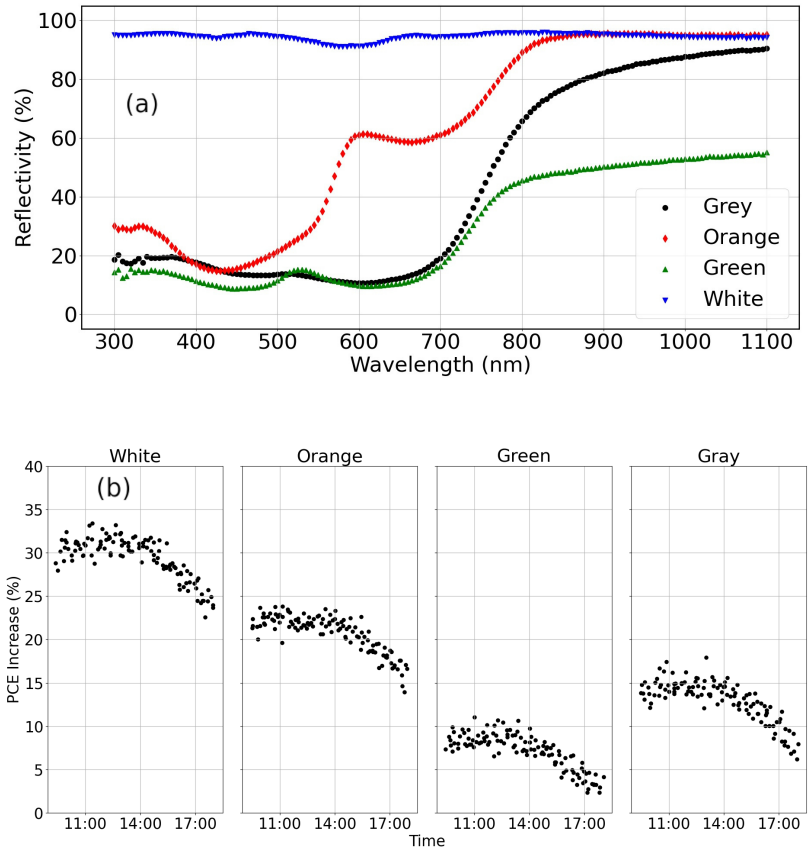

Figure 4.9: Reflectivity values of the four paper sheets in the 300 nm – 1100 nm range (a). Relative *PCE* gains compared to the monofacial configuration with the four colored paper sheets in (b).

Chapter 5

Innovative material characterization

As part of my research activities I have collaborated with other research groups on the characterization of new materials for silicon solar cells.
One of such activities, realized in collaboration with Consiglio Nazionale delle Ricerche - Istituto per la Microelettronica e Microsistemi (CNR-IMM) regarded the development of sub-stoichiometric molybdenum oxide (MoO_{3-x}) as a hole-selective contact in SHJ solar cells. Though the effectiveness of MoO_{3-x} has already been examined in other works [336], the goal of this study is to achieve good performance with films deposited by sputtering rather than evaporation, as this would represent an important step towards the upscaling to industrial applications. To this end, it is necessary to identify the optimal process conditions that permit both a great control of MoO_{3-x} stoichiometry and of the Si/MoO_{3-x} interface: in fact, the stoichiometry determines properties of the oxide such as the bandgap and the work function. However, oxygen vacancies generate intra-bandgap donor defect states [337], improving conductivity but also decreasing the optical transparency of the film.
Two samples have been realized: one with a 7 nm MoO_{3-x} film ($0 < x < 0.4$) replacing the p+ side of the a-Si (i)/a-Si (p+) passivation layer and one without any a-Si passivation layer. MoO_{3-x} has been deposited by sputtering at ambient temperature, followed by ITO sputtering at ambient temperature under Ar and O_2 flow; then the samples have been

annealed at 200 °C under N_2 flow. The stoichiometry of the MoO_{3-x} film has been tuned by controlling the the Ar pressure during the RF sputtering and then characterized by Rutherford backscattering spectrometry (RBS) and X-ray photoelectron spectroscopy (XPS). These samples, realized on flat substrates, have been compared with a flat reference SHJ cell. I have measured the EQE and reflectivity of the sample to determine the Internal Quantum Efficiency (IQE) as

$$IQE = \frac{EQE}{1 - R - T} \tag{5.1}$$

where R and T are the reflectance and transmittance of the cell. The passivated MoO_{3-x} sample shows higher EQE and IQE than the flat reference sample, especially for wavelengths below 600 nm.

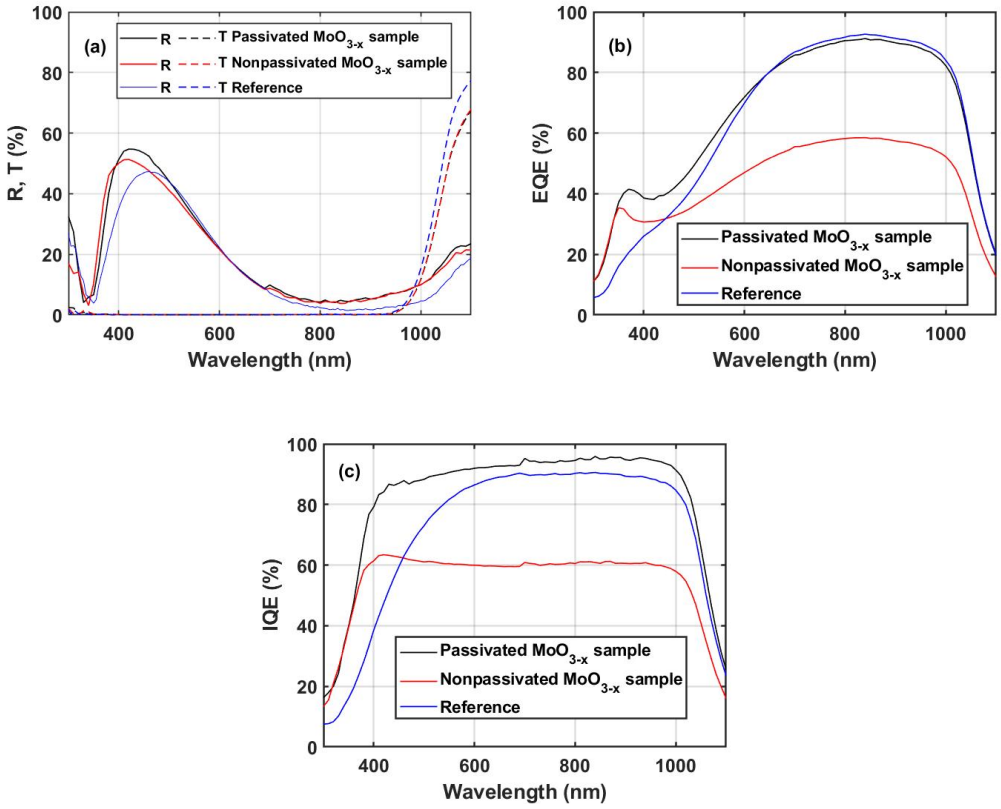

Figure 5.1: Reflectance and transmittance (a), EQE (b) and IQE (c) of the passivated and nonpassivated MoO_{3-x} SHJ cells and of the reference cell.

Another activity, in collaboration with Università degli studi di Catania (UniCt), concerned the development of new anti-reflection coatings for SHJ cells. The goal of this research is too reduce the indium consumption in this type of cell: in fact, indium is considered a critical material due to its low abundance [338].
The first phase of this study consisted in substituting ITO with another TCO, namely Zr-doped indium Oxide (IZrO). IZrO is a TCO characterized by a bandgap above 3 eV (depending on the Zr doping), high mobility and high transparency in the near-infrared wavelength range [339, 340, 341]. Initially, IZrO films with thickness ranging from 10 nm to 100 nm have been grown on a glass substrate for characterization. The films have been realized by co-sputtering from separate targets and then annealed at 200 °C for 30 min under N_2 flow: this process has been chosen with the idea of allowing easy scalability to industrial applications. The results of the electrical characterization are reported in Table 5.1.

Sample	Resistivity (Ω/cm)	Hall mobility (cm^2/Vs)
20 nm	$1.4 \cdot 10^{-3}$	2.65
20 nm annealed	$3.6 \cdot 10^{-4}$	8.40
50 nm	$1.4 \cdot 10^{-3}$	3.17
50 nm annealed	$3.2 \cdot 10^{-4}$	9.61
100 nm	$1.6 \cdot 10^{-3}$	2.72
100 nm annealed	$4.1 \cdot 10^{-4}$	10.3

Table 5.1: Electrical characterization of IZrO films before and after annealing (30 min, 200 °C, N_2 flow).

Successively, solar cell samples have been realized in which IZrO substituted ITO on the n-side or on the p-side. I have performed *EQE* measurement on these samples: samples with IZrO on the p-side showed generally higher *EQE* than the other group, and in general an efficiency loss can be observed for short and long wavelengths (Figure 5.2). This losses have been attributed to absorbance by the IZrO film in the ultraviolet/visible region and to interference effect due to the unoptimized thickness of the film to achieve anti-reflection. The next phase of this research will focus on the introduction of an SiO_2/IZrO bi-layer, in order to

optimize the film thickness for the anti-reflection effect without increasing the indium content of the cell.

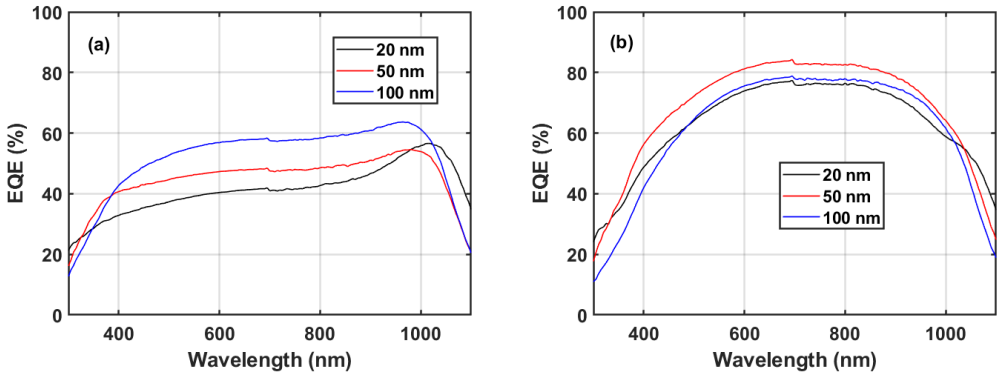

Figure 5.2: External Quantum Efficiency measurement of SHJ cell with an IZrO anti-relfection coating on the n-side (a) and on the p-side (b), with film thickness from 20 nm to 100 nm.

A third activity, in collaboration with UniCt, aims at the development of plasmonic-enhanced solar cells. In fact, noble metal nanoparticles (NPs) generate surface plasmons when excited by light with wavelength greater than the size of the nanoparticles [342], resulting in enhanced light absorption at the plasmon resonance frequency, which in turn depends on the shape and size of the nanoparticles. In the context of solar cells, plasmonic nanostructures are being studied not only for their increased absorption, but also for increasing the optical path length by scattering [343]. In particular, copper is an interesting candidate due to its absorption peak lying between 590 nm and 630 nm, although it is more sensible to oxidation compared to other metals such as gold and silver [344].
Cu NPs have been obtained by laser ablation in a liquid Cu target using a 1064 nm nanosecond pulsed laser in acetone and methanol, then they have been characterized with several techniques including Scanning Electron Microscopy (SEM), High-Resolution Transmission Electron Microscopy (HR-TEM), Energy Dispersive X-Ray (EDX) and Electron Energy Loss Spectroscopy (EELS), X-ray Diffraction (XRD) and XPS, from which resulted a larger fraction of NPs with radius below 3 nm and rarer NPs

with radius larger than 15 nm. These nanoparticles have been embedded in an AZO/IZrO double stack. Two samples have been realized starting from a silicon heterojunction with an aluminum contact on the rear side and depositing the double stack on the front, in a case including the Cu NPs and in another sample without NPs. Then the samples have been annealed at 200 °C for 30 min in N_2 atmosphere. I have measured the *EQE* (Figure 5.3a) and reflectance (Figure 5.3b) from which the *IQE* (Figure 5.3c) has been calculated as in Equation (5.1) (transmittance has been neglected in this case). The data of Figure 5.3 the quantum efficiency gains due to both the thermal annealing and the inclusion of the Cu NPs, with *IQE* values above 80%.

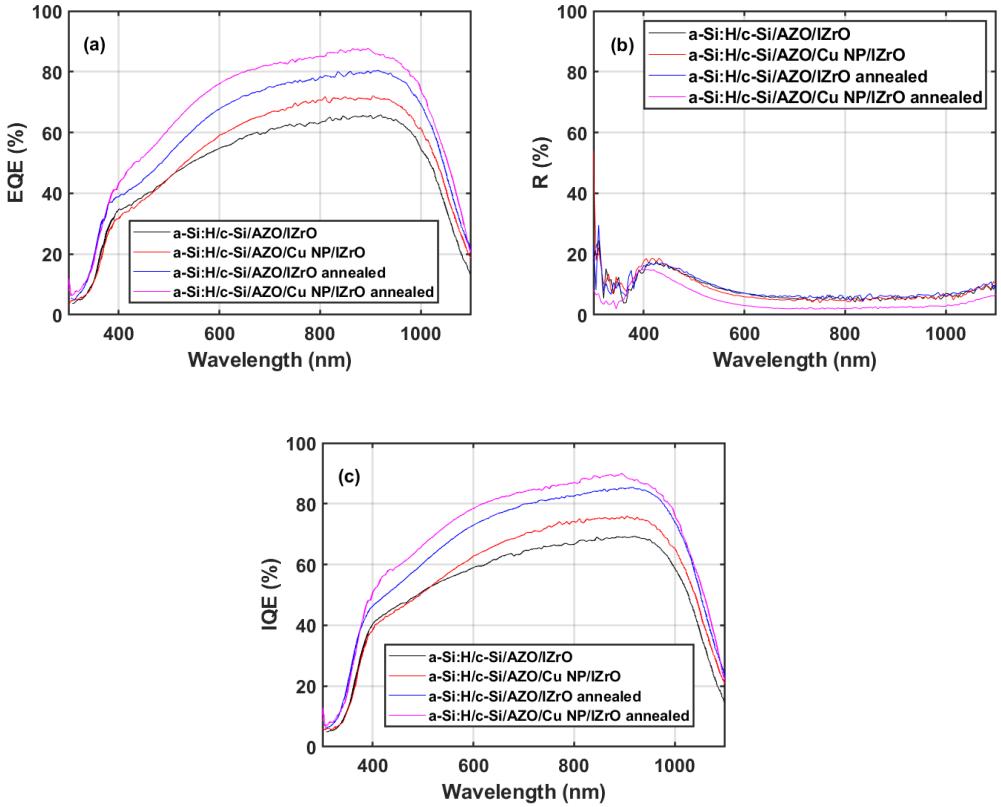

Figure 5.3: *EQE* (a), reflectance (b) and *IQE* (c) of the SHJ sample with the double stack AZO/IZrO with and without Cu NPs and before and after annealing.

Conclusions

In this work, I have illustrated the current challenges of silicon photovoltaics and my research activity for the PhD programme in Physics aimed at studying these problems.
In Chapter 1 I have illustrated the growth of this technology, from its early understanding by Shockley and Queisser to its current industrial maturity producing several successful solutions in terms of cell architecture. I have also showed how diverse research has been in studying new materials and processes, and how sometimes the scientific activity can be tied to the economic and industrial trends, as the polysilicon shortage crisis between 2004 and 2008 has lead researchers to find several new alternatives, some of which are still in active development or have already found success in the market.
In Chapter 2 I have reported on analytical and computational methods commonly used to predict the performance of solar cells, and I have also described a Python script that I have written to perform 3D simulation of textured multi-junction cells. In particular, the model employs optical ray tracing to determine the absorption spectra of each layer in the stack, but introduces an empirical coefficient to condense carrier transport and recombination, thereby reducing the input parameters of the model to the optical constants and state-of-the-art efficiencies of the materials involved. I have applied the model to optimize the top module for several thin-film technologies in a voltage-matched two-terminal system with a bifacial silicon heterojunction bottom module, predicting an efficiency higher than 34% with a 1.85 eV bandgap perovskite with state-of-the-art cells.

In Chapter 3 I have described the challenges in efficiently installing modules on the field. Especially for bifacial modules, optimizing the installation is another task that is suited to computational physics, and I have listed the most common models used to predicts solar irradiance along with its components and module temperature. Then, I have described a model that has been developed and used by our research group: in particular, the model has been designed specifically for bifacial systems, and for this reason the evaluation of the albedo irradiance is performed by a fully-3D sum of contributions from each ground element. The model has been used to investigate several aspects of bifacial installations, from perimeter effects due to uneven shading across a row of modules to the impact of different albedo conditions on the power output of bifacial modules.
In Chapter 4 I have discussed one of the most promising approaches to overcome the efficiency limit of single-junction silicon photovoltaics, that is, the multi-junction modules. In these systems two or more different semiconductors technologies work in tandem to split solar light efficiently, reducing thermalization losses and increasing the energy yield. However, three connection schemes have been designed, each with its own advantages and caveats. I have also reported on a voltage-matched two-terminal system combining bifacial silicon heterojunction and gallium arsenide that has been developed during my research activity, demonstrating that the parallel connection between the two modules is particularly suited to the integration of bifacial modules in multi-junction system, as the voltage match required to optimize the performance can be maintained throughout the day even in vastly different albedo conditions.
Lastly, in Chapter 5 I have reported several activities carried out in collaboration with other research groups aimed at the characterization of new materials for silicon solar cells, with particular emphasis on the passivation and anti-reflection layers in silicon heterojunction solar cells, although these studies are still under active development.
Further improvements are still possible, both for the installation of modules on the field and the development of new technologies. In fact, research projects have already started to develop smart electronics for installed modules, new semiconductor technologies based on innovative materials and improved optical elements for the efficient employment of diffuse light in physically-split multi-junction modules.

Bibliography

[1] William Shockley and Hans J. Queisser. Detailed balance limit of efficiency of p-n junction solar cells. *Journal of Applied Physics*, 32(3):510–519, 06 2004.

[2] M. Wolf. Limitations and possibilities for improvement of photovoltaic solar energy converters: Part i: Considerations for earth's surface operation. *Proceedings of the IRE*, 48(7):1246–1263, 1960.

[3] Martin A. Green. Accuracy of analytical expressions for solar cell fill factors. *Solar Cells*, 7(3):337–340, 1982.

[4] Mohammad I Hossain, Wayesh Qarony, Sainan Ma, Longhui Zeng, Dietmar Knipp, and Yuen Hong Tsang. Perovskite/silicon tandem solar cells: from detailed balance limit calculations to photon management. *Nano-micro letters*, 11:1–24, 2019.

[5] Sven Rühle. Tabulated values of the shockley–queisser limit for single junction solar cells. *Solar Energy*, 130:139–147, 2016.

[6] Jefferey L Gray. *Fundamental Properties of Semiconductors*, page 94–98. Wiley, 2011.

[7] Seth Hubbard. *Recombination*, chapter 2.4, pages 39–46. John Wiley & Sons, Ltd, 2016.

[8] J. Dziewior and W. Schmid. Auger coefficients for highly doped and highly excited silicon. *Applied Physics Letters*, 31(5):346–348, 08 2008.

[9] R.A. Sinton and R.M. Swanson. Recombination in highly injected silicon. *IEEE Transactions on Electron Devices*, 34(6):1380–1389, 1987.

[10] M.A. Green. Limits on the open-circuit voltage and efficiency of silicon solar cells imposed by intrinsic auger processes. *IEEE Transactions on Electron Devices*, 31(5):671–678, 1984.

[11] A. Hangleiter and R. Häcker. Enhancement of band-to-band auger recombination by electron-hole correlations. *Phys. Rev. Lett.*, 65:215–218, Jul 1990.

[12] Pietro P. Altermatt, Jan Schmidt, Gernot Heiser, and Armin G. Aberle. Assessment and parameterisation of coulomb-enhanced auger recombination coefficients in lowly injected crystalline silicon. *Journal of Applied Physics*, 82(10):4938–4944, 11 1997.

[13] Mark J. Kerr and Andres Cuevas. General parameterization of auger recombination in crystalline silicon. *Journal of Applied Physics*, 91(4):2473–2480, 02 2002.

[14] Armin Richter, Stefan W. Glunz, Florian Werner, Jan Schmidt, and Andres Cuevas. Improved quantitative description of auger recombination in crystalline silicon. *Phys. Rev. B*, 86:165202, Oct 2012.

[15] Marc Rüdiger, Johannes Greulich, Armin Richter, and Martin Hermle. Parameterization of free carrier absorption in highly doped silicon for solar cells. *IEEE Transactions on Electron Devices*, 60(7):2156–2163, 2013.

[16] D.K. Schroder, R.N. Thomas, and J.C. Swartz. Free carrier absorption in silicon. *IEEE Journal of Solid-State Circuits*, 13(1):180–187, 1978.

[17] Joerg Isenberg and Wilhelm Warta. Free carrier absorption in heavily doped silicon layers. *Applied Physics Letters*, 84(13):2265–2267, 03 2004.

[18] Armin Richter, Martin Hermle, and Stefan W. Glunz. Reassessment of the limiting efficiency for crystalline silicon solar cells. *IEEE Journal of Photovoltaics*, 3(4):1184–1191, 2013.

[19] Martin A Green. Self-consistent optical parameters of intrinsic silicon at 300 k including temperature coefficients. *Solar Energy Materials and Solar Cells*, 92(11):1305–1310, 2008.

[20] T. Trupke, M. A. Green, P. Würfel, P. P. Altermatt, A. Wang, J. Zhao, and R. Corkish. Temperature dependence of the radiative recombination coefficient of intrinsic crystalline silicon. *Journal of Applied Physics*, 94(8):4930–4937, 09 2003.

[21] Andreas Schenk. Finite-temperature full random-phase approximation model of band gap narrowing for silicon device simulation. *Journal of Applied Physics*, 84(7):3684–3695, 10 1998.

[22] Pietro P. Altermatt, Andreas Schenk, Frank Geelhaar, and Gernot Heiser. Reassessment of the intrinsic carrier density in crystalline silicon in view of band-gap narrowing. *Journal of Applied Physics*, 93(3):1598–1604, 02 2003.

[23] Paul A. Basore. Defining terms for crystalline silicon solar cells. *Progress in Photovoltaics: Research and Applications*, 2(2):177–179, 1994.

[24] Bruno Ceccaroli and Otto Lohne. *Solar Grade Silicon Feedstock*, page 169–217. Wiley, 2011.

[25] GUNNAR ERIKSSON and KLAUS HACK. Production of metallurgical-grade silicon in an electric arc furnace. In K. Hack, editor, *The SGTE Casebook (Second Edition)*, Woodhead Publishing Series in Metals and Surface Engineering, pages 415–424. Woodhead Publishing, second edition edition, 2008.

[26] Kouji Yasuda, Kazuki Morita, and Toru H. Okabe. Processes for production of solar-grade silicon using hydrogen reduction and/or thermal decomposition. *Energy Technology*, 2(2):141–154, 2014.

[27] Shwetank Yadav, Kinnor Chattopadhyay, and Chandra Veer Singh. Solar grade silicon production: A review of kinetic, thermodynamic and fluid dynamics based continuum scale modeling. *Renewable and Sustainable Energy Reviews*, 78:1288–1314, 2017.

[28] Carl L. Yaws, Fred C. Jelen, Ku-Yen Li, P.M. Patel, and C.S. Fang. New technologies for solar energy silicon: Cost analysis of ucc silane process. *Solar Energy*, 22(6):547–553, 1979.

[29] Vasilis Fthenakis and Enrica Leccisi. Updated sustainability status of crystalline silicon-based photovoltaic systems: Life-cycle energy and environmental impact reduction trends. *Progress in Photovoltaics: Research and Applications*, 29(10):1068–1077, 2021.

[30] Hugo Rodriguez, Ismael Guerrero, Wolfgang Koch, Arthur L. Endrös, Dieter Franke, Christian Häßler, Juris P. Kalejs, and H. J. Möller. *Bulk Crystal Growth and Wafering for PV*, page 169–217. Wiley, 2011.

[31] Tatsuo Saga. Advances in crystalline silicon solar cell technology for industrial mass production. *npg asia materials*, 2(3):96–102, 2010.

[32] Robert S. Feigelson. Crystal growth through the ages: A historical perspective. In Tatau Nishinaga, editor, *Handbook of Crystal Growth (Second Edition)*, pages 1–83. Elsevier, Boston, second edition edition, 2015.

[33] Soonwoo Kwon, Jongheop Yi, Sewang Yoon, Joon Sung Lee, and Donghwan Kim. Effects of textured morphology on the short circuit current of single crystalline silicon solar cells: Evaluation of alkaline wet-texture processes. *Current Applied Physics*, 9(6):1310–1314, 2009.

[34] Markus Fischer, Michael Woodhouse, Susanne Herritsch, and Jutta Trube. International technology roadmap for photovoltaic (itrpv). *VDMA EV*, 2021.

[35] Hemant Kumar Raut, V Anand Ganesh, A Sreekumaran Nair, and Seeram Ramakrishna. Anti-reflective coatings: A critical, in-depth review. *Energy & Environmental Science*, 4(10):3779–3804, 2011.

[36] J.G. Fossum. Physical operation of back-surface-field silicon solar cells. *IEEE Transactions on Electron Devices*, 24(4):322–325, 1977.

[37] Abhishek Kumar, Monika Bieri, Thomas Reindl, and Armin G. Aberle. Economic viability analysis of silicon solar cell manufacturing: Al-bsf versus perc. *Energy Procedia*, 130:43–49, 2017. Proceedings of the SNEC 11th International Photovoltaic Power Generation Conference & Exhibition, SNEC 2017 Scientific Conference.

[38] S. R. Wenham and M. A. Green. Silicon solar cells. *Progress in Photovoltaics: Research and Applications*, 4(1):3–33, 1996.

[39] Martin A. Green. The passivated emitter and rear cell (perc): From conception to mass production. *Solar Energy Materials and Solar Cells*, 143:190–197, 2015.

[40] S. Narasinha and A. Rohatgi. Optimized aluminum back surface field techniques for silicon solar cells. In *Conference Record of the Twenty Sixth IEEE Photovoltaic Specialists Conference - 1997*, pages 63–66, 1997.

[41] Savita Kashyap, Jaya Madan, Rahul Pandey, and Rajnish Sharma. Comprehensive study on the recent development of perc solar cell. In *2020 47th IEEE Photovoltaic Specialists Conference (PVSC)*, pages 2542–2546, 2020.

[42] Ki Hyung Kim, Chang Sub Park, Jae Doo Lee, Jong Youb Lim, Je Min Yeon, Il Hwan Kim, Eun Joo Lee, and Young Hyun Cho. Record high efficiency of screen-printed silicon aluminum back surface field solar cell: 20.29 *Japanese Journal of Applied Physics*, 56(8S2):08MB25, jul 2017.

[43] M.A. Green, A.W. Blakers, J. Zhao, A.M. Milne, A. Wang, and X. Dai. Characterization of 23-percent efficient silicon solar cells. *IEEE Transactions on Electron Devices*, 37(2):331–336, 1990.

[44] Thorsten Dullweber and Jan Schmidt. Industrial silicon solar cells applying the passivated emitter and rear cell (perc) concept—a review. *IEEE Journal of Photovoltaics*, 6(5):1366–1381, 2016.

[45] Andrew W. Blakers, Aihua Wang, Adele M. Milne, Jianhua Zhao, and Martin A. Green. 22.8% efficient silicon solar cell. *Applied Physics Letters*, 55(13):1363–1365, 09 1989.

[46] Andrew Blakers. Development of the perc solar cell. *IEEE Journal of Photovoltaics*, 9(3):629–635, 2019.

[47] Guido Agostinelli, J Szlufcick, Patrick Choulat, and Guy Beaucarne. Local contact structures for industrial perc-type solar cells. In *Proceedings of the 20th European Photovoltaic Solar Energy Conference*, pages 942–945, 2005.

[48] Mikio Taguchi. Review—development history of high efficiency silicon heterojunction solar cell: From discovery to practical use. *ECS Journal of Solid State Science and Technology*, 10(2):025002, feb 2021.

[49] J. I. Pankove and M. L. Tarng. Amorphous silicon as a passivant for crystalline silicon. *Applied Physics Letters*, 34(2):156–157, 08 2008.

[50] W. Fuhs, K. Niemann, and J. Stuke. Heterojunctions of amorphous silicon and silicon single crystals. *AIP Conference Proceedings*, 20(1):345–350, 05 1974.

[51] Koji Okuda, Hiroaki Okamoto, and Yoshihiro Hamakawa. Amorphous si/polycrystalline si stacked solar cell having more than 12 *Japanese Journal of Applied Physics*, 22(9A):L605, sep 1983.

[52] MM Rahman and S Furukawa. Amorphous/crystalline heterostructure as a novel approach to fabrication of a solar cell. *Electronics letters*, 20(2):57–58, 1984.

[53] Masayuki Iwamoto, Kouji Minami, and Toshihiko Yamaoki. Photovoltaic device, 1990.

[54] Shigeru Noguchi, Hiroshi Iwata, and Keiichi Sano. Photovoltaic device, 1991.

[55] Cosimo Gerardi. Tecnologie fotovoltaiche innovative per ridurre il costo dell'elettricità. 2020.

[56] Radovan Kopecek, Florian Buchholz, Valentin D. Mihailetchi, Joris Libal, Jan Lossen, Ning Chen, Haifeng Chu, Christoph Peter, Tudor Timofte, Andreas Halm, Yonggang Guo, Xiaoyong Qu, Xiang Wu, Jiaqing Gao, and Peng Dong. Interdigitated back contact technology as final evolution for industrial crystalline single-junction silicon solar cell. *Solar*, 3(1):1–14, 2023.

[57] Arsalan Razzaq, Thomas G. Allen, Wenzhu Liu, Zhengxin Liu, and Stefaan De Wolf. Silicon heterojunction solar cells: Techno-economic assessment and opportunities. *Joule*, 6(3):514–542, 2022.

[58] Frank Feldmann, Martin Bivour, Christian Reichel, Martin Hermle, and Stefan W. Glunz. Passivated rear contacts for high-efficiency n-type si solar cells providing high interface passivation quality and excellent transport characteristics. *Solar Energy Materials and Solar Cells*, 120:270–274, 2014.

[59] F Feldmann, Martin Bivour, Christian Reichel, Martin Hermle, and Stefan W Glunz. A passivated rear contact for high-efficiency n-type silicon solar cells enabling high vocs and ff> 82%. In *28th European PV solar energy conference and exhibition*, 2013.

[60] Dibyendu Kumar Ghosh, Sukanta Bose, Gourab Das, Shiladitya Acharyya, Anupam Nandi, Sumita Mukhopadhyay, and Anindita Sengupta. Fundamentals, present status and future perspective of topcon solar cells: A comprehensive review. *Surfaces and Interfaces*, 30:101917, 2022.

[61] J. Shewchun, R. Singh, and M. A. Green. Theory of metal-insulator-semiconductor solar cells. *Journal of Applied Physics*, 48(2):765–770, 08 2008.

[62] Frank Feldmann, Maik Simon, Martin Bivour, Christian Reichel, Martin Hermle, and Stefan W. Glunz. Efficient carrier-selective p- and n-contacts for si solar cells. *Solar Energy Materials and Solar Cells*, 131:100–104, 2014. SI: SiliconPV 2014.

[63] Ke Tao, Shuai Jiang, Rui Jia, Ying Zhou, Pengfei Zhang, Xiaowan Dai, Hengchao Sun, Zhi Jin, and Xinyu Liu. The impact of indium

tin oxide deposition and post annealing on the passivation property of topcon solar cells. *Solar Energy*, 176:241–247, 2018.

[64] Yuguo Tao, Vijaykumar Upadhyaya, Ying-Yuan Huang, Chia-Wei Chen, Keenan Jones, and Ajeet Rohatgi. Carrier selective tunnel oxide passivated contact enabling 21.4efficient large-area n-type silicon solar cells. In *2016 IEEE 43rd Photovoltaic Specialists Conference (PVSC)*, pages 2531–2535, 2016.

[65] Kunta Yoshikawa, Hayato Kawasaki, Wataru Yoshida, Toru Irie, Katsunori Konishi, Kunihiro Nakano, Toshihiko Uto, Daisuke Adachi, Masanori Kanematsu, Hisashi Uzu, et al. Silicon heterojunction solar cell with interdigitated back contacts for a photoconversion efficiency over 26%. *Nature energy*, 2(5):1–8, 2017.

[66] R.J. Schwartz and M.D. Lammert. Silicon solar cells for high concentration applications. In *1975 International Electron Devices Meeting*, pages 350–352, 1975.

[67] M.D. Lammert and R.J. Schwartz. The interdigitated back contact solar cell: A silicon solar cell for use in concentrated sunlight. *IEEE Transactions on Electron Devices*, 24(4):337–342, 1977.

[68] Qiu Pengcheng and Qiu Pengxiang. Characteristics and development of interdigital back contact solar cells. *IOP Conference Series: Earth and Environmental Science*, 621(1):012067, jan 2021.

[69] Jingjing Liu, Yao Yao, Shaoqing Xiao, and Xiaofeng Gu. Review of status developments of high-efficiency crystalline silicon solar cells. *Journal of Physics D: Applied Physics*, 51(12):123001, feb 2018.

[70] Andrea Ingenito, Olindo Isabella, and Miro Zeman. Simplified process for high efficiency, self-aligned ibc c-si solar cells combining ion implantation and epitaxial growth: Design and fabrication. *Solar Energy Materials and Solar Cells*, 157:354–365, 2016.

[71] Guangtao Yang, Andrea Ingenito, Olindo Isabella, and Miro Zeman. Ibc c-si solar cells based on ion-implanted poly-silicon passivating contacts. *Solar Energy Materials and Solar Cells*, 158:84–90,

2016. Proceedings of the 6th International Conference on Silicon Photovoltaics.

[72] Kunta Yoshikawa, Wataru Yoshida, Toru Irie, Hayato Kawasaki, Katsunori Konishi, Hirotaka Ishibashi, Tsuyoshi Asatani, Daisuke Adachi, Masanori Kanematsu, Hisashi Uzu, and Kenji Yamamoto. Exceeding conversion efficiency of 26% by heterojunction interdigitated back contact solar cell with thin film si technology. *Solar Energy Materials and Solar Cells*, 173:37–42, 2017. Proceedings of the 7th international conference on Crystalline Silicon Photovoltaics.

[73] Vaibhav V. Kuruganti, Daniel Wurmbrand, Thomas Buck, Sven Seren, Miro Zeman, Olindo Isabella, Fabian Geml, Heiko Plagwitz, Barbara Terheiden, and Valentin D. Mihailetchi. Industrially viable diffused ibc solar cells using apcvd dopant glass layers. *Solar Energy Materials and Solar Cells*, 251:112111, 2023.

[74] Joseph J. Wysocki and Paul Rappaport. Effect of temperature on photovoltaic solar energy conversion. *Journal of Applied Physics*, 31(3):571–578, 06 2004.

[75] O. Dupré, R. Vaillon, and M.A. Green. Physics of the temperature coefficients of solar cells. *Solar Energy Materials and Solar Cells*, 140:92–100, 2015.

[76] Y.P. Varshni. Temperature dependence of the energy gap in semiconductors. *Physica*, 34(1):149–154, 1967.

[77] K. P. O'Donnell and X. Chen. Temperature dependence of semiconductor band gaps. *Applied Physics Letters*, 58(25):2924–2926, 06 1991.

[78] S. M. Sze and Kwok Kwok Ng. *Physics and Properties of Semiconductors - A Review*, page 16–27. John Wiley & Sons, Inc., 2007.

[79] Priyanka Singh and N.M. Ravindra. Temperature dependence of solar cell performance — an analysis. *Solar Energy Materials and Solar Cells*, 101:36–45, 2012.

[80] S. M. Sze and Kwok Kwok Ng. *Junctions*. John Wiley & Sons, Inc., 2007.

[81] Martin A. Green. *Efficiency Limits, Losses, and Measurement*. Prentice-Hall, 1982.

[82] Martin A. Green. General temperature dependence of solar cell performance and implications for device modelling. *Progress in Photovoltaics: Research and Applications*, 11(5):333–340, 2003.

[83] Martin A. Green. Radiative efficiency of state-of-the-art photovoltaic cells. *Progress in Photovoltaics: Research and Applications*, 20(4):472–476, 2012.

[84] Takahiro Mishima, Mikio Taguchi, Hitoshi Sakata, and Eiji Maruyama. Development status of high-efficiency hit solar cells. *Solar Energy Materials and Solar Cells*, 95(1):18–21, 2011. 19th International Photovoltaic Science and Engineering Conference and Exhibition (PVSEC-19) Jeju, Korea, 9-13 November 2009.

[85] Xiaodong Li, Yuhao Yang, Shenglei Huang, Kai Jiang, Zhenfei Li, Wenjie Zhao, Jian Yu, Qi Gao, Anjun Han, Jianhua Shi, Junlin Du, Fanying Meng, Liping Zhang, Zhengxin Liu, and Wenzhu Liu. Reassessment of silicon heterojunction cell performance under operating conditions. *Solar Energy Materials and Solar Cells*, 247:111951, 2022.

[86] Anh Huy Tuan Le, Rabin Basnet, Di Yan, Wenhao Chen, Naomi Nandakumar, Shubham Duttagupta, Johannes P. Seif, and Ziv Hameiri. Temperature-dependent performance of silicon solar cells with polysilicon passivating contacts. *Solar Energy Materials and Solar Cells*, 225:111020, 2021.

[87] Simon M.F. Zhang, Johannes P. Seif, Malcolm D. Abbott, Anh Huy Tuan Le, Thomas G. Allen, Ivan Perez-Wurfl, and Ziv Hameiri. Illumination-dependent temperature coefficients of the electrical parameters of modern silicon solar cell architectures. *Nano Energy*, 98:107221, 2022.

[88] Jan Haschke, Johannes P Seif, Yannick Riesen, Andrea Tomasi, Jean Cattin, Loïc Tous, Patrick Choulat, Monica Aleman, Emanuele Cornagliotti, Angel Uruena, et al. The impact of silicon solar cell architecture and cell interconnection on energy yield in hot & sunny climates. *Energy & Environmental Science*, 10(5):1196–1206, 2017.

[89] Simon M. F. Zhang, Johannes P. Seif, Thomas G. Allen, Rabin Basnet, Anh Huy Tuan Le, Ivan Perez-Wurfl, and Ziv Hameiri. Temperature- and illumination-dependent characterization of solar cells using suns-voc(t) and i-v(t). In *2021 IEEE 48th Photovoltaic Specialists Conference (PVSC)*, pages 0737–0740, 2021.

[90] Le Wang, Yi Tang, Shu Zhang, Faze Wang, and Jun Wang. Energy yield analysis of different bifacial pv (photovoltaic) technologies: Topcon, hjt, perc in hainan. *Solar Energy*, 238:258–263, 2022.

[91] Makoto Kasu, Jaffar Abdu, Shigeomi Hara, Sungwoo Choi, Yasuo Chiba, and Atsushi Masuda. Temperature dependence measurements and performance analyses of high-efficiency interdigitated back-contact, passivated emitter and rear cell, and silicon heterojunction photovoltaic modules. *Japanese Journal of Applied Physics*, 57(8S3):08RG18, jul 2018.

[92] He Wang, Xiaoli Cheng, and Hong Yang. Temperature coefficients and operating temperature verification for passivated emitter and rear cell bifacial silicon solar module. *IEEE Journal of Photovoltaics*, 10(3):729–739, 2020.

[93] Xiaoli Cheng, Tianze Zhou, Songshan Feng, He Wang, Hong Yang, Shengchun Mao, and Huacong Yu. Comparative study on temperature coefficients of al-bsf solar cells and perc solar cells. In *2019 IEEE 46th Photovoltaic Specialists Conference (PVSC)*, pages 0304–0307, 2019.

[94] Weiliang Wu, Jie Bao, Limin Ma, Chen Chen, Ronglin Liu, Zhencong Qiao, Jia Chen, and Zhifeng Liu. Development of industrial n-type bifacial topcon solar cells and modules. 10 2019.

[95] Robby Peibst, Felix Haase, Byungsul Min, Christina Hollemann, Till Brendemühl, Karsten Bothe, and Rolf Brendel. On the chances and challenges of combining electron-collecting npolo and hole-collecting al-p+ contacts in highly efficient p-type c-si solar cells. *Progress in Photovoltaics: Research and Applications*, 31(4):327–340, 2023.

[96] Olivier Dupré, Rodolphe Vaillon, and Martin A. Green. *Specificities of the Thermal Behavior of Current and Emerging Photovoltaic Technologies*, page 107–110. SPRINGER, 2018.

[97] Maarten W. M. van Cleef, Francisco A. Rubinelli, Rita Rizzoli, Roberto Pinghini, Ruud E. I. Schropp, and Werner F. van der Weg. Amorphous silicon carbide/crystalline silicon heterojunction solar cells: A comprehensive study of the photocarrier collection. *Japanese Journal of Applied Physics*, 37(7R):3926, jul 1998.

[98] NM Bordina, TM Golovner, VV Zadde, AK Zaitseva, AP Landsman, and VI Streltsova. Operation of a thin silicon photoconverter under illumination on both sides. *Applied solar energy*, 11(5-6):81–86, 1975.

[99] Antonio Luque. Procedimento para obtener celulas solares bifaciales, 1978.

[100] Antonio Luque, JoséM Ruiz, Andrés Cuevas, Javier Eguren, and MG Agost. Double sided/ds/solar cells to improve static concentration. In *Photovoltaic Solar Energy Conference*, pages 269–277, 1978.

[101] Antonio Luque, Andres Cuevas, and Javier Eguren. Solar cell behaviour under variable surface recombination velocity and proposal of a novel structure. *Solid-State Electronics*, 21(5):793–794, 1978.

[102] Antonio Luque. Double-sided solar cell with self-refrigerating concentrator, 1979.

[103] Javier Eguren, J. del Alamo, and Antonio Luque. Optimisation of p+ doping level of n+-p-p+ bifacial b.s.f. solar cells by ion implantation. *Electronics Letters*, 16:633–634, 1980.

[104] A. Cuevas, A. Luque, J. Eguren, and J. Del Alamo. High efficiency bifacial back surface field solar cells. *Solar Cells*, 3(4):337–340, 1981.

[105] Eduardo Lorenzo. On the historical origins of bifacial pv modelling. *Solar Energy*, 218:587–595, 2021.

[106] J. Eguren, F. Martínez-Moreno, P. Merodio, and E. Lorenzo. First bifacial pv modules early 1983. *Solar Energy*, 243:327–335, 2022.

[107] SW Glunz, J Knobloch, D Biro, and W Wettling. Optimized high-efficiency silicon solar cells with jsc= 42 ma/cm^2 and ɲ= 23.3%. In *Proceedings of the 14th European photovoltaic solar energy conference*, pages 392–395, 1997.

[108] C.Z. Zhou, P.J. Verlinden, R.A. Crane, R.M. Swanson, and R.A. Sinton. 21.9% efficient silicon bifacial solar cells. In *Conference Record of the Twenty Sixth IEEE Photovoltaic Specialists Conference - 1997*, pages 287–290, 1997.

[109] T Uematsu, K Tsutsui, Y Yazawa, T Warabisako, I Araki, Y Eguchi, and T Joge. Development of bifacial pv cells for new applications of flat-plate modules. *Solar Energy Materials and Solar Cells*, 75(3):557–566, 2003. PVSEC 12, PART III.

[110] Antonius Burgers. 19% efficient n-type si solar cells made in pilot production. In *25th European Photovoltaic Solar Energy Conference and Exhibition - 5th World Conference on Photovoltaic Energy Conversion*, 09 2010.

[111] I.G. Romijn, B.B. Van Aken, J. Anker, A.R. Burgers, A. Gutjahr, B. Heurtault, M. Koppes, E. Kossen, M. Lamers, D.S. Saynova, C.J.J. Tool, F. Lang, G. Li, H. Wang, Z. Hu, P.R. Venema, and A.H.G. Vlooswijk. Industrial implementation of efficiency improvements in n-type solar cells and modules. *27th European Photovoltaic Solar Energy Conference and Exhibition*, 2012.

[112] Hyunsoo Lim, Seong Hyeon Cho, Jiyeon Moon, Da Yeong Jun, and Sung Hyun Kim. Effects of reflectance of backsheets and spacing between cells on photovoltaic modules. *Applied Sciences*, 12(1), 2022.

[113] Khalid Radouane, A. Plotton, Amy Lindsay, C. Lucas, and Patrick Dupeyrat. Investigations on albedo dependency of bifacial pv yield. In *29th European photovoltaic solar energy conference and exhibition*, 2014.

[114] Tian Shen Liang, Mauro Pravettoni, Chris Deline, Joshua S Stein, Radovan Kopecek, Jai Prakash Singh, Wei Luo, Yan Wang, Armin G Aberle, and Yong Sheng Khoo. A review of crystalline silicon bifacial photovoltaic performance characterisation and simulation. *Energy & Environmental Science*, 12(1):116–148, 2019.

[115] J. Levrat, C. Allebé, N. Badel, L. Barraud, M. Bonnet-Eymard, J. Champliaud, F. Debrot, A. Descoeudres, A. Faes, A. Lachowicz, S. Nicolay, L. Sansonnens, C. Ballif, J. Geissbühler, S. De Wolf, and M. Despeisse. High-performance hetero-junction crystalline silicon photovoltaic technology. In *2014 IEEE 40th Photovoltaic Specialist Conference (PVSC)*, pages 1218–1222, 2014.

[116] Thorsten Dullweber, Christopher Kranz, Robby Peibst, Ulrike Baumann, Helge Hannebauer, Alexander Fülle, Stefan Steckemetz, Torsten Weber, Martin Kutzer, Matthias Müller, Gerd Fischer, Phedon Palinginis, and Holger Neuhaus. Perc+: industrial perc solar cells with rear al grid enabling bifaciality and reduced al paste consumption. *Progress in Photovoltaics: Research and Applications*, 24(12):1487–1498, 2016.

[117] Gautam Raina and Sunanda Sinha. A simulation study to evaluate and compare monofacial vs bifacial perc pv cells and the effect of albedo on bifacial performance. *Materials Today: Proceedings*, 46:5242–5247, 2021. International Conference on Innovations in Clean Energy Technologies (ICET2020).

[118] Meriç Fırat, Hariharsudan Sivaramakrishnan Radhakrishnan, María Recamán Payo, Patrick Choulat, Hussein Badran, Arvid van der Heide, Jonathan Govaerts, Filip Duerinckx, Loic Tous, Ali Hajjiah, and Jef Poortmans. Large-area bifacial n-topcon solar cells with in situ phosphorus-doped lpcvd poly-si passivating contacts. *Solar Energy Materials and Solar Cells*, 236:111544, 2022.

[119] Yifeng Chen, Daming Chen, Chengfa Liu, Zigang Wang, Yang Zou, Yu He, Yao Wang, Ling Yuan, Jian Gong, Wenjie Lin, Xueling Zhang, Yang Yang, Hui Shen, Zhiqiang Feng, Pietro P. Altermatt, and Pierre J. Verlinden. Mass production of industrial tunnel oxide passivated contacts (i-topcon) silicon solar cells with average efficiency over 23% and modules over 345 w. *Progress in Photovoltaics: Research and Applications*, 27(10):827–834, 2019.

[120] Radovan Kopecek, Joris Libal, Jan Lossen, Valentin D. Mihailetchi, Haifeng Chu, Christoph Peter, Florian Buchholz, Eckard Wefringhaus, Andreas Halm, Jikui Ma, Liu Jianda, Guo Yonggang, Qu Xiaoyong, Wu Xiang, and Dong Peng. Zebra technology: low cost bifacial ibc solar cells in mass production with efficiency exceeding 23.5%. In *2020 47th IEEE Photovoltaic Specialists Conference (PVSC)*, pages 1008–1012, 2020.

[121] Cosimo Gerardi, Giuseppe Bengasi, Lorenzo Carbone, Antonio Spampinato, Francesco Rametta, Antonino Ragonesi, Gaetano Izzo, Marcello Sciuto, Marina Foti, and Fabrizio Bizzarri. Innovative pv technologies for reducing electricity costs. *IOP Conference Series: Materials Science and Engineering*, 1265(1):012002, nov 2022.

[122] Gøran Bye and Bruno Ceccaroli. Solar grade silicon: Technology status and industrial trends. *Solar Energy Materials and Solar Cells*, 130:634–646, 2014.

[123] Peter Woditsch and Wolfgang Koch. Solar grade silicon feedstock supply for pv industry. *Solar Energy Materials and Solar Cells*, 72(1):11–26, 2002. EMRS 2001 Symposium E: Crystalline Silicon for Solar Cells.

[124] J. Degoulange, I. Périchaud, C. Trassy, and S. Martinuzzi. Multicrystalline silicon wafers prepared from upgraded metallurgical feedstock. *Solar Energy Materials and Solar Cells*, 92(10):1269–1273, 2008.

[125] Antonio Luque and Steven Hegedus. *Achievements and Challenges of Solar Electricity from Photovoltaics*, page 1–37. Wiley, 2011.

[126] K. L. Chopra, P. D. Paulson, and V. Dutta. Thin-film solar cells: an overview. *Progress in Photovoltaics: Research and Applications*, 12(2-3):69–92, 2004.

[127] J. S. Blakemore. Semiconducting and other major properties of gallium arsenide. *Journal of Applied Physics*, 53(10):R123–R181, 10 1982.

[128] Vesselinka Petrova-Koch, Rudolf Hezel, and Adolf Goetzberger. *High-efficient low-cost photovoltaics: Recent developments*. Springer, 2nd edition, 2020.

[129] SM Bedair, MF Lamorte, and JR Hauser. A two-junction cascade solar-cell structure. *Applied Physics Letters*, 34(1):38–39, 1979.

[130] Martin A. Green, Ewan D. Dunlop, Jochen Hohl-Ebinger, Masahiro Yoshita, Nikos Kopidakis, Karsten Bothe, David Hinken, Michael Rauer, and Xiaojing Hao. Solar cell efficiency tables (version 60). *Progress in Photovoltaics: Research and Applications*, 30(7):687–701, 2022.

[131] Brendan M. Kayes, Hui Nie, Rose Twist, Sylvia G. Spruytte, Frank Reinhardt, Isik C. Kizilyalli, and Gregg S. Higashi. 27.6% conversion efficiency, a new record for single-junction solar cells under 1 sun illumination. In *2011 37th IEEE Photovoltaic Specialists Conference*, pages 000004–000008, 2011.

[132] Owen D. Miller, Eli Yablonovitch, and Sarah R. Kurtz. Strong internal and external luminescence as solar cells approach the shockley–queisser limit. *IEEE Journal of Photovoltaics*, 2(3):303–311, 2012.

[133] Kevin L. Schulte, Steve W. Johnston, Anna K. Braun, Jacob T. Boyer, Anica N. Neumann, William E. McMahon, Michelle Young, Pablo Guimerá Coll, Mariana I. Bertoni, Emily L. Warren, and Myles A. Steiner. Gaas solar cells grown on acoustically spalled gaas substrates with 27*Joule*, 7(7):1529–1542, 2023.

[134] Eric A. Schiff, Steven Hegedus, and Xunming Deng. *Amorphous Silicon-based Solar Cells*, page 487–545. Wiley, 2011.

[135] N. F. Mott, E. A. Davis, and R. A. Street. States in the gap and recombination in amorphous semiconductors. *The Philosophical Magazine: A Journal of Theoretical Experimental and Applied Physics*, 32(5):961–996, 1975.

[136] David Redfield. Energy-band tails and the optical absorption edge; the case of a-si:h. *Solid State Communications*, 44(9):1347–1349, 1982.

[137] David Carlson and C.R. Wronski. Amorphous silicon solar cell. *Applied Physics Letters*, 28:671 – 673, 07 1976.

[138] Cristophe Ballif, Matthieu Despeisse, and Franz-Joseph Haug. *Thin-Film Solar Cells based on Amorphous and Microcrystalline Silicon*, page 139–207. Imperial College Press, 2nd edition, 2015.

[139] D. L. Staebler and C. R. Wronski. Reversible conductivity changes in discharge-produced amorphous si. *Applied Physics Letters*, 31(4):292–294, 08 2008.

[140] J. Meier, R. Flückiger, H. Keppner, and A. Shah. Complete microcrystalline p-i-n solar cell—crystalline or amorphous cell behavior? *Applied Physics Letters*, 65(7):860–862, 08 1994.

[141] Armin G. Aberle. Thin-film solar cells. *Thin Solid Films*, 517(17):4706–4710, 2009. 4th International Conference on Technological Advances of Thin Films and Surface Coatings.

[142] M. Yoshimi, T. Sasaki, T. Sawada, T. Suezaki, T. Meguro, T. Matsuda, K. Santo, K. Wadano, M. Ichikawa, A. Nakajima, and K. Yamamoto. High efficiency thin film silicon hybrid solar cell module on 1 m/sup 2/-class large area substrate. In *3rd World Conference on Photovoltaic Energy Conversion, 2003. Proceedings of*, volume 2, pages 1566–1569 Vol.2, 2003.

[143] Janne Meier, S. Dubail, R. Fluckiger, D. Fischer, Herbert Keppner, and Arvind Shah. Intrinsic microcrystalline silicon (µc-si:h)-a promising new thin film solar cell material. volume 1, pages 409 – 412 vol.1, 01 1995.

[144] T. Matsuyama, N. Terada, T. Baba, T. Sawada, S. Tsuge, K. Wakisaka, and S. Tsuda. High-quality polycrystalline silicon thin film prepared by a solid phase crystallization method. *Journal of Non-Crystalline Solids*, 198-200:940–944, 1996. Amorphous Semiconductors-Science and Technology.

[145] Martin A. Green. Polycrystalline silicon on glass for thin-film solar cells. *Applied Physics A*, 96(1):153–159, jan 2009.

[146] Vitaliy Avrutin, Natalia Izyumskaya, and Hadis Morkoç. Amorphous and micromorph si solar cells: current status and outlook. *Turkish Journal of Physics*, 38(3):526–542, 2014.

[147] C. Becker, D. Amkreutz, T. Sontheimer, V. Preidel, D. Lockau, J. Haschke, L. Jogschies, C. Klimm, J.J. Merkel, P. Plocica, S. Steffens, and B. Rech. Polycrystalline silicon thin-film solar cells: Status and perspectives. *Solar Energy Materials and Solar Cells*, 119:112–123, 2013. Thin-film Photovoltaic Solar Cells.

[148] Shota Minoura, Takuji Maekawa, Keita Kodera, Akihiro Nakane, Shigeru Niki, and Hiroyuki Fujiwara. Optical constants of cu (in, ga) se2 for arbitrary cu and ga compositions. *Journal of Applied Physics*, 117(19), 2015.

[149] William N. Shafarnam, Susanne Siebentritt, and Lars Stolt. *Cu(InGa)Se_2 Solar Cells*, page 546–599. Wiley, 2011.

[150] P. D. Paulson, R. W. Birkmire, and W. N. Shafarman. Optical characterization of cuin$_{1-x}$ga$_x$se$_2$ alloy thin films by spectroscopic ellipsometry. *Journal of Applied Physics*, 94(2):879–888, 06 2003.

[151] M. Elbar and S. Tobbeche. Numerical simulation of cgs/cigs single and tandem thin-film solar cells using the silvaco-atlas software. *Energy Procedia*, 74:1220–1227, 2015. The International Conference on Technologies and Materials for Renewable Energy, Environment and Sustainability –TMREES15.

[152] DS Albin, JJ Carapella, JR Tuttle, and R Noufi. The effect of copper vacancies on the optical bowing of chalcopyrite cu(in,ga)se$_2$ alloys. *MRS Online Proceedings Library (OPL)*, 228, 1991.

[153] Su-Huai Wei and Alex Zunger. Band offsets and optical bowings of chalcopyrites and zn-based ii-vi alloys. *Journal of Applied Physics*, 78(6):3846–3856, 09 1995.

[154] Sigurd Wagner, J. L. Shay, P. Migliorato, and H. M. Kasper. $Cuinse_2$/cds heterojunction photovoltaic detectors. *Applied Physics Letters*, 25(8):434–435, 10 2003.

[155] L. L. Kazmerski, F. R. White, and G. K. Morgan. Thin-film $cuinse_2$/cds heterojunction solar cells. *Applied Physics Letters*, 29(4):268–270, 08 2008.

[156] Reid A. Mickelsen and W.S. Chen. Development of a 9. 4% efficient thin-film $cuinse_2$/cds solar cell. page 800 – 804, 1981. Cited by: 158.

[157] Tokio Nakada, Hiroki Ohbo, Takayuki Watanabe, Hidenobu Nakazawa, Masahiro Matsui, and Akio Kunioka. Improved cu(in,ga)$(s,se)_2$ thin film solar cells by surface sulfurization. *Solar Energy Materials and Solar Cells*, 49(1):285–290, 1997.

[158] Motoshi Nakamura, Koji Yamaguchi, Yoshinori Kimoto, Yusuke Yasaki, Takuya Kato, and Hiroki Sugimoto. Cd-free cu(in,ga)$(se,s)_2$ thin-film solar cell with record efficiency of 23.35%. *IEEE Journal of Photovoltaics*, 9(6):1863–1867, 2019.

[159] Mary D. Archer. *The Past and Present*, pages 1–39. Imperial College Press, 2nd edition, 2015.

[160] Timothy A. Gessert and Dieter Bonnet. *Polycristalline Cadmium Telluride Photovoltaic Devices*, pages 209–244. Imperial College Press, 2nd edition, 2015.

[161] Brian E. McCandless and James R. Sites. *Cadmium Telluride Solar Cells*, page 600–641. Wiley, 2011.

[162] E.W. Justi, G. Schneider, and J. Seredynski. Investigations on cdte thin film solar cells. *Energy Conversion*, 13(2):53–56, 1973.

[163] R.H. Bube, F. Buch, A.L. Fahrenbruch, Y.Y. Ma, and K.W. Mitchell. Photovoltaic energy conversion with n-cds—p-cdte heterojunctions and other ii-vi junctions. *IEEE Transactions on Electron Devices*, 24(4):487–492, 1977.

[164] Alessandro Romeo and Elisa Artegiani. Cdte-based thin film solar cells: Past, present and future. *Energies*, 14(6), 2021.

[165] J. Britt and C. Ferekides. Thin-film cds/cdte solar cell with 15.8% efficiency. *Applied Physics Letters*, 62(22):2851–2852, 05 1993.

[166] Michael A. Scarpulla, Brian McCandless, Adam B. Phillips, Yanfa Yan, Michael J. Heben, Colin Wolden, Gang Xiong, Wyatt K. Metzger, Dan Mao, Dmitry Krasikov, Igor Sankin, Sachit Grover, Amit Munshi, Walajabad Sampath, James R. Sites, Alexandra Bothwell, David Albin, Matthew O. Reese, Alessandro Romeo, Marco Nardone, Robert Klie, J. Michael Walls, Thomas Fiducia, Ali Abbas, and Sarah M. Hayes. Cdte-based thin film photovoltaics: Recent advances, current challenges and future prospects. *Solar Energy Materials and Solar Cells*, 255:112289, 2023.

[167] Naba R. Paudel and Yanfa Yan. Enhancing the photo-currents of cdte thin-film solar cells in both short and long wavelength regions. *Applied Physics Letters*, 105(18):183510, 11 2014.

[168] Brian O'regan and Michael Grätzel. A low-cost, high-efficiency solar cell based on dye-sensitized colloidal tio_2 films. *nature*, 353(6346):737–740, 1991.

[169] Michael A. Grätzel and James R. Durrant. *Dye- and Perovskite-sensitised Mesoscopic Solar Cells*, pages 413–452. Imperial College Press, 2nd edition, 2015.

[170] Jean Desilvestro, Michael Graetzel, Ladislav Kavan, Jacques Moser, and Jan Augustynski. Highly efficient sensitization of titanium dioxide. *Journal of the American Chemical Society*, 107(10):2988–2990, 1985.

[171] Dan Zhang, Marko Stojanovic, Yameng Ren, Yiming Cao, Felix T Eickemeyer, Etienne Socie, Nick Vlachopoulos, Jacques-E Moser, Shaik M Zakeeruddin, Anders Hagfeldt, et al. A molecular photosensitizer achieves a v oc of 1.24 v enabling highly efficient and stable dye-sensitized solar cells with copper (ii/i)-based electrolyte. *Nature communications*, 12(1):1777, 2021.

[172] Kenji Kakiage, Yohei Aoyama, Toru Yano, Keiji Oya, Jun-ichi Fujisawa, and Minoru Hanaya. Highly-efficient dye-sensitized solar cells with collaborative sensitization by silyl-anchor and carboxy-anchor dyes. *Chemical communications*, 51(88):15894–15897, 2015.

[173] Chiara Liliana Boldrini, Norberto Manfredi, Filippo Maria Perna, Vito Capriati, and Alessandro Abbotto. Designing eco-sustainable dye-sensitized solar cells by the use of a menthol-based hydrophobic eutectic solvent as an effective electrolyte medium. *Chemistry – A European Journal*, 24(67):17656–17659, 2018.

[174] Helen Dick Megaw. Crystal structure of barium titanate. *Nature*, 155(3938):484–485, 04 1945.

[175] Akihiro Kojima, Kenjiro Teshima, Yasuo Shirai, and Tsutomu Miyasaka. Organometal halide perovskites as visible-light sensitizers for photovoltaic cells. *Journal of the American Chemical Society*, 131(17):6050–6051, 2009. PMID: 19366264.

[176] Guangda Niu, Xudong Guo, and Liduo Wang. Review of recent progress in chemical stability of perovskite solar cells. *Journal of Materials Chemistry A*, 3(17):8970–8980, 2015.

[177] Jeong-Hyeok Im, Chang-Ryul Lee, Jin-Wook Lee, Sang-Won Park, and Nam-Gyu Park. 6.5% efficient perovskite quantum-dot-sensitized solar cell. *Nanoscale*, 3:4088–93, 09 2011.

[178] Michael M. Lee, Joël Teuscher, Tsutomu Miyasaka, Takurou N. Murakami, and Henry J. Snaith. Efficient hybrid solar cells based on meso-superstructured organometal halide perovskites. *Science*, 338(6107):643–647, 2012.

[179] Michael Saliba, Kwan Wee Tan, Hiroaki Sai, David T. Moore, Trent Scott, Wei Zhang, Lara A. Estroff, Ulrich Wiesner, and Henry J. Snaith. Influence of thermal processing protocol upon the crystallization and photovoltaic performance of organic–inorganic lead trihalide perovskites. *The Journal of Physical Chemistry C*, 118(30):17171–17177, 2014.

[180] Giles E. Eperon, Victor M. Burlakov, Pablo Docampo, Alain Goriely, and Henry J. Snaith. Morphological control for high performance, solution-processed planar heterojunction perovskite solar cells. *Advanced Functional Materials*, 24(1):151–157, 2014.

[181] Mingyu Jeong, In Woo Choi, Eun Min Go, Yongjoon Cho, Minjin Kim, Byongkyu Lee, Seonghun Jeong, Yimhyun Jo, Hye Won Choi, Jiyun Lee, Jin-Hyuk Bae, Sang Kyu Kwak, Dong Suk Kim, and Changduk Yang. Stable perovskite solar cells with efficiency exceeding 24.8% and 0.3-v voltage loss. *Science*, 369(6511):1615–1620, 2020.

[182] Xin Yu Chin, Deniz Turkay, Julian A. Steele, Saba Tabean, Santhana Eswara, Mounir Mensi, Peter Fiala, Christian M. Wolff, Adriana Paracchino, Kerem Artuk, Daniel Jacobs, Quentin Guesnay, Florent Sahli, Gaëlle Andreatta, Mathieu Boccard, Quentin Jeangros, and Christophe Ballif. Interface passivation for 31.25%-efficient perovskite/silicon tandem solar cells. *Science*, 381(6653):59–63, 2023.

[183] Mohammed Istafaul Haque Ansari, Ahsanulhaq Qurashi, and Mohammad Khaja Nazeeruddin. Frontiers, opportunities, and challenges in perovskite solar cells: A critical review. *Journal of Photochemistry and Photobiology C: Photochemistry Reviews*, 35:1–24, 2018.

[184] Jian Gong, Seth B Darling, and Fengqi You. Perovskite photovoltaics: life-cycle assessment of energy and environmental impacts. *Energy & Environmental Science*, 8(7):1953–1968, 2015.

[185] Priyanka Roy, Aritra Ghosh, Fraser Barclay, Ayush Khare, and Erdem Cuce. Perovskite solar cells: A review of the recent advances. *Coatings*, 12(8), 2022.

[186] Giorgio Schileo and Giulia Grancini. Lead or no lead? availability, toxicity, sustainability and environmental impact of lead-free perovskite solar cells. *Journal of materials chemistry C*, 9(1):67–76, 2021.

[187] Bahaa EA Saleh and Malvin Carl Teich. *Fundamentals of photonics*. John Wiley & sons, 2019.

[188] Eugene Hecht. *The Propagation of Light*, page 96–158. Pearson, 5th edition, 2016.

[189] Armin Richter, Martin Hermle, and Stefan W Glunz. Reassessment of the limiting efficiency for crystalline silicon solar cells. *IEEE journal of photovoltaics*, 3(4):1184–1191, 2013.

[190] Zhengshan Jason Yu, Mehdi Leilaeioun, and Zachary Holman. Selecting tandem partners for silicon solar cells. *Nature Energy*, 1(11):1–4, 2016.

[191] PA Basore. Photovoltaic device analysis on personal computers. In *American Soc. for Engineering Education Annual Conf.*, pages 848–853, 1986.

[192] Paul A Basore, DT Rover, and AW Smith. Pc-1d version 2: Enhanced numerical solar cell modelling. In *Conference record of the twentieth IEEE photovoltaic specialists conference*, pages 389–396. IEEE, 1996.

[193] Paul A Basore and Kirsten Cabanas-Holmen. Pc2d: A circular-reference spreadsheet solar cell device simulator. *IEEE Journal of Photovoltaics*, 1(1):72–77, 2011.

[194] Paul A Basore. Efficient computation of multidimensional lambertian optical absorption. *IEEE Journal of Photovoltaics*, 9(1):106–111, 2018.

[195] Marc Burgelman, Peter Nollet, and Stefaan Degrave. Modelling polycrystalline semiconductor solar cells. *Thin solid films*, 361:527–532, 2000.

[196] Johan Verschraegen and Marc Burgelman. Numerical modeling of intra-band tunneling for heterojunction solar cells in scaps. *Thin Solid Films*, 515(15):6276–6279, 2007.

[197] Marc Burgelman and Jonas Marlein. Analysis of graded band gap solar cells with scaps. In *Proceedings of the 23rd European Photovoltaic Solar Energy Conference, Valencia*, pages 2151–2155, 2008.

[198] Koen Decock, Samira Khelifi, and Marc Burgelman. Modelling multivalent defects in thin film solar cells. *Thin Solid Films*, 519(21):7481–7484, 2011.

[199] Koen Decock, Paweł Zabierowski, and Marc Burgelman. Modeling metastabilities in chalcopyrite-based thin film solar cells. *Journal of Applied Physics*, 111(4), 2012.

[200] S Eidelloth, U Eitner, S Steingrube, and R Brendel. Open source graphical user interface in matlab for two-dimensional simulations solving the fully coupled semiconductor equations using comsol. *Proc. 25th EU PVSEC*, pages 2477–2485, 2010.

[201] Yiming Liu, Yun Sun, and Angus Rockett. A new simulation software of solar cells—wxamps. *Solar Energy Materials and Solar Cells*, 98:124–128, 2012.

[202] Andreas Fell. A free and fast three-dimensional/two-dimensional solar cell simulator featuring conductive boundary and quasi-neutrality approximations. *IEEE Transactions on Electron Devices*, 60(2):733–738, 2012.

[203] N Boukortt, S Patanè, and B Hadri. Development of high-efficiency perc solar cells using atlas silvaco. *Silicon*, 11:145–152, 2019.

[204] M Elbar and S Tobbeche. Numerical simulation of cgs/cigs single and tandem thin-film solar cells using the silvaco-atlas software. *Energy Procedia*, 74:1220–1227, 2015.

[205] Sherif Michael and Andrew Bates. The design and optimization of advanced multijunction solar cells using the silvaco atlas software package. *Solar energy materials and solar cells*, 87(1-4):785–794, 2005.

[206] Roberto Corso, Marco Leonardi, Rachela G Milazzo, Andrea Scuto, Stefania MS Privitera, Marina Foti, Cosimo Gerardi, and Salvatore A Lombardo. Evaluation of voltage-matched 2t multi-junction modules based on monte carlo ray tracing. *Energies*, 16(11):4292, 2023.

[207] Hideki Maezawa and Hiroshi Miyauchi. Rigorous expressions for the fresnel equations at interfaces between absorbing media. *JOSA A*, 26(2):330–336, 2009.

[208] Francis X Canning. Corrected fresnel coefficients for lossy materials. In *2011 IEEE International Symposium on Antennas and Propagation (APSURSI)*, pages 2123–2126. IEEE, 2011.

[209] Francis X Canning. On fresnel coefficients for transmission into a lossy medium. In *2015 International Conference on Electromagnetics in Advanced Applications (ICEAA)*, pages 165–168. IEEE, 2015.

[210] Kotaro Kawajiri, Kiyotaka Tahara, and Shigeyuki Uemiya. Lifecycle assessment of critical material substitution: Indium tin oxide and aluminum zinc oxide in transparent electrodes. *Resources, Environment and Sustainability*, 7:100047, 2022.

[211] Stephanie Essig, Christophe Allebé, Timothy Remo, John F Geisz, Myles A Steiner, Kelsey Horowitz, Loris Barraud, J Scott Ward, Manuel Schnabel, Antoine Descoeudres, et al. Raising the one-sun conversion efficiency of iii–v/si solar cells to 32.8% for two junctions and 35.9% for three junctions. *Nature Energy*, 2(9):1–9, 2017.

[212] Patricia SC Schulze, Alexander J Bett, Martin Bivour, Pietro Caprioglio, Fabian M Gerspacher, Özde Ş Kabaklı, Armin Richter, Martin Stolterfoht, Qinxin Zhang, Dieter Neher, et al. 25.1% high-efficiency monolithic perovskite silicon tandem solar cell with a high bandgap perovskite absorber. *Solar RRL*, 4(7):2000152, 2020.

[213] Yukinori Nishigaki, Takayuki Nagai, Mitsutoshi Nishiwaki, Takuma Aizawa, Masayuki Kozawa, Kota Hanzawa, Yoshitsune

Kato, Hitoshi Sai, Hidenori Hiramatsu, Hideo Hosono, et al. Extraordinary strong band-edge absorption in distorted chalcogenide perovskites. *Solar Rrl*, 4(5):1900555, 2020.

[214] Konstantinos Papatryfonos, Todora Angelova, Antoine Brimont, Barry Reid, Stefan Guldin, Peter Raymond Smith, Mingchu Tang, Keshuang Li, Alwyn J Seeds, Huiyun Liu, et al. Refractive indices of mbe-grown alxga (1- x) as ternary alloys in the transparent wavelength region. *AIP Advances*, 11(2), 2021.

[215] RE Treharne, A Seymour-Pierce, K Durose, K Hutchings, S Roncallo, and D Lane. Optical design and fabrication of fully sputtered cdte/cds solar cells. In *Journal of Physics: Conference Series*, volume 286, page 012038. IOP Publishing, 2011.

[216] Jung Woo Leem and Jae Su Yu. Influence of oblique-angle sputtered transparent conducting oxides on performance of si-based thin film solar cells. *physica status solidi (a)*, 208(9):2220–2225, 2011.

[217] Zheng Fang, Zhilong Xu, Tao Jang, Fei Zhou, and Shixiang Huang. Standard deviation quantitative characterization and process optimization of the pyramidal texture of monocrystalline silicon cells. *Materials*, 13(3), 2020.

[218] Suprava Chakraborty, Avinash Kumar Haldkar, and Nallapaneni Manoj Kumar. Analysis of the hail impacts on the performance of commercially available photovoltaic modules of varying front glass thickness. *Renewable Energy*, 203:345–356, 2023.

[219] Mengjie Li, Nafis Iqbal, Zhihao Yang, Xuli Lin, Nicole Karam Pannaci, Christian Avalos, Thomas Shaw, Titel Jurca, and Kristopher Davis. A comprehensive evaluation of contact recombination and contact resistivity losses in industrial silicon solar cells. *IEEE Journal of Photovoltaics*, 10(5):1277–1282, 2020.

[220] Nils Reiners and Ulf Blieske. Smarti-an open source matlab ray tracing tool for solar cell and module optics. In *2018 7th International Energy and Sustainability Conference (IESC)*, pages 1–6. IEEE, 2018.

[221] Bram Greve. Reflections and refractions in ray tracing. 12 2006.

[222] A.H. Reshak, M.M. Shahimin, S. Shaari, and N. Johan. Surface modification via wet chemical etching of single-crystalline silicon for photovoltaic application. *Progress in Biophysics and Molecular Biology*, 113(2):327–332, 2013.

[223] Oliver Höhn, Nico Tucher, and Benedikt Bläsi. Theoretical study of pyramid sizes and scattering effects in silicon photovoltaic module stacks. *Optics express*, 26(6):A320–A330, 2018.

[224] Farjana Akter Jhuma, Marshia Zaman Shaily, and Mohammad Junaebur Rashid. Towards high-efficiency czts solar cell through buffer layer optimization. *Materials for Renewable and Sustainable Energy*, 8:1–7, 2019.

[225] Sinan Yaşar, Süleyman Kahraman, Samed Çetinkaya, Ş Apaydın, İsmail Bilican, and İhsan Uluer. Numerical thickness optimization study of cigs based solar cells with wxamps. *Optik*, 127(20):8827–8835, 2016.

[226] M. Canino, V. Boldrini, R. Rizzoli, E. Centurioni, A. Maurizi, S. Lombardo, A. Terrasi, and C. Summonte. Tco optimization of c-si heterojunction solar cells for tandem architecture by optical simulation. WIP, 2021.

[227] Zhaosheng Hu, Zhenhua Lin, Jie Su, Jincheng Zhang, Jingjing Chang, and Yue Hao. A review on energy band-gap engineering for perovskite photovoltaics. *Solar Rrl*, 3(12):1900304, 2019.

[228] Valerio Lucarini, Jarkko J Saarinen, Kai-Erik Peiponen, and Erik M Vartiainen. *Kramers-Kronig relations in optical materials research*, volume 110. Springer Science & Business Media, 2005.

[229] Zhengshan Jason Yu, Mehdi Leilaeioun, and Zachary Holman. Selecting tandem partners for silicon solar cells. *Nature Energy*, 1(11):1–4, 2016.

[230] Seyed Abbas Mousavi Maleki, H Hizam, and Chandima Gomes. Estimation of hourly, daily and monthly global solar radiation on inclined surfaces: Models re-visited. *Energies*, 10(1):134, 2017.

[231] R. M. Milne. Note on the equation of time. *The Mathematical Gazette*, 10(155):372–375, 1921.

[232] L.T. Wong and W.K. Chow. Solar radiation model. *Applied Energy*, 69(3):191–224, 2001.

[233] MA Machler and M Iqbal. A modification of the ashrae clear sky irradiation model. *ASHRAE transactions*, 91(1):106–115, 1985.

[234] GV Parishwad, RK Bhardwaj, and VK Nema. Estimation of hourly solar radiation for india. *Renewable Energy*, 12(3):303–313, 1997.

[235] Wanxiang Yao, Chunfeng Xu, Jun Zhao, Xiao Wang, Yan Wang, Xianli Li, and Jingfu Cao. The modified ashrae model based on the mechanism of multi-parameter coupling. *Energy Conversion and Management*, 209:112642, 2020.

[236] Samer Alsadi and Yasser Nassar. Correction of the ashrae clear-sky model parameters based on solar radiation measurements in the arabic countries. *International Journal of Renewable Energy Technology Research*, 5:1–16, 07 2016.

[237] Mohamed Abouhashish. Applicability of ashrae clear-sky model based on solar-radiation measurements in saudi arabia. In *AIP Conference Proceedings*, volume 1850. AIP Publishing, 2017.

[238] N Nijegorodov. Improved ashrae model to predict hourly and daily solar radiation components in botswana, namibia, and zimbabwe. *Renewable energy*, 9(1-4):1270–1273, 1996.

[239] Christian Gueymard. Critical analysis and performance assessment of clear sky solar irradiance models using theoretical and measured data. *Solar Energy*, 51(2):121–138, 1993.

[240] Benjamin YH Liu and Richard C Jordan. The interrelationship and characteristic distribution of direct, diffuse and total solar radiation. *Solar energy*, 4(3):1–19, 1960.

[241] DG Erbs, SA Klein, and JA Duffie. Estimation of the diffuse radiation fraction for hourly, daily and monthly-average global radiation. *Solar energy*, 28(4):293–302, 1982.

[242] JF Orgill and KGT Hollands. Correlation equation for hourly diffuse radiation on a horizontal surface. *Solar energy*, 19(4):357–359, 1977.

[243] ABJARKH De Miguel, J Bilbao, R Aguiar, H Kambezidis, and E Negro. Diffuse solar irradiation model evaluation in the north mediterranean belt area. *Solar energy*, 70(2):143–153, 2001.

[244] CP Jacovides, FS Tymvios, VD Assimakopoulos, and NA Kaltsounides. Comparative study of various correlations in estimating hourly diffuse fraction of global solar radiation. *Renewable energy*, 31(15):2492–2504, 2006.

[245] A Louche, G Notton, P Poggi, and G Simonnot. Correlations for direct normal and global horizontal irradiation on a french mediterranean site. *Solar Energy*, 46(4):261–266, 1991.

[246] S Karatasou, M Santamouris, and V Geros. Analysis of experimental data on diffuse solar radiation in athens, greece, for building applications. *International journal of sustainable energy*, 23(1-2):1–11, 2003.

[247] Jacyra Soares, Amauri P Oliveira, Marija Zlata Božnar, Primož Mlakar, Joao F Escobedo, and Antonio J Machado. Modeling hourly diffuse solar-radiation in the city of são paulo using a neural-network technique. *Applied energy*, 79(2):201–214, 2004.

[248] Amauri P Oliveira, João F Escobedo, Antonio J Machado, and Jacyra Soares. Correlation models of diffuse solar-radiation applied to the city of sao paulo, brazil. *Applied Energy*, 71(1):59–73, 2002.

[249] John Boland, Lynne Scott, and Mark Luther. Modelling the diffuse fraction of global solar radiation on a horizontal surface. *Environmetrics: The official journal of the International Environmetrics Society*, 12(2):103–116, 2001.

[250] JW Spencer. A comparison of methods for estimating hourly diffuse solar radiation from global solar radiation. *Solar Energy*, 29(1):19–32, 1982.

[251] Joseph C Lam and Danny HW Li. Correlation between global solar radiation and its direct and diffuse components. *Building and environment*, 31(6):527–535, 1996.

[252] J Chandrasekaran and S Kumar. Hourly diffuse fraction correlation at a tropical location. *Solar Energy*, 53(6):505–510, 1994.

[253] Eduardo Pigueiras. *Energy Collected and Delivered by PV Modules*, pages 905 – 970. 01 2005.

[254] B Liu and R Jordan. Daily insolation on surfaces tilted towards equator. *ASHRAE J.;(United States)*, 10, 1961.

[255] Pericles S Koronakis. On the choice of the angle of tilt for south facing solar collectors in the athens basin area. *Solar Energy*, 36(3):217–225, 1986.

[256] YQ Tian, RJ Davies-Colley, P Gong, and BW Thorrold. Estimating solar radiation on slopes of arbitrary aspect. *Agricultural and Forest Meteorology*, 109(1):67–74, 2001.

[257] V Badescu. 3d isotropic approximation for solar diffuse irradiance on tilted surfaces. *Renewable energy*, 26(2):221–233, 2002.

[258] Richard Perez, Pierre Ineichen, Robert Seals, Joseph Michalsky, and Ronald Stewart. Modeling daylight availability and irradiance components from direct and global irradiance. *Solar energy*, 44(5):271–289, 1990.

[259] Richard Perez, Ronald Stewart, Robert Seals, and Ted Guertin. The development and verification of the perez diffuse radiation model. Technical report, Sandia National Lab.(SNL-NM), Albuquerque, NM (United States); State Univ. . . , 1988.

[260] Richard Perez, Robert Seals, Pierre Ineichen, Ronald Stewart, and David Menicucci. A new simplified version of the perez diffuse irradiance model for tilted surfaces. *Solar energy*, 39(3):221–231, 1987.

[261] Ígor Rapp-Arrarás and Juan M. Domingo-Santos. Functional forms for approximating the relative optical air mass. *Journal of Geophysical Research: Atmospheres*, 116(D24), 2011.

[262] Fritz Kasten. A new table and approximation formula for the relative optial air mass. *Archiv für Meteorologie, Geophysik und Bioklimatologie, Serie B*, 14:206–223, 1965.

[263] Aden B Meinel and Marjorie P Meinel. Applied solar energy: an introduction. *NASA STI/Recon Technical Report A*, 77:33445, 1977.

[264] Dirk C Jordan, Sarah R Kurtz, Kaitlyn VanSant, and Jeff Newmiller. Compendium of photovoltaic degradation rates. *Progress in Photovoltaics: Research and Applications*, 24(7):978–989, 2016.

[265] Cornelia Peike, Ingrid Hädrich, Karl-Anders Weiß, Ines Dürr, and F Ise. Overview of pv module encapsulation materials. *Photovoltaics International*, 19:85–92, 2013.

[266] Claudia Buerhop-Lutz, Oleksandr Stroyuk, Tobias Pickel, Thilo Winkler, Jens Hauch, and Ian Marius Peters. Pv modules and their backsheets - a case study of a multi-mw pv power station. *Solar Energy Materials and Solar Cells*, 231:111295, 2021.

[267] Michel Mattei, Gilles Notton, Christian Cristofari, Marc Muselli, and Philippe Poggi. Calculation of the polycrystalline pv module temperature using a simple method of energy balance. *Renewable energy*, 31(4):553–567, 2006.

[268] BJ Huang, PE Yang, YP Lin, BY Lin, HJ Chen, RC Lai, and JS Cheng. Solar cell junction temperature measurement of pv module. *Solar Energy*, 85(2):388–392, 2011.

[269] Joseph Kuitche, Jaewon Oh, Alfred Brunger, Takamitsu Inoue, Matthew Muller, Christian Bauerdick, Joerg Althaus, Stefan Kiehn, Victor Feng, Ulrike Therhaag, and Robert Struwe. One year noct round-robin testing per iec 61215 standard. In *2011 37th IEEE Photovoltaic Specialists Conference*, pages 002380–002385, 2011.

[270] I Santiago, D Trillo-Montero, IM Moreno-Garcia, V Pallarés-López, and JJ Luna-Rodríguez. Modeling of photovoltaic cell temperature losses: A review and a practice case in south spain. *Renewable and Sustainable Energy Reviews*, 90:70–89, 2018.

[271] Leticia de Oliveira Santos, Paulo Cesar Marques de Carvalho, and Clodoaldo de Oliveira Carvalho Filho. Photovoltaic cell operating temperature models: a review of correlations and parameters. *IEEE Journal of Photovoltaics*, 12(1):179–190, 2021.

[272] R.G. Ross. Flat-plate photovoltaic array design optimization. pages 1126–1132, San Diego, CA, 1980.
.

[273] Vat Sun, Attakorn Asanakham, Thoranis Deethayat, and Tanongkiat Kiatsiriroat. A new method for evaluating nominal operating cell temperature (noct) of unglazed photovoltaic thermal module. *Energy Reports*, 6:1029–1042, 2020.

[274] David Faiman. Assessing the outdoor operating temperature of photovoltaic modules. *Progress in Photovoltaics: Research and Applications*, 16(4):307–315, 2008.

[275] PVsyst Cell Temperature Model — pvpmc.sandia.gov. `https://pvpmc.sandia.gov/modeling-steps/2-dc-module-iv/cell-temperature/pvsyst-cell-temperature-model/`. [Accessed 09-08-2023].

[276] Zheng Ren, Sebastien Jacques, Sébastien Bissey, A. Caldeira, A. Schellmanns, and N. Cézac. Pvlab: an innovative and flexible

simulation tool to better size photovoltaic units. *Renewable Energy and Power Quality Journal*, pages 87–91, 04 2014.

[277] David L King, Jay A Kratochvil, and William Earl Boyson. *Photovoltaic array performance model*, volume 8. Citeseer, 2004.

[278] Pierre Ineichen, Olivier Guisan, and Richard Perez. Ground-reflected radiation and albedo. *Solar Energy*, 44(4):207–214, 1990.

[279] Wenbo Gu, Tao Ma, Meng Li, Lu Shen, and Yijie Zhang. A coupled optical-electrical-thermal model of the bifacial photovoltaic module. *Applied Energy*, 258:114075, 2020.

[280] Ufuk Alper Yusufoglu, Tae Hun Lee, Tobias Markus Pletzer, Andreas Halm, Lejo Joseph Koduvelikulathu, Corrado Comparotto, Radovan Kopecek, and Heinrich Kurz. Simulation of energy production by bifacial modules with revision of ground reflection. *Energy Procedia*, 55:389–395, 2014.

[281] Xingshu Sun, Mohammad Ryyan Khan, Chris Deline, and Muhammad Ashraful Alam. Optimization and performance of bifacial solar modules: A global perspective. *Applied energy*, 212:1601–1610, 2018.

[282] Bill Marion, Sara MacAlpine, Chris Deline, Amir Asgharzadeh, Fatima Toor, Daniel Riley, Joshua Stein, and Clifford Hansen. A practical irradiance model for bifacial pv modules. In *2017 IEEE 44th Photovoltaic Specialist Conference (PVSC)*, pages 1537–1542. IEEE, 2017.

[283] Yunus A. Çengel. *Radiation Heat Transfer*. McGraw-Hill, 2003.

[284] Ufuk A Yusufoglu, Tobias M Pletzer, Lejo Joseph Koduvelikulathu, Corrado Comparotto, Radovan Kopecek, and Heinrich Kurz. Analysis of the annual performance of bifacial modules and optimization methods. *IEEE Journal of Photovoltaics*, 5(1):320–328, 2014.

[285] Ismail Shoukry, Joris Libal, Radovan Kopecek, Eckard Wefringhaus, and Jürgen Werner. Modelling of bifacial gain for stand-alone and in-field installed bifacial pv modules. *Energy Procedia*, 92:600–608, 2016.

[286] M. Lamers, Ebrar Ozkalay, R.S.R. Gali, Gaby Janssen, A.W. Weeber, I.G. Romijn, and Bas Van Aken. Temperature effects of bifacial modules: Hotter or cooler? *Solar Energy Materials and Solar Cells*, 185:192–197, 05 2018.

[287] S.M.S. Privitera, M. Muller, W. Zwaygardt, M. Carmo, R. Milazzo, Pier Enrico Zani, Marco Leonardi, Francesco Maita, Andrea Canino, Marina Foti, Fabrizio Bizzarri, Cosimo Gerardi, and Salvatore Lombardo. Highly efficient solar hydrogen production through the use of bifacial photovoltaics and membrane electrolysis. *Journal of Power Sources*, 473:228619, 10 2020.

[288] Fabio Ricco Galluzzo, Andrea Canino, Cosimo Gerardi, and Salvatore A. Lombardo. A new model for predicting bifacial pv modules performance: first validation results. In *2019 IEEE 46th Photovoltaic Specialists Conference (PVSC)*, pages 1293–1297, 2019.

[289] Fabio Ricco Galluzzo, Pier Enrico Zani, Marina Foti, Andrea Canino, Cosimo Gerardi, and Salvatore Lombardo. Numerical modeling of bifacial pv string performance: Perimeter effect and influence of uniaxial solar trackers. *Energies*, 13(4), 2020.

[290] Isaac Todhunter. *Area of a spherical triangle. Spherical excess.* Macmillan, 1878.

[291] Marco Leonardi, Roberto Corso, Rachela G. Milazzo, Carmelo Connelli, Marina Foti, Cosimo Gerardi, Fabrizio Bizzarri, Stefania M. S. Privitera, and Salvatore A. Lombardo. The effects of module temperature on the energy yield of bifacial photovoltaics: Data and model. *Energies*, 15(1), 2022.

[292] Roberto Corso, Marco Leonardi, Andrea Scuto, Gabriella Milazzo, Marina Foti, Cosimo Gerardi, Fabrizio Bizzarri, Stefania M. S. Privitera, and Salvatore A. Lombardo. Three-dimensional model of bifacial photovoltaic systems, experimental validation, and evaluation of temperature, albedo and perimeter effects. In *XXII CONGRESSO NAZIONALE CIRIAF - Sviluppo Sostenibile, Tutela dell'Ambiente e della Salute Umana - Atti*, pages 318–323, 2022.

[293] Marco Leonardi, Roberto Corso, Andrea Scuto, Gabriella Milazzo, Carmelo Connelli, Marina Foti, Cosimo Gerardi, Fabrizio Bizzarri, Stefania M. S. Privitera, and Salvatore A. Lombardo. Effects of solar spectrum and albedo on the performance of bifacial si heterojunction mini-modules. In *2022 IEEE 49th Photovoltaics Specialists Conference (PVSC)*, pages 0567–0569, 2022.

[294] Chris Gueymard. Daily spectral effects on concentrating pv solar cells as affected by realistic aerosol optical depth and other atmospheric conditions. volume 7410, 08 2009.

[295] Roberto Corso, Fabio Matera, and Salvatore A. Lombardo. Numerical evaluation of optimal tilt angle for energy production and minimum shadowing for bifacial solar modules. In *2023 IEEE 50th Photovoltaics Specialists Conference (PVSC)*, 2023.

[296] Joel Jean, Patrick R Brown, Robert L Jaffe, Tonio Buonassisi, and Vladimir Bulović. Pathways for solar photovoltaics. *Energy & Environmental Science*, 8(4):1200–1219, 2015.

[297] Russell K Jones, James H Ermer, Christopher M Fetzer, and Richard R King. Evolution of multijunction solar cell technology for concentrating photovoltaics. *Japanese Journal of Applied Physics*, 51(10S), 2012.

[298] J E Parrott. The limiting efficiency of an edge-illuminated multigap solar cell. *Journal of Physics D: Applied Physics*, 12(3):441, mar 1979.

[299] A De Vos. Detailed balance limit of the efficiency of tandem solar cells. *Journal of Physics D: Applied Physics*, 13(5):839, may 1980.

[300] C. H. Henry. Limiting efficiencies of ideal single and multiple energy gap terrestrial solar cells. *Journal of Applied Physics*, 51(8):4494–4500, 07 2008.

[301] Antonio Martí and Gerardo L. Araújo. Limiting efficiencies for photovoltaic energy conversion in multigap systems. *Solar Energy Materials and Solar Cells*, 43(2):203–222, 1996.

[302] Andrew S. Brown and Martin A. Green. Limiting efficiency for current-constrained two-terminal tandem cell stacks. *Progress in Photovoltaics: Research and Applications*, 10(5):299–307, 2002.

[303] M Meusel, C Baur, W Guter, M Hermle, F Dimroth, AW Bett, T Bergunde, R Dietrich, R Kern, W Köstler, et al. Development status of european multi-junction space solar cells with high radiation hardness. *Proc. 20th EPSEC*, 2005.

[304] Ryan M. France, John F. Geisz, Tao Song, Waldo Olavarria, Michelle Young, Alan Kibbler, and Myles A. Steiner. Triple-junction solar cells with 39.5% terrestrial and 34.2% space efficiency enabled by thick quantum well superlattices. *Joule*, 6(5):1121–1135, 2022.

[305] Céline Michel, Jérôme Loicq, Tanguy Thibert, and Serge Habraken. Optical study of diffraction grating/fresnel lens combinations applied to a spectral-splitting solar concentrator for space applications. *Appl. Opt.*, 54(22):6666–6673, Aug 2015.

[306] Sunita Darbe and Harry Atwater. Resonant dielectric high-contrast gratings as spectrum splitting optical elements for ultrahigh efficiency (>50%) photovoltaics. In *2015 IEEE 42nd Photovoltaic Specialist Conference (PVSC)*, pages 1–4, 2015.

[307] Carissa N. Eisler, Cristofer A. Flowers, Emily C. Warmann, John V. Lloyd, Pilar Espinet-Gonzalez, Sunita Darbe, Michelle S. Dee, Matthew D. Escarra, Emily D. Kosten, Weijun Zhou, and Harry A. Atwater. The polyhedral specular reflector: A spectrum-splitting multijunction design to achieve ultrahigh (>50%) solar module efficiencies. *IEEE Journal of Photovoltaics*, 9(1):174–182, 2019.

[308] Duanhui Li, Tian Gu, Jurgen Michel, and Juejun Hu. Micro-prism spectrum splitting optics for lateral-arrayed multi junction micro cpv. In *2019 IEEE 46th Photovoltaic Specialists Conference (PVSC)*, pages 2524–2527, 2019.

[309] Xiaoting Wang, Nick Waite, Paola Murcia, Keith Emery, Myles Steiner, Fouad Kiamilev, Keith Goossen, Christiana Honsberg,

and Allen Barnett. Lateral spectrum splitting concentrator photovoltaics: direct measurement of component and submodule efficiency. *Progress in Photovoltaics: Research and Applications*, 20(2):149–165, 2012.

[310] Martin A. Green, Mark J. Keevers, Ian Thomas, John B. Lasich, Keith Emery, and Richard R. King. 40% efficient sunlight to electricity conversion. *Progress in Photovoltaics: Research and Applications*, 23(6):685–691, 2015.

[311] A. Scuto, R. Corso, M. Leonardi, R.G. Milazzo, S. M. S. Privitera, C. Colletti, M. Foti, F. Bizzarri, C. Gerardi, and S.A. Lombardo. Outdoor performance of gaas/bifacial si heterojunction four-terminal system using optical spectrum splitting. *Solar Energy*, 241:483–491, 2022.

[312] Yuechen Wu and Raymond K. Kostuk. Two-junction holographic spectrum-splitting microconcentrating photovoltaic system. *Journal of Photonics for Energy*, 7(1):017001, 2017.

[313] Shelby D. Vorndran, Benjamin Chrysler, Brian Wheelwright, Roger Angel, Zachary Holman, and Raymond Kostuk. Off-axis holographic lens spectrum-splitting photovoltaic system for direct and diffuse solar energy conversion. *Appl. Opt.*, 55(27):7522–7529, Sep 2016.

[314] Ian Marius Peters, Carlos David Rodríguez Gallegos, Larry Lüer, Jens A. Hauch, and Christoph J. Brabec. Practical limits of multijunction solar cells. *Progress in Photovoltaics: Research and Applications*, n/a(n/a).

[315] Ugur Ortabasi, Allan Lewandowski, Robert McConnell, Daniel J Aiken, Paul L Sharps, and Bertrand G Bovard. Dish/photovoltaic cavity converter (pvcc) system for ultimate solar-to-electricty conversion efficiency-general concept and first performance predictions. In *Conference Record of the Twenty-Ninth IEEE Photovoltaic Specialists Conference, 2002.*, pages 1616–1620. IEEE, 2002.

[316] Bernhard Mitchell, Gerhard Peharz, Gerald Siefer, Marius Peters, Tobias Gandy, Jan Christoph Goldschmidt, Jan Benick, Stefan W. Glunz, Andreas W. Bett, and Frank Dimroth. Four-junction spectral beam-splitting photovoltaic receiver with high optical efficiency. *Progress in Photovoltaics: Research and Applications*, 19(1):61–72, 2011.

[317] Sarah E Sofia, Hao Wang, Annalisa Bruno, Jose Luis Cruz-Campa, Tonio Buonassisi, and Ian Marius Peters. Roadmap for cost-effective, commercially-viable perovskite silicon tandems for the current and future pv market. *Sustainable Energy & Fuels*, 4(2):852–862, 2020.

[318] Joseph Burdick and Troy Glatfelter. Spectral response and i–v measurements of tandem amorphous-silicon alloy solar cells. *Solar Cells*, 18(3):301–314, 1986.

[319] Moritz H. Futscher and Bruno Ehrler. Efficiency limit of perovskite/si tandem solar cells. *ACS Energy Letters*, 1(4):863–868, 2016.

[320] Emily L. Warren, Michael G. Deceglie, Michael Rienäcker, Robby Peibst, Adele C. Tamboli, and Paul Stradins. Maximizing tandem solar cell power extraction using a three-terminal design. *Sustainable Energy Fuels*, 2:1141–1147, 2018.

[321] T. Nagashima, K. Okumura, K. Murata, and Y. Kimura. Three-terminal tandem solar cells with a back-contact type bottom cell. In *Conference Record of the Twenty-Eighth IEEE Photovoltaic Specialists Conference - 2000 (Cat. No.00CH37036)*, pages 1193–1196, 2000.

[322] John Wauchope Matthews. *Epitaxial growth*. Academic P., 1975.

[323] U. Gösele and Q.-Y. Tong. Semiconductor wafer bonding. *Annual Review of Materials Science*, 28(1):215–241, 1998.

[324] Emily L. Warren, William E. McMahon, Michael Rienäcker, Kaitlyn T. VanSant, Riley C. Whitehead, Robby Peibst, and Adele C. Tamboli. A taxonomy for three-terminal tandem solar cells. *ACS Energy Letters*, 5(4):1233–1242, 2020.

[325] Manuel Schnabel, Michael Rienäcker, Emily L. Warren, John F. Geisz, Robby Peibst, Paul Stradins, and Adele C. Tamboli. Equivalent performance in three-terminal and four-terminal tandem solar cells. *IEEE Journal of Photovoltaics*, 8(6):1584–1589, 2018.

[326] Philipp Tockhorn, Philipp Wagner, Lukas Kegelmann, Johann-Christoph Stang, Mathias Mews, Steve Albrecht, and Lars Korte. Three-terminal perovskite/silicon tandem solar cells with top and interdigitated rear contacts. *ACS Applied Energy Materials*, 3(2):1381–1392, 2020.

[327] William E. McMahon, Henning Schulte-Huxel, Jeronimo Buencuerpo, John F. Geisz, Michelle S. Young, Talysa R. Klein, Adele C. Tamboli, and Emily L. Warren. Homogenous voltage-matched strings using three-terminal tandem solar cells: Fundamentals and end losses. *IEEE Journal of Photovoltaics*, 11(4):1078–1086, 2021.

[328] ReRa Solutions. Rera solutions gaas solar cell.

[329] G. Condorelli, P. Rotoli, A. Canino, A. Battaglia, W. Favre, A. S. Ozanne, A. Moustafa, A. Danel, D. Muñoz, P. J. Ribeyron, and C. Gerardi. Contamination control challenges on shj solar cell processing. In *2017 IEEE 44th Photovoltaic Specialist Conference (PVSC)*, pages 1747–1751, 2017.

[330] G. Condorelli, W. Favre, A. Battaglia, P. Rotoli, A. Canino, M. Sciuto, A. Ragonesi, A. Danel, D. Muñoz, C. Roux, J.-F. Lerat, F. Medlege, V. Barth, L. Sicot, P.-J. Ribeyron, and C. Gerardi. High efficiency hetero-junction: From pilot line to industrial production. In *2018 IEEE 7th World Conference on Photovoltaic Energy Conversion (WCPEC) (A Joint Conference of 45th IEEE PVSC, 28th PVSEC & 34th EU PVSEC)*, pages 1970–1973, 2018.

[331] Massimo Izzi, Mario Tucci, Paola Delli Veneri, Sandra Scalari, Daniele Proietti, Claudio Colletti, Marco Balucani, and Luca Serenelli. Ampere: An european project aimed to decrease the levelized cost of energy with innovative heterojunction bifacial module solution ready for the market. In *2018 IEEE 7th World Conference on*

Photovoltaic Energy Conversion (WCPEC) (A Joint Conference of 45th IEEE PVSC, 28th PVSEC & 34th EU PVSEC), pages 569–572, 2018.

[332] Rubén Pérez and Peter Gumbsch. Directional anisotropy in the cleavage fracture of silicon. *Phys. Rev. Lett.*, 84:5347–5350, Jun 2000.

[333] A. Scuto, R. Corso, M. Leonardi, R.G. Milazzo, S.M.S. Privitera, C. Colletti, M. Foti, F. Bizzarri, C. Gerardi, and S. Lombardo. Data on the design optimization, indoor characterization and outdoor testing of gaas/bifacial si heterojunction four-terminal photovoltaic systems. *Data in Brief*, 45:108609, 2022.

[334] Thorlabs Inc. Thorlabs dichroic mirror.

[335] Roberto Corso, Fabio Matera, Andrea Scuto, and Salvatore A. Lombardo. Outdoor characterization of a bifacial four-terminal gaas/si minimodule under different albedo conditions. In *2023 IEEE 50th Photovoltaics Specialists Conference (PVSC)*, 2023.

[336] Corsin Battaglia, Silvia Martín de Nicolás, Stefaan De Wolf, Xingtian Yin, Maxwell Zheng, Christophe Ballif, and Ali Javey. Silicon heterojunction solar cell with passivated hole selective moox contact. *Applied Physics Letters*, 104(11):113902, 03 2014.

[337] Corsin Battaglia, Xingtian Yin, Maxwell Zheng, Ian D. Sharp, Teresa Chen, Stephen McDonnell, Angelica Azcatl, Carlo Carraro, Biwu Ma, Roya Maboudian, Robert. M. Wallace, and Ali Javey. Hole selective moox contact for silicon solar cells. *Nano Letters*, 14(2):967–971, 2014.

[338] T.T. Werner, Gavin M. Mudd, and Simon M. Jowitt. The world's by-product and critical metal resources part iii: A global assessment of indium. *Ore Geology Reviews*, 86:939–956, 2017.

[339] Erkan Aydin, Michele De Bastiani, Xinbo Yang, Muhammad Sajjad, Faisal Aljamaan, Yury Smirnov, Mohamed Nejib Hedhili, Wenzhu Liu, Thomas G. Allen, Lujia Xu, Emmanuel Van Kerschaver, Monica Morales-Masis, Udo Schwingenschlögl, and Stefaan De Wolf. Zr-doped indium oxide (izro) transparent electrodes

for perovskite-based tandem solar cells. *Advanced Functional Materials*, 29(25):1901741, 2019.

[340] Xiaohan Huang, Yurong Zhou, Wanwu Guo, Fengzhen Liu, Dongming Zhao, Rui Life, Haiwei Huang, Zhidan Hao, and Yuqin Zhou. Zr-doped indium oxide films for silicon heterojunction solar cells. *Solar Energy Materials and Solar Cells*, 260:112480, 2023.

[341] C. Manoharan, M. Jothibas, S. Johnson Jeyakumar, and S. Dhanapandian. Structural, optical and electrical properties of zr-doped in2o3 thin films. *Spectrochimica Acta Part A: Molecular and Biomolecular Spectroscopy*, 145:47–53, 2015.

[342] Susie Eustis and Mostafa A. El-Sayed. Why gold nanoparticles are more precious than pretty gold: noble metal surface plasmon resonance and its enhancement of the radiative and nonradiative properties of nanocrystals of different shapes. *Chemical Society reviews*, 35:209–217, 2006.

[343] F. Enrichi, A. Quandt, and G.C. Righini. Plasmonic enhanced solar cells: Summary of possible strategies and recent results. *Renewable and Sustainable Energy Reviews*, 82:2433–2439, 2018.

[344] Peisheng Liu, Hao Wang, Xiaoming Li, Muchen Rui, and Haibo Zeng. Localized surface plasmon resonance of cu nanoparticles by laser ablation in liquid media. *Rsc Advances*, 5(97):79738–79745, 2015.

Acknowledgements

I gratefully acknowledge my tutors, Dr. Salvatore Lombardo and Prof. Riccardo Reitano, for my professional and personal growth they have nurtured during these last three years, the impact of which cannot be understated. I would also like to thank my colleagues and friends from Consiglio Nazionale delle Ricerche, with whom I have shared many enjoyable and professionally exciting moments. I also acknowledge the contribution and kind helpfulness of the teaching staff of the University of Catania, namely the former coordinator of the PhD programme in Physiscs Prof. Sebastiano Albergo, the current coordinator Prof. Livio Lamia as well as the teachers of the courses I have taken for the PhD programme. Lastly, I want to thank the following research groups from for their collaborations in the field of new materials for silicon solar cells: Dr. Maria Miritello and Dr. Giorgia Franzò from CNR-IMM and UniCt PhD. student Salvatore La Manna for their work on sub-stoichiometric MoO_{3-x} (BEST4U project), Prof. Antonio Terrasi and PhD. students Andrea Lo Mastro and Fiorella Tringali from UniCt for their work on the IZrO anti-reflection coating (BEST4U project) and Prof. Stefano Boscarino and Prof. Francesco Ruffino from UniCt for their work on Cu-based plasmonic nanoparticles (BEST4U and SAMOTHRACE projects).